

Design, Modeling and Simulation of a Miniaturized Gas Sensor

Nicoleta Sandu Chivu

A Thesis

In the Department

of

Electrical and Computer Engineering

Presented in Partial Fulfillment of the Requirements

For the Degree of

Doctor of Philosophy (Electrical and Computer Engineering) at

Concordia University

Montreal, Quebec, Canada

September 2012

© Nicoleta Sandu Chivu, 2012

**CONCORDIA UNIVERSITY  
SCHOOL OF GRADUATE STUDIES**

This is to certify that the thesis prepared

By: Nicoleta Sandu Chivu

Entitled: Design, Modeling, and Simulation of a Miniaturized Gas Sensor

and submitted in partial fulfillment of the requirements for the degree of

DOCTOR OF PHILOSOPHY (Electrical & Computer Engineering)

complies with the regulations of the University and meets the accepted standards with respect to originality and quality.

Signed by the final examining committee:

<u>Dr. Gerard J. Gouw</u>	Chair
<u>Dr. Durgamadhab Misra</u>	External Examiner
<u>Dr. Javad Dargahi</u>	External to Program
<u>Dr. Leslie Landsberger</u>	Examiner
<u>Dr. Zahangir Kabir</u>	Examiner
<u>Dr. Mojtaba Kahrizi</u>	Thesis Supervisor

Approved by

Chair of Department or Graduate Program Director

Dean of Faculty

# ABSTRACT

## Design, Modeling and Simulation of a Miniaturized Gas Sensor

Nicoleta Sandu Chivu, Ph.D.

Concordia University, 2012

In this thesis we have designed, modeled and simulated a miniaturized gas ionization sensor (GIS). Gas ionization sensors work by detecting the ionization breakdown voltages,  $V_B$ , of the gases to be identified. Recently a GIS based on gold/silver nanowires was developed in Micro/Nano Devices Laboratories in ECE department at Concordia University that operates by field-ionizing unknown gases at exceptionally low voltages. The breakdown voltages of the gases are used to identify them and the resultant field-ion current-voltage ( $I-V$ ) characteristic is used to determine their pressures. Freestanding gold nanowires (AuNW), grown on one of the two parallel plates act as field-amplifiers to reduce the field ionization threshold voltages. The sensor was tested for several elemental gases like Ar, N<sub>2</sub> and He in pressure range of  $\sim 0.01 < P < 100$  Torr. Each gas demonstrated a distinctive  $I-V$  characteristic. Our simulations results were in agreement with the experimental.

Although the developed device demonstrated several advantages compare to the sensors available in the market, in terms of low cost, low power and high sensitivity but the device never tested for selectivity and for more complex gases. In practical applications there is usually a soup of gases (like an odor) and identification of one or

few particular gases in the soup are the subjects of interest. As well, monitoring the greenhouse gases is very essential in many environments.

There are many parameters which control the function of the GIS device. These parameters include the type of nanowires, their aspect ratio, porosity, configuration of nanowires, gap between the two electrodes and between the electrodes and the tip of nanowires, the sharpness of the nanowires and materials used to fabricate the nanowires. Therefore, the prior knowledge about the design of the device with any specification and for any particular application and functionality is very essential. Experimentally if it is not impossible it would be very difficult to design and optimize the sensor for detection of various gases by trial and error. It will be very expensive and very large labor and time consuming.

In this thesis, we have modeled the GIS device and its function, due to the field ionization, based on “A Particle-In-Cell/Monte-Carlo-Collision (PIC/MCC)”. All parameters responsible to control the function of the device are included in the model. The modeled device was simulated using a software tool that we modified specifically to accommodate the structure and functions of the device. We have called the software tool XOOPIE-GIS which is a modified and new version of open-source software called XOOPIE. As the electric field between the two electrodes is responsible for the breakdown of the gases inside the GIS, the non-linear electric field induced around nanowires is studied analytically and simulated using COMSOL, a multiphysics simulation tool. The results were then integrated in the XOOPIE-GIS codes.

The device was designed considering various nanowires like silver, gold, and ZnO. The simulations were done for some simple gases like Ar, N<sub>2</sub>, and Ne. The results

of simulations were verified with experimental results performed in the laboratories of Micro/Nano Device in ECE department at Concordia University prior to this work. We also modified the simulation tool for monitoring greenhouse gases like SF<sub>6</sub>, CF<sub>4</sub>, CO, and CO<sub>2</sub>. Further we tried to identify specific gases in an environment contains mixture of gases like N<sub>2</sub>O<sub>2</sub>CO<sub>2</sub>, ArNe, N<sub>2</sub>O<sub>2</sub>, and ArHe. We have found out that in these cases gases with highest concentration always dominate and influence the breakdown of the mixed gases. As a result, the application of this device will be very limited in these cases. We have suggested some modifications to the device structure to make it more suitable for identifying gases in a soup of gases.

## ACKNOWLEDGMENTS

First at all, I would like to express my sincere gratitude to my supervisor Dr. Mojtaba Kahrizi for his helps and supports. Without his advices, guidance and patience this thesis wouldn't reach its present form.

I also truly appreciate the members of my supervisory and examining committees for their advices and constructive comments which made a great improvement to this work.

I would like to convey my heartfelt thanks to Concordia University for offering me an environment to study and concentrate on my thesis. I give my sincere thanks to all my colleagues in particular I express my appreciation to Dr. Ramin Banan Sadeghian for his helpful advices at the early stage of this program.

Last but not least I am very grateful to my parents, Eugenia and Traian, who always believed in me and encouraged me to work hard to continue pursuing my studies, to my husband, Laurentiu, and to my son, Nicolas, who gave me all their supports and love.

This thesis is a dedication to all the people above. Without them I wouldn't be stand up today to pursue my dream.

# Table of Contents

List of Figures .....	x
List of Tables .....	xvi
List of Acronyms .....	xiii
List of Symbols .....	xix
<b>CHAPTER 1            INTRODUCTION.....</b>	<b>1</b>
1.1 OVERVIEW OF GAS SENSORS .....	2
<i>1.1.1 Chemical type gas sensors</i> .....	3
<i>1.1.2 Physical type gas sensors – Gas Ionization Sensors</i> .....	6
<i>1.1.3 GIS structure based on Metallic NW</i> .....	9
1.2 PROBLEM STATEMENT .....	11
1.3 METHODOLOGY .....	12
1.4 BASIC ASSUMPTION .....	14
1.5 CONTRIBUTION OF THE THESIS .....	14
1.6 ORGANIZATION OF THE THESIS .....	16
<b>CHAPTER 2            THEORETICAL BACKGROUND.....</b>	<b>18</b>
2.1 ELECTRICAL PHENOMENA IN GASES .....	18
<i>2.1.1 Ionization and Breakdown of Gases</i> .....	18
<i>2.1.2 Principles of Ionizations</i> .....	19
<i>2.1.3 Discharge of Gases</i> .....	20
<i>2.1.4 Paschen’s Law</i> .....	23
2.2 FIELD IONIZATION.....	24
<b>CHAPTER 3        ELECTROSTATIC FIELD INSIDE A GIS .....</b>	<b>26</b>

3.1 FIELD ENHANCEMENT AT THE TIP OF THE NANOWIRES .....	26
3.2 THE LOCAL ELECTRIC FIELD IN THE MODELED DEVICE .....	34
3.3 THE TOTAL ELECTRIC FIELD IN THE MODELED DEVICE .....	39
3.4 SCREENING EFFECT .....	40
<b>CHAPTER 4 SIMULATIONS OF THE MODELED ELECTRIC FIELD GENERATED AROUND NANOWIRES.....</b>	<b>42</b>
4.1 ELECTROSTATIC FIELD INSIDE THE GIS .....	43
4.1.1 <i>The Shape Effect of Nanowires tips</i> .....	45
4.1.2 <i>The Effect of Whiskers on the Electric Field Enhancement</i> .....	50
4.1.3 <i>The Effect of the Nanowires Separation on Electric Field Distribution</i> .....	53
4.1.4 <i>The Aspect Ratio <math>\beta</math> (the Length to Radius Ratio of the NW)</i> .....	56
4.1.5 <i>The Effect of the Distance between Plates</i> .....	61
4.1.6 <i>Electric Field Study for Non Parallel Plates</i> .....	63
4.2 CONCLUSIONS .....	67
<b>CHAPTER 5 SIMULATIONS OF THE MODELED GIS DEVICE.....</b>	<b>70</b>
5.1 MONTE CARLO COLLISIONS .....	71
5.1.1 <i>Steps in MCC Mechanism Applied to Model the Gas Discharge Inside of the GIS Device..</i>	73
5.1.2 <i>The Breakdown of the Device</i> .....	80
5.2 XOOPIC MONTE CARLO COLLISIONS PACKAGE .....	82
5.3 ELECTRON COLLISION CROSS SECTIONS .....	89
5.4 APPLYING CROSS SECTIONS IN XOOPIC-GIS .....	91
5.5 XOOPIC-GIS INPUT FILE .....	92
5.6 THE FLOW CHART OF THE XOOPIC-GIS .....	94
5.7 XOOPIC-GIS PARAMETERS OPTIMIZATION. ....	96
5.8 CONCLUSIONS .....	100
<b>CHAPTER 6 XOOPIC-GIS SIMULATION RESULTS.....</b>	<b>101</b>

6.1 GENERAL DESCRIPTION OF GAS IONIZATION IN GIS .....	102
6.2 VERIFICATION OF THE SIMULATION RESULTS .....	107
6.3 EFFECTS OF VARIOUS PARAMETERS ON AUNW-GIS .....	110
6.3.1 <i>Effect of Series Resistance on VB</i> .....	111
6.3.2 <i>Effect of Aspect Ratio on VB</i> .....	113
6.3.3 <i>Effect of the Chamber Width on VB</i> .....	114
6.3.4 <i>Effect of the Gap Distance on VB</i> .....	115
6.3.5 <i>Effect of Various Nanowires on VB</i> .....	115
6.4 DETECTION OF BREAKDOWN VOLTAGES FOR SIMPLE GASES .....	117
6.5 DETECTION OF BREAKDOWN VOLTAGES FOR GREENHOUSE GASES .....	118
6.6 DETECTION OF BREAKDOWN VOLTAGES FOR MIXED GASES .....	122
6.7 CONCLUSIONS .....	126
<b>CHAPTER 7 CONCLUSIONS, CONTRIBUTION AND FUTURE WORK.....</b>	<b>128</b>
7.1 SUMMARY OF THE PROJECT .....	128
7.2 CONTRIBUTIONS.....	129
7.3 FUTURE WORK .....	131
<b>BIBLIOGRAPHY.....</b>	<b>133</b>

## List of Figures

- FIGURE 1.1 SENSITIVITY OF THE P<sup>TH</sup> FILM AFTER EXPOSURE TO 300 PPM CONCENTRATION OF ODOR GASES AT THE THREE OPERATING TEMPERATURES [1].
- FIGURE 1.2 ELECTRICAL RESISTANCE VARIATIONS OF SAMPLE UPON INJECTION OF NH<sub>3</sub> GAS [7].
- FIGURE 1.3 THE SCHEMATIC DIAGRAM OF THE GAS IONIZATION SENSOR BASED ON CNTS FILM REPORTED BY JIARUI HUANG ET AL [22].
- FIGURE 1.4 THE NANOWIRE SENSOR DEVICE WITH A ZNO NANOWIRE FILM AS THE ANODE AND A CU PLATE AS THE CATHODE [23].
- FIGURE 1.5 CURRENT–VOLTAGE CURVES FOR HE, NO<sub>2</sub>, CO, H<sub>2</sub>, AIR AND O<sub>2</sub>, SHOWING DISTINCT BREAKDOWN VOLTAGES [23].
- FIGURE 1.6 SCHEMATIC ILLUSTRATIONS OF THE GIS WITH THE NANOWIRES GROWN ON ONE OF THE ELECTRODES [25].
- FIGURE 1.7 SIMULATIONS TOOLS USED TO MODEL AND OPTIMIZE THE GIS – XOOPICTOOL USED TO STUDY THE BREAKDOWN VOLTAGE V<sub>B</sub>; COMSOL TOOL USED TO STUDY THE ELECTRIC FIELD SURROUNDING THE NANOWIRES.
- FIGURE 2.1 I-V GASEOUS DISCHARGES CHARACTERISTIC IN UNIFORM FIELDS, UP TO THE BREAKDOWN POINT V<sub>B</sub>. (A) OHMIC REGION, (B) TRANSITION TO SATURATION, (C) SATURATION, (D) PRE-BREAKDOWN TOWNSEND DISCHARGE [35].
- FIGURE 2.2 VARIATION OF THE VOLTAGE WITH RESPECT TO Pd (PASCHEN'S CURVES) [35].
- FIGURE 2.3 [39] POTENTIAL ENERGY DIAGRAM FOR A 1S ELECTRON OF A HYDROGEN ATOM IN A FIELD OF 2V/Å, AT A DISTANCE OF 5.5Å FROM A TUNGSTEN SURFACE. EF IS THE FERMI LEVEL; UI, IONIZATION POTENTIAL, PM, ATOM POTENTIAL; PW, SUPERPOSITION OF APPLIED AND PSEUDO IMAGE POTENTIAL; XC, CRITICAL DISTANCE. DASHED LINES SHOW THE POTENTIAL IN THE ABSENCE OF AN EXTERNAL FIELD.
- FIGURE 2.4 FIELD IONIZATION OF HYDROGEN ATOMS IN A TWO PARALLEL PLATE GIS WITH NANOWIRES GROWN AT THE ANODE SIDE.

FIGURE 3.1 GEOMETRICAL MODEL FOR A FIELD- ENHANCING HEMISPHERE-ON-A-POST (RT = NANOWIRE RADIUS; ELOC = LOCAL ELECTRIC FIELD AT THE TIP; L = NANOWIRE LENGTH, D = DISTANCE BETWEEN THE TWO PARALLEL PLATES; V = APPLIED VOLTAGE BETWEEN THE TWO PARALLEL PLATES)

FIGURE 3.2 VARIATION OF THE EMPIRICAL PARAMETER C VERSUS X, USED INTO THE FITTING FORMULA OF THE COMPUTED VALUES OF THE ENHANCEMENT FACTOR B.

FIGURE 3.3 THEORETICAL WORKS ON SCREENING EFFECT VERSUS DISTANCE BETWEEN NANOWIRES (SL IS AN INTEGER NUMBER OF THE NANOWIRE LENGTH).

FIGURE 3.4 COMSOL SIMULATIONS ON SCREENING EFFECT VERSUS DISTANCE BETWEEN NANOWIRES (SL IS AN INTEGER NUMBER OF THE NANOWIRE LENGTH).

FIGURE 3.5 THEORETICAL WORKS ON SCREENING EFFECT VERSUS DISTANCE BETWEEN NANOWIRES FOR DIFFERENT B FACTOR– MATLAB SIMULATION

FIGURE 3.6 CONFIGURATION OF THE NEEDLE-TO-PLANE ELECTRODE SYSTEM WHERE “ $\xi$ ” IS THE DISTANCE FROM THE NEEDLE TIP, “A” IS THE DISTANCE BETWEEN NEEDLE AND PLANE ELECTRODES AND “R” THE RADIUS OF THE NEEDLE TIP [50].

FIGURE 3.7 THE TOTAL ELECTRIC FIELD CALCULATED IN Z-Y PLANE IN A NEEDLE TO PLAN ELECTRODE SYSTEM; NANOWIRE LENGTH  $L=25\mu\text{M}$ , TIP RADIUS  $R = 0.5\mu\text{M}$  AND GAP DISTANCE  $D=100\mu\text{M}$ .

FIGURE 3.8 THE TOTAL ELECTRIC FIELD CALCULATED IN Z-Y PLANE, FOR A GIS SYSTEM WITH A SINGLE NANOWIRE OF TIP RADIUS  $R = 0.5\mu\text{M}$ .

FIGURE 3.9 THE TOTAL ELECTRIC FIELD CALCULATED IN Z-Y PLANE, FOR A GIS SYSTEM WITH A SINGLE NANOWIRE OF TIP RADIUS  $R = 1\mu\text{M}$ .

FIGURE 3.10 ELECTRIC FIELD INTENSITY VERSUS DISTANCE FROM THE NANOWIRES TIP CALCULATED IN Z-Y PLANE, TIP RADIUS  $R = 1\mu\text{M}$ .

FIGURE 4.1 THE ELECTRIC FIELD LINE INTENSITY INDUCED AROUND A NANOWIRE GROWN BETWEEN TWO PARALLEL PLATES GIS SYSTEM; BACKGROUND GAS AR, APPLIED VOLTAGE  $V=-150\text{V}$ ; WORKING TEMPERATURE  $T=300\text{K}$ .

FIGURE 4.2 ELECTRIC FIELD INTENSITY FOR ONE NANOWIRE GROWN BETWEEN TWO PARALLEL PLATES GIS SYSTEM; ; BACKGROUND GAS AR, APPLIED VOLTAGE  $V=-150\text{V}$ ; WORKING TEMPERATURE

T=300K. A) CONVEX CIRCLE SHAPE TIP; RADIUS  $R = 0.01\mu\text{M}$ ; B) CONCAVE ELLIPSOID SHAPE TIP; SEMI AXES  $A = 0.01\mu\text{M}$ ,  $B = 0.03\mu\text{M}$ ; C) CONVEX ELLIPSOID SHAPE TIP; SEMI AXES  $A = 0.01\mu\text{M}$ ,  $B = 0.03\mu\text{M}$ ; D) CONCAVE ELLIPSOID SHAPE TIP; SEMI AXES  $A = 0.01\mu\text{M}$ ,  $B = 0.02\mu\text{M}$ ; E) CONVEX ELLIPSOID SHAPE TIP; SEMI AXES  $A = 0.01\mu\text{M}$ ,  $B = 0.02\mu\text{M}$ ; F) TRIANGLE SHAPE TIP,  $H = 0.1\mu\text{M}$ ; G) TRIANGLE SHAPE TIP,  $H = 0.02\mu\text{M}$ ;

FIGURE 4.3 ELECTRIC FIELD CONTOUR FOR DIFFERENT SHAPE OF NANOWIRES TIPS INSIDE A TWO PARALLEL PLATES GIS SYSTEM; BACKGROUND GAS AR, APPLIED VOLTAGE  $V=-150\text{V}$ ; WORKING TEMPERATURE  $T=300\text{K}$ . A) CONVEX CIRCLE SHAPE TIP; RADIUS  $R = 0.01\mu\text{M}$ ; B) CONCAVE ELLIPSOID SHAPE TIP; SEMI AXES  $A = 0.01\mu\text{M}$ ,  $B = 0.03\mu\text{M}$ ; C) CONVEX ELLIPSOID SHAPE TIP; SEMI AXES  $A = 0.01\mu\text{M}$ ,  $B = 0.03\mu\text{M}$ ; D) CONCAVE ELLIPSOID SHAPE TIP; SEMI AXES  $A = 0.01\mu\text{M}$ ,  $B = 0.02\mu\text{M}$ ; E) CONVEX ELLIPSOID SHAPE TIP; SEMI AXES  $A = 0.01\mu\text{M}$ ,  $B = 0.02\mu\text{M}$ ; F) TRIANGLE SHAPE TIP,  $H = 0.1\mu\text{M}$ ;

FIGURE 4.4 ELECTRIC FIELD INTENSITY FOR CIRCULAR NANOWIRES WITH GROWN WHISKERS ON THEIR TIPS GROWN BETWEEN TWO PARALLEL PLATES GIS SYSTEM; ; BACKGROUND GAS AR, APPLIED VOLTAGE  $V=-150\text{V}$ ; WORKING TEMPERATURE  $T=300\text{K}$ ; A) ONE SINGLE WHISKER; B) MULTIPLE WHISKERS.

FIGURE 4.5 ELECTRIC FIELD CONTOURS FOR CIRCULAR NANOWIRES WITH GROWN WHISKERS ON THEIR TIPS FOR A TWO PARALLEL PLATES GIS SYSTEM; BACKGROUND GAS AR, APPLIED VOLTAGE  $V=-150\text{V}$ ; WORKING TEMPERATURE  $T=300\text{K}$ ; A) ONE SINGLE WHISKER; B) MULTIPLE WHISKERS.

FIGURE 4.6 ELECTRIC FIELD INTENSITY VARIATION VERSUS DISTANCES BETWEEN THE NANOWIRES GROWN BETWEEN TWO PARALLEL PLATES GIS SYSTEM; BACKGROUND GAS AR, APPLIED VOLTAGE  $V=-150\text{V}$ ; WORKING TEMPERATURE  $T=300\text{K}$ ; ( $L = 5\mu\text{M}$ ,  $R = 0.01\mu\text{M}$ ,  $V = -150\text{V}$ ); A)  $S = 0.01\mu\text{M}$ ; B)  $S = 0.0125\mu\text{M}$ ; C)  $S = 0.0166\mu\text{M}$ ; D)  $S = 0.025\mu\text{M}$ ; E)  $S = 0.05\mu\text{M}$ ;

FIGURE 4.7 ELECTRIC FIELD CONTOUR EVOLUTION UPON NANOWIRES DISTANCE ( $L = 5\mu\text{M}$ ,  $R = 0.01\mu\text{M}$ ,  $V = -150\text{V}$ ); A)  $S = 0.01\mu\text{M}$ ; B)  $S = 0.0166\mu\text{M}$ ; C)  $S = 0.5\mu\text{M}$ ; D)  $S = 2.5\mu\text{M}$ ; E)  $S = 15\mu\text{M}$ ;

FIGURE 4.8 ELECTRIC FIELD LINES EVOLUTION UPON NANOWIRES DISTANCE ( $L = 5\mu\text{M}$ ,  $R = 0.01\mu\text{M}$ ,  $V = -150\text{V}$ ); A)  $S = 0.01\mu\text{M}$ ; B)  $S = 0.05\mu\text{M}$ ; C)  $S = 0.5\mu\text{M}$ ; D)  $S = 15\mu\text{M}$ ;

FIGURE 4.9 ELECTRIC FIELD INTENSITY EVOLUTION UPON NANOWIRES LENGTH IN A TWO PARALLEL PLATES GIS SYSTEM; BACKGROUND GAS AR, APPLIED VOLTAGE  $V=-150V$ ; WORKING TEMPERATURE  $T=300K$ ; ( $B = 500$ ;  $s = 0.025\mu m$ ,  $D = 100\mu m$ ,  $V = -150 V$ ); A)  $L = 5\mu m$ ; B)  $L = 15\mu m$ ; C)  $L = 10\mu m$ ; D)  $L = 25\mu m$ ;

FIGURE 4.10 ELECTRIC FIELD CONTOUR EVOLUTION UPON NANOWIRES LENGTH IN A TWO PARALLEL PLATES GIS SYSTEM ; BACKGROUND GAS AR, APPLIED VOLTAGE  $V=-150V$ ; WORKING TEMPERATURE  $T=300K$ ; ( $B = 500$ ;  $s = 0.025\mu m$ ,  $D = 100\mu m$ ,  $V = -150V$ ); A)  $L = 5\mu m$ ; B)  $L = 15\mu m$ ; C)  $L = 10\mu m$ ; D)  $L = 25\mu m$ ;

FIGURE 4.11 ELECTRIC FIELD LINES EVOLUTION UPON NANOWIRES LENGTH IN A TWO PARALLEL PLATES GIS SYSTEM ; BACKGROUND GAS AR, APPLIED VOLTAGE  $V=-150V$ ; WORKING TEMPERATURE  $T=300K$ ; ( $B = 500$ ;  $s = 0.025\mu m$ ,  $D = 100\mu m$ ,  $V = -150 V$ ); A)  $L = 5\mu m$ ; B)  $L = 10\mu m$ ; C)  $L = 15\mu m$ ; D)  $L = 20\mu m$ ; E)  $L = 25\mu m$ .

FIGURE 4.12 ELECTRIC FIELD VERSUS THE GAP BETWEEN THE NANOWIRES AND THE OPPOSITE ELECTRODE;

FIGURE 4.13 ELECTRIC FIELD INTENSITY EVOLUTION IN A TWO NON-PARALLEL GIS SYSTEM FIGURE 4.12 ELECTRIC FIELD INTENSITY EVOLUTION; A) ANODE IS PARALLEL WITH CATHODE; B) ANODE IS ROTATED WITH  $10^\circ$  WITH RESPECT TO THE CATHODE; C) ANODE IS ROTATED WITH  $40^\circ$  WITH RESPECT TO THE CATHODE; A) ANODE IS PARALLEL WITH CATHODE; B) ANODE IS ROTATED WITH  $10^\circ$  WITH RESPECT TO THE CATHODE; C) ANODE IS ROTATED WITH  $40^\circ$  WITH RESPECT TO THE CATHODE;

FIGURE 4.14 ELECTRIC FIELD CONTOUR IN A TWO NON-PARALLEL PLATES GIS SYSTEM FIGURE 4.12 ELECTRIC FIELD INTENSITY EVOLUTION; A) ANODE IS PARALLEL WITH CATHODE; B) ANODE IS ROTATED WITH  $10^\circ$  WITH RESPECT TO THE CATHODE; C) ANODE IS ROTATED WITH  $40^\circ$  WITH RESPECT TO THE CATHODE; A) ANODE IS PARALLEL WITH CATHODE; B) ANODE IS ROTATED WITH  $10^\circ$  WITH RESPECT TO THE CATHODE; C) ANODE IS ROTATED WITH  $20^\circ$  WITH RESPECT TO THE CATHODE; D) ANODE IS ROTATED WITH  $40^\circ$  WITH RESPECT TO THE CATHODE;

FIGURE 4.14 COMSOL SIMULATIONS FLOWCHART – STEPS TAKEN TO STUDY THE ELECTRIC FIELD INTENSITY INSIDE THE GIS CHAMBER.

FIGURE 5.1 THE MATHEMATICAL GRID SET INTO THE PLASMA REGION USED BY MONTE CARLO COLLISION TECHNIQUE.

FIGURE 5.2 GIS MODEL DEFINED AS TWO PARALLEL PLATE ELECTRODES WITH NANOWIRES GROWN AT THE CATHODE SIDE AND AN EXTERNAL CIRCUIT CONNECTED IN SERIES WITH THE DEVICE.

FIGURE 5.3 TWO DIMENSIONAL GRIDS USED TO WEIGHTING THE CHARGE DENSITY AT THE GRID POINTS [69].

FIGURE 5.4 PIC BILINEAR INTERPOLATION INTERPRETATION; AREAS ARE ASSIGNED TO GRID POINTS WITH THE PARTICLE CENTER LOCATED AT  $Q(X, Y)$ .

FIGURE 5.5 LOCATION OF THE  $E_j, k$  IN RELATION WITH  $\phi_j, k$  AT THE GRID POINTS OF THE MATHEMATICAL GRID USED IN MONTE CARLO COLLISION TECHNIQUE [69].

FIGURE 5.6 CLASSICAL PIC – MCC SCHEMES

FIGURE 5.7 FLOWCHART OF THE VOLTAGE COMPUTATION BETWEEN THE TWO ELECTRODES GIS AFFECTED BY THE POTENTIAL DROP ACROSS THE SERIES RESISTANCE  $R$ .

FIGURE 5.8 – PRINCIPLE OF ELECTRON-MOLECULE COLLISIONS INSIDE OF THE GIS CHAMBER REPRESENTED BY: IONIZATION CROSS SECTION, ELASTIC CROSS SECTION, ELECTRON ATTACHMENT CROSS SECTION AND EXCITATION CROSS SECTION.

FIGURE 5.9 –FLOW CHART OF THE ELECTRON-MOLECULE COLLISIONS INSIDE OF THE GAS DISCHARGE REPRESENTED BY THE ELASTIC AND INELASTIC ELECTRON COLLISION.

FIGURE 5.10 XOOPIE – MCC CLASS FLOWCHART OF THE IMPLEMENTED MCC TECHNIQUE INTO THE TWO PACKAGES OF XOOPIE SOFTWARE - ADVISOR AND PHYSICS.

FIGURE 5.11 XOOPIE-GIS INPUT FILE FLOWCHARTS – PHYSICS AND DEVICE STRUCTURE.

FIGURE 5.12 XOOPIE GIS FLOW CHART.

FIGURE 5.13 THE ELECTRIC FIELD INTENSITY - COMSOL SIMULATION FIGURE 5.11 XOOPIE-GIS; THE INSET SHOWS THE SAME ELECTRIC FIELD INTENSITY FROM XOOPIE-GIS SIMULATIONS.

FIGURE 5.14 XOOPIE SIMULATIONS FLOWCHART.

FIGURE 6.1 THE GIS SCHEMATIC DEVICE WITH SERIES RESISTANCE  $R$  SHOWING THE CHARGE ACCUMULATION AT THE ANODE.

FIGURE 6.2 THE 2 – D MODEL FOR THE DEVICE SHOWING THE RADIATION- GENERATED ELECTRONS (OR IONS) BEFORE A BIAS VOLTAGE WAS APPLIED.

FIGURE 6.3 THE ELECTRIC FIELD INTENSITY BETWEEN THE TWO ELECTRODES FOR THE EXTERNAL APPLIED FIELD OF  $V = -150V$ ; X AXES REPRESENTS THE CHAMBER DEVICE LENGTH, ON Y AXES IS REPRESENTED THE GAP DISTANCE BETWEEN THE TWO PLATES; A) 3D VIEW WITH ELECTRIC FIELD INTENSITY SHOWN ON Z AXES; B) 3-D VIEW WITH A SECTION CUT ALONG THE Z AXES.

FIGURE 6.4. PHASE SPACE PLOT OF ELECTRONS AND ARGON IONS WHEN THE CHARGE CONCENTRATION AT THE FIRST AVALANCHE BECOME MAXIMUM A) ELECTRONS AND B) IONS AT  $P = 1$  TORR,  $V = -155V$ , C) ELECTRONS AND D) IONS AT  $P = 0.05$ TORR,  $V = -180V$

FIGURE 6.5 THE EVOLUTION OF THE TOTAL NUMBER OF CARRIERS IN ARGON FOR  $P=1$  TORR. (BOTH AXES ARE LOGARITHMIC SCALED)

FIGURE 6.6 THE  $I-T$  CHARACTERISTICS SHOWING THE BREAKDOWN OF ARGON GAS AT PRESSURE  $P = 1$ TORR.

FIGURE 6.7 SIMULATED  $V-P$  CURVES FOR AuNWS GROWN AT CATHODE SIDE [25].

FIGURE 6.8 EXPERIMENTAL  $V-P$  CURVES FOR AuNWS GROWN AT CATHODE AND AT ANODE [25].

FIGURE 6.9 EXPERIMENTAL  $V-P$  CURVE FOR ARNWS GROWN AT CATHODE [26].

FIGURE 6.10 SIMULATED  $V-P$  CURVE FOR ARNWS GROWN AT CATHODE [26].

FIGURE 6.11 GENERATED CURRENT VERSUS TIME FOR AR AT  $P= 1$  TORR,  $BETA = 500$ ,  $Y = 100\mu M$ ,  $X = 1000\mu M$  AND A)  $R = 4$  OHM, B)  $R = 6$  OHM, C)  $R = 8$  OHM, D)  $R = 10$  OHM

FIGURE 6.12 SHOWS A TYPICAL SIMULATION RESULT OF GENERATED CURRENT VERSUS TIME BETWEEN THE TWO PARALLEL PLATES FOR THE DEVICE HAVING A) AR NWS; B) ZNO NWS.

FIGURE 6.13 SIMULATION RESULT OF GENERATED CATHODE CURRENT VERSUS TIME FOR THE DEVICE HAVING AS BACKGROUND GAS A) HE,  $V_B = -200V$  ; B) NE,  $V_B = -190$  V.

FIGURE 6.14 CF<sub>4</sub> PARTICLE CHARGE NUMBER EVOLUTION VERSUS TIME REPORTED BY N. CHIVU AND M. KAHRIZI [42].

FIGURE 6.15  $V_{APP} - T$  CURVES FOR A) SF<sub>6</sub> - GOLD; B) N<sub>2</sub> - GOLD; C) CO<sub>2</sub> - GOLD; D) CF<sub>4</sub> - GOLD.

FIGURE 6.16 PHASE SPACE PLOT OF AR (50%)NE(50%) FOR A) ARGON IONS; B) ELECTRONS; C) NEON IONS.

FIGURE 6.17 THE ELECTRIC FIELD INTENSITY ALONG Y AXIS (E<sub>Y</sub>) OF THE CELL FOR A) AR (80%) NE(20%); B) AR(50%)NE(50%).

FIGURE 6.18 THE GENERATED CURRENT VERSUS TIME FOR (A) AR (10%) NE (90%) (B) AR (20%) NE (80%) (C) AR (50%) NE(50%)

## List of Tables

TABLE 3.1 VALUES OF THE COMPUTED AND FITTED VALUES OF THE ENHANCEMENT FACTOR B OF EVENLY SPACED LINEAR ARRAYS FOR VARIOUS COMBINATIONS OF L/R, AND S/L [50].

TABLE 4.1 ELECTRIC FIELD INTENSITY FOR DIFFERENT SHAPE OF NANOWIRES TIPS.

TABLE 4.2 ELECTRIC FIELD INTENSITY FOR DIFFERENT NANOWIRES TIPS:

TABLE 4.3 ELECTRIC FIELD INTENSITY FOR DIFFERENT DISTANCES BETWEEN THE NANOWIRES:

TABLE 4.4 ELECTRIC FIELD INTENSITY FOR NANOWIRE WITH VARIOUS LENGTHS.

TABLE 4.5 ELECTRIC FIELD INTENSITY FOR DIFFERENT GAP DISTANCE.

TABLE 5.1 THE EFFECT OF THE NANOWIRE TIP SHAPE ON BREAKDOWN. ALL OTHER PARAMETERS WERE TAKEN THE SAME. THE MEASUREMENTS ARE DONE FOR AR GAS.

TABLE 5.2 THE TIME OF BREAKDOWN FOR DEVICES VERSUS THE DISTANCES BETWEEN NANOWIRES. ALL OTHER PARAMETERS WERE TAKEN THE SAME. THE MEASUREMENTS ARE DONE FOR AR GAS.

TABLE 6.1 THE EFFECT OF SERIES RESISTANCE ON  $V_B$

TABLE 6.2 THE EFFECT OF THE ENHANCEMENT FACTOR ON  $V_B$

TABLE 6.3 THE EFFECT OF THE CHAMBER WIDTHS ON  $V_B$

TABLE 6.4 THE EFFECT OF THE GAP DISTANCE ON  $V_B$

TABLE 6.5 THE EFFECT OF DIFFERENT NANOWIRES ON  $V_B$

TABLE 6.6 SIMULATION RESULTS OF BREAKDOWN VOLTAGES FOR SEVERAL GASES IN THE MODELED GIS DEVICE.

TABLE 6.7 SIMULATION RESULTS OF BREAKDOWN VOLTAGES FOR GREENHOUSE GASES IN THE MODELED GIS DEVICE.

TABLE 6.8 EXTRAPOLATED  $V_B$  VALUES AT THE SAMPLE TIME  $t = 1.2 \times 10^{-9}$  S, BASED ON SIMULATION RESULTS OF BREAKDOWN VOLTAGES FOR SEVERAL GREENHOUSE GASES IN THE MODELED GIS DEVICE.

TABLE 6.9 REPRESENTS THE PARAMETERS USED IN THE SIMULATIONS FOR AUNWS, FOR TWO DIFFERENT GAS MIXTURE, AT  $R = 10$  OHM, ( $BETA = 500$ ,  $X = 1000 \mu\text{M}$ ,  $Y = 100 \mu\text{M}$ ).

TABLE 6.10 SIMULATION RESULTS OF BREAKDOWN VOLTAGES FOR SEVERAL GAS MIXTURES IN THE  
MODELED GIS DEVICE.

## List of Acronyms

AuNW	Gold Nanowire
AgNW	Silver Nanowire
CMOS	Complementary Metal Oxide Semiconductor
CNTs	Carbon Nanotubes
COMSOL	Finite Element Method Analyzer Software Tool
FI	Field Ionization
FIM	Field Ion Microscope
FN	Fowler Nordheim
ITO	Indium tin oxide
GIS	Gas Ionization Sensors
MATLAB	Mathematical Software Tool
MCC	Monte Carlo Collisions
MFP	Mean Free Paths
NW-GIS	Nanowires Gas Ionization Sensor
MWNTs	Multiwall Carbon Nanotubes
PIC	Particle in Cell
XOOPIC	Object Oriented Particle in Cell Code
XOOPIC-GIS	Object Oriented Particle in Cell Code – Gas Ionization Sensor
ZnONW	Zinc Oxide Nanowire

## List of Symbols

P	Gas pressure	[torr]
G	Ion-electron generation rate	[cm <sup>-3</sup> s <sup>-1</sup> ]
R	Ion-electron recombination rate	[cm <sup>-3</sup> s <sup>-1</sup> ]
e	Charge per electron	1.602×10 <sup>-19</sup> [C]
n	Charged particle concentration	[cm <sup>-3</sup> ]
n <sub>e</sub> ,n <sub>i</sub>	Concentration of electrons and ions	[cm <sup>-3</sup> ]
μ <sub>e</sub> ,μ <sub>i</sub>	Electron and Ion mobility	[cm <sup>2</sup> V <sup>-1</sup> s <sup>-1</sup> ]
dn/dt	Rate of production of charged particles	[cm <sup>-3</sup> s <sup>-1</sup> ]
n <sub>+</sub>	Secondary electrons generated per second	[cm <sup>-3</sup> s <sup>-1</sup> ]
n <sub>0</sub>	Primary leaving the cathode per second	[cm <sup>-3</sup> s <sup>-1</sup> ]
n <sub>a</sub>	Total electrons arriving at the anode	[cm <sup>-3</sup> s <sup>-1</sup> ]
V <sub>B</sub>	Breakdown voltage	[V]
Φ	Work function	[eV]
d, d <sub>gap</sub>	Interelectrode distance	[cm]
E	Effective electric field	[Vcm <sup>-1</sup> ]
E <sub>app</sub>	Applied electric field	[Vcm <sup>-1</sup> ]
E <sub>loc</sub>	Local electric field	[Vcm <sup>-1</sup> ]
J	Current density	[Acm <sup>-2</sup> ]
α	Townsend's primary ionization coefficient	[cm <sup>-1</sup> ]
ω/α	Total secondary electron factor	–
γ	Secondary electron factor by ion bombardment	–
β	Electric field enhancement factor	–

$l$	Nanowire length	$[\mu\text{m}]$
$r_t$	Nanowire tip radius	$[\text{nm}]$
$\eta$	The ionization coefficient	–
$s$	Nanowire separation	$[\mu\text{m}]$

# Chapter 1

## Introduction

In recent years, concerns about protection of our ecosystem, safety and security of our societies has dramatically increased. Identification of toxic or bad-smelling gases, hazardous gases used for industrial processes, detection of air pollutants in environment, detection of the various volatile gases or smells generated from foods or food materials, hazardous gases generated by chemical, environmental, medical industries has become increasingly important. Many observable characteristics of drinking water like color, taste, smell, and odor are the signs that there may be a problem with the water. For the above reasons observable parameters in particular the odor could be due to the water contamination with some toxic chemicals, organic compounds and bacteria, at dangerous levels. In military and security industries, detecting poisonous and explosive gases is a daily challenging problem. Often the gaseous components are present at very low levels and mixed with several other disturbing gases, the detection is not easy. As a result, development of a sophisticated system to detect and control gases is felt more than ever. For this, development of gas sensors with high selectivity, sensitivity, reversibility and durability integrated with microelectronic circuitry, software tools, pattern recognition, and multi-sensing systems, all together into a device (an e-Nose) is highly desirable.

# 1.1 Overview of Gas Sensors

Gas sensors are devices that identify and/or measure the concentration of a particular gas, in a background atmosphere. The performance of a gas sensor is evaluated by suitable parameters such as:

1. Selectivity;
2. Sensitivity;
3. Stability;
4. Response time;
5. Recovery time;
6. Life cycle;
7. Working temperature.

In practice it is a difficult task to create an ideal gas sensor with all the above characteristics. On the other hand in many applications it is not required that the sensor have all the ideal parameters at once. The main requirements for a good performance of a sensor are stability, sensitivity, selectivity, reversibility, and low cost.

Based on the operation mechanism, the gas sensors can be classified into chemical type gas sensors operated by gas adsorption and physical type gas sensors operated by field ionization.

## 1.1.1 Chemical Type Gas Sensors

A chemical sensor is a device which transforms chemical information into an analytical signal. Usually gaseous species are adsorbed at the surface of materials. By monitoring the changes in materials parameters, the type and concentration of the gas can be detected. Materials such as carbon nanotubes (CNTs), polymer, porous silicon, and metaloxides were used as active layer in these types of sensors [1-9]. In most cases the gas molecules are absorbed by the active layer leading to a change in the electrical resistance of the sensor. Except a few type of polymer based sensors, this type of sensors works at high temperatures (300C – 500C). Another disadvantage of this type of sensors is that is difficult to make the distinction between different mixtures of gases with different concentration as the net change in the conductance can be equal to the one of a single pure gas.

Sakurai et al. [1] reported the detection of ammonia, methane, ethanol and chloroform gases using polythiophene (pTh) film and poly (3n dodecylthiophene) (pDITh) as sensitive layer, working at temperatures closer to room temperature.

The adsorption or desorption of those volatiles gases induces a measurable change in the resistance of the conductive polymer layer. The film exposure at the studied gases was done at room temperature and one atmosphere pressure with humidity of 65%. After 10 minutes exposure to the gas, the gas sensor was refreshed in the air for 20 minutes. For example, in the ammonia detection the resistance of the pTh layer increased fast under the gas exposure and then remained constant when ammonia was replaced by air. The sensitivity ( $S = (R_g - R_i) / R_i$ ) [1] where  $R_i$  is the initial resistance and  $R_g$  is the resistance

after exposure) of the sensor detecting several gases was reported under various operating temperatures (Figure 1.1) [1].

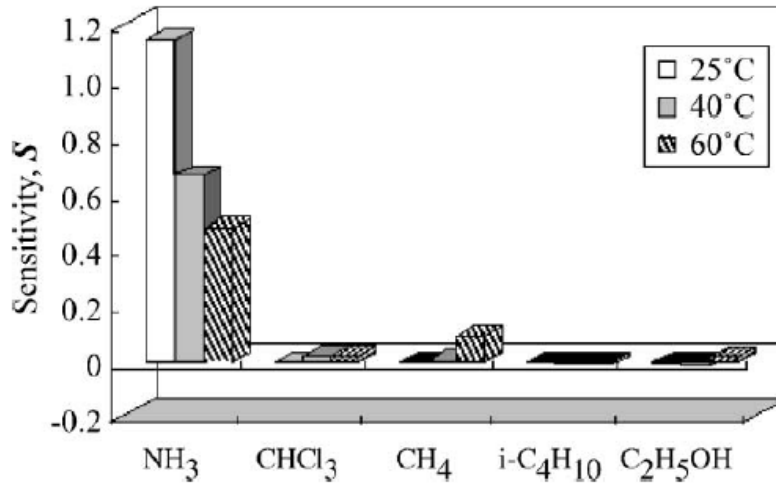


Figure 1.1 Sensitivity of the pTh film after exposure to 300 ppm concentration of odor gases at the three operating temperatures [1].

From Figure 1.1 it can be seen that for different gases at different temperatures, the polymer resistance changes considerably and the gases were successfully detected.

In his research, M. Y. Faizah [7] successfully reported the detection of carbon dioxide (CO<sub>2</sub>), acetylene (C<sub>2</sub>H<sub>2</sub>), ammonia (NH<sub>3</sub>), natural gas (95% methane, CH<sub>4</sub>) and hydrogen (H<sub>2</sub>) using the carbon nanotubes as the sensible layer (Figure 1.2). The electrical changes in the carbon nanotubes will detect the presence of different test gases.

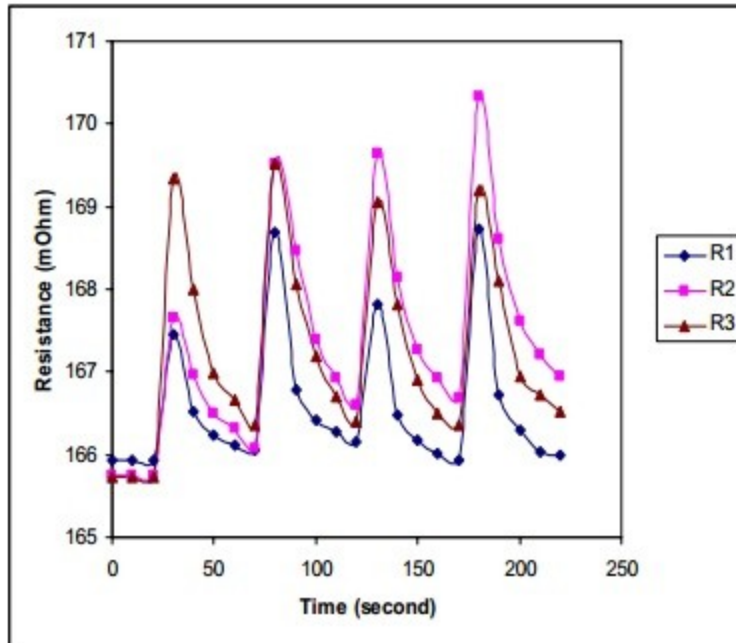


Figure 1.2 Electrical resistance variations of sample upon injection of  $\text{NH}_3$  gas [7].

Although the chemical type sensors may show good sensitivity with low cost and a simple working principle but these sensors don't have high accuracy in detection of the gases with low adsorption energy. Also, detection of any gas in mixed gases is a very difficult task, if ever possible. Another drawback for these types of sensors is that due to adsorption of gases, the nature sensing element of the sensors changes and in most cases is not reversible.

## 1.1.2 Physical Type Gas Sensors – Gas Ionization Sensors

In the physical sensors no chemical reactions take place and the analytical signal is the result of a physical process. Among all physical type of gas sensors available in the market or reported in literature gaseous breakdown ionization sensors [10-17] have several advantages in terms of miniaturization and selectivity. Also as there is no adsorption and desorption of the gases by the sensor elements, durability and response time have been improved. The ionization sensor is basically made of two parallel plates, anode and cathode. These devices work by fingerprinting the ionization *breakdown voltage* of the unknown gas, making them a more suitable technique to detect various gases particularly distinguishing gases in a complex environment. Such a technique is feasible and provides improved selectivity, because it is well-established that at constant temperature and pressure every gas has a unique breakdown electric field [18-23]. However, in uniform fields the voltages required to cause gaseous breakdown are in the order of several hundred to thousand volts [10] therefore, either difficult or hazardous to employ. The solution is to create a high electric field inside of the gas sensor with a lower applied voltage. There are several works done and reported in literature in this regard. Modi and co-workers [21] have reported the fabrication and testing of an ionization microsensor which detects various gases based on the electrical breakdown of gases. The gas sensor was basically a two electrodes system (anode and cathode) separated by the background gas and between the electrodes a controlled direct voltage was applied. The

anode side was in fact a multiwall carbon nanotubes (MWNTs) film. The applied voltage creates a very high nonlinear electric field at the nanotubes tips and promotes the creation of a “corona” leading to a powerful electron avalanche, lowering the breakdown voltages. The sensors are not affected anymore by the gas adsorption property and showed a good selectivity and sensitivity. The system was tested in the air with and without the carbon nanotubes at the anode side, proving that the breakdown voltage is lower (about 65%) when MWNTs were used.

With the MWNTs configuration at the anode side, the study was done to detect gases like ammonia, helium, argon, nitrogen, oxygen and air at room temperature and a chamber pressure of 760 Torr. The distance between the two electrodes was maintained at 150  $\mu\text{m}$ . The results show that each gas has a distinct breakdown pattern; the lowest value is reached by helium, at 164V and highest by ammonia (430V).

Jiarui Huang and co-workers [22] incorporated carbon nanotubes (CNTs) grown on silicon substrate into their gas ionization sensor. They have done their tests with the nanotubes structure at the anode side as well as at the cathode side to detect ammonia in the ambient air. In the configuration with the CNTs at the cathode, the secondary electron emission ejected from the sharp tips increases the ionization collisions and breakdown voltage is further lowered comparative to the anode side configuration.

The schematic of the gas sensor system of their research is shown in Figure 1.3, where one electrode is made of CNTs film and the other one is an indium tin oxide (ITO) glass plate, separated by a glass insulator.

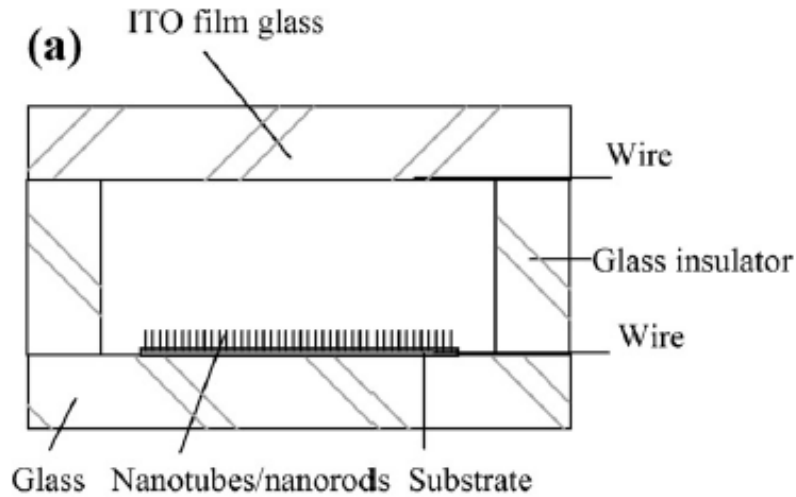


Figure 1.3 The schematic diagram of the gas ionization sensor based on CNTs film reported by Jiarui Huang et al [22].

However, in an atmosphere containing oxygen, the CNTs can easily degrade due to the oxidation process.

Liao, L. et al [23] used ZnO nanowires as the field ionization anode instead of CNTs proving a better stability and anti-oxidation behavior. Also the very sharp nanowires tip generates high nonlinear electric field at a low applied voltage between the two electrodes. The schematic of the gas ionization sensor device structure is shown in Figure 1.4.

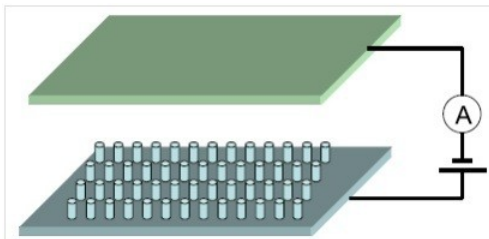


Figure 1.4 The nanowire sensor device with a ZnO nanowire film as the anode and a Cu plate as the cathode [23].

Figure 1.5 demonstrates the I-V characteristics of the sensor for various gases reported by reference [23].

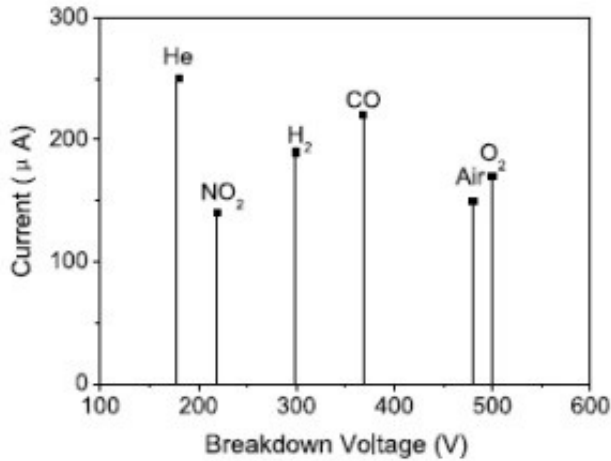


Figure 1.5 Current–Voltage curves for He, NO<sub>2</sub>, CO, H<sub>2</sub>, air and O<sub>2</sub>, showing distinct breakdown voltages [23].

Although the breakdown voltages for ZnO nanowires are higher than the CNT's breakdown voltages, the stability and anti-oxidation property of ZnO is much better.

### 1.1.3 GIS Structure Based on Metallic NWs

The design and fabrication of the device was made based on available technology and equipment in the laboratory. The GIS sensor with metallic nanowires is basically made of two parallel plates, anode and cathode, with vertically aligned nanowires grown on one electrode, as illustrated in Figure 1.6 [24]. The nanowires materials used in this work were either Ag, or Au. The two electrodes are separated by the background gas (Ar as an example).

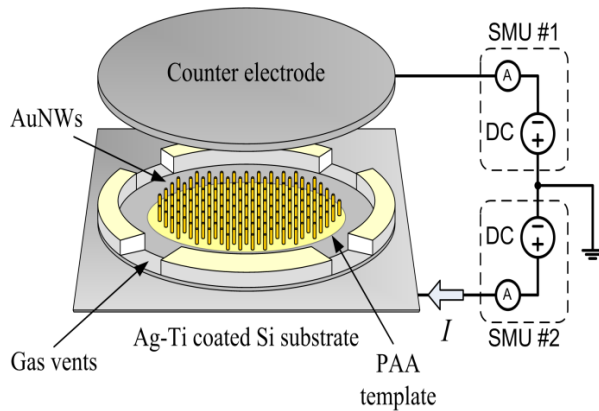


Figure 1.6 Schematic illustrations of the GIS with the nanowires grown on one of the electrodes [24].

The fabricated device is a part of an ongoing research in Micro/Nano Device Fabrication Laboratories in ECE department to develop an odor sensor (an eNose) for various applications including monitoring the quality of air, water, and so on. In this context, this miniaturized gas sensor based on metallic nanowires is designed and developed recently [24-34]. The miniaturized device is proven to be very sensitive, low cost and operates on very low voltages. The device is also compatible with standard CMOS technologies (it is fabricated on single crystal silicon wafers). So, it can be easily integrated with any microelectronic circuitry. There are many parameters, which control the functionality of the developed GIS device. These parameters include aspect ratio of nanowires, porosity, configuration of nanowires, gap between the two electrodes, gap between the electrodes and the tip of nanowires, the sharpness of the nanowires, the effects of nonlinearity of the electric field due to the aspect ratio of the nanowires, inter-wire distances and materials used to grow the nanowires. Considering all these parameters, the design of the device needs to be optimized to make suitable for various applications. The optimization of the device experimentally using fabrication-testing and using trial and error technique, will be very costly and time consuming.

## 1.2 Problem Statement

Most of the chemical gas sensors, beside the fact that they operate at high temperature, they have also potential difficulties to detect gases with low absorption energy and to distinguish between gases or gas mixtures. To overcome this inconvenience, a gas ionization sensor is developed. To design and adjust a GIS for a specific application is very time consuming, based on the fact that experiments should be repeated by trial and error. Therefore, modeling and simulations are required to adjust and optimize the sensor for any specific application, prior to fabrication of the device. The main task of this thesis is focused on the optimization of the design and parameters which control the functionality of the fabricated device. Parameters like the aspect ratio of nanowires, gap between the two electrodes, gap between the electrodes and the tip of nanowires, the sharpness of the nanowires, configuration of nanowires and materials used to fabricate the nanowires are of main interest in the fabrication and design of GIS.

Further, the breakdown behavior of the gases can be improved by achieving a high nonlinear electric field inside the gas chamber. In this regard, analytical studies on nonlinear electric field between the two electrodes are *necessary to be done*.

The second task of this thesis is focused on the gas detection from a mixture of gases and greenhouse gas detection.

## 1.3 Methodology

Any scientific research method involves a mutual interdependence between experimental work and theoretical work. By repeating the experiments, the data result is collected and then is fitted in patterns and analyzed by the theoretical approaches. An important bridge between the experimental work and theoretical studies of a specific research is the computer experiment or computer simulations. The basic idea in computer simulations is to design and simulate the actual physical system and to analyze the simulation results. The main advantage of the computer simulation is that complicated physical systems can be easily studied, helping us understand and predict the system. In order to model our GIS, several computer simulations are carried out to determine the best parameters and device configuration. The software tools used for simulations are XOOPIE-GIS and COMSOL as is shown in Figure 1.7.

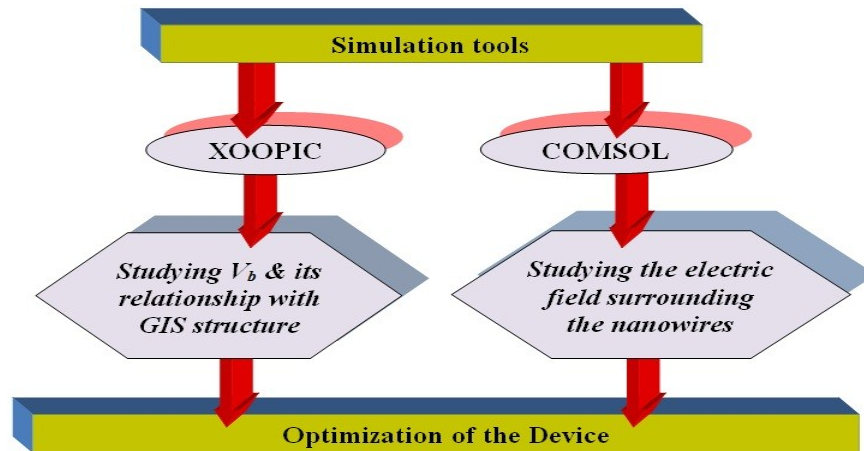


Figure 1.7 Simulation tools used to model and optimize the GIS – XOOPIE tool used to study the breakdown voltage  $V_B$ ; COMSOL tool used to study the electric field surrounding the nanowires.

Based on XOOPIIC, and an object oriented particle-in-cell (PIC) code, we have developed our XOOPIIC-GIS software tool to accommodate the design, structure and the function of our device.

We designed our GIS as a two parallel rectangular equipotential sheets, corresponding to the two electrodes of the sensor. The nanowires were designed to grow on one of the plates placed between the two electrodes. Gases to be identified fill up the space, gas chamber, between the two plates.

An external voltage was considered between the two electrodes generating an electric field inside the chamber. The discharge of gas molecules caused by the electric field, generated primary and secondary electrons, ions, and finally the breakdown of the gases, all were modeled in this work.

The electron cross sections are used inside of our XOOPIIC-GIS to model the particles collisions through Particle in Cell – Monte Carlo Collision (PIC-MCC) mechanism.

Analytical work is done to calculate the local and total electric field, responsible for the breakdown of the gases inside the modeled device.

Based on the analytical model, simulations were carried out using finite element method analyzer COMSOL to optimize the nanowires shape and their configurations.

The proposed model and the results of simulation of the GIS were verified by comparing them with the experimental results obtained in our laboratory. The XOOPIIC-GIS was further developed to accommodate greenhouse gases as well as detection of impurities in mixed gases.

## 1.4 Basic Assumptions

Several assumptions are done in our XOOPIE-GIS simulation. The geometry of the device in x-y coordinates is a rectangle having the horizontal length of 1 cm and the vertical length of 100 $\mu$ m. The nanowire length varies between 15 $\mu$ m and 35 $\mu$ m. The simulations are done at room temperature and due to the computer memory limitation the maximum number of particles used in simulations was considered as  $1 \times 10^{19}$ .

## 1.5 Contribution of the Thesis

**The following outlines the contribution made in this project:**

- **Modeling of the NW-GIS for a first time.**

The miniaturized gas sensor based on nanowires was developed for the first time in our laboratories. In this work theoretical studies and modeling the device based on these studies contributed further improvements of the device structure and its function.

- **Developing software to simulate the model.**

The software is based on an open source tools. We modified and developed the tool to accommodate our modeled device and simulate the structure and its function.

- **Studies of physical and chemical properties of various gases.**

Modeling of the device is based on very complicated physical properties of the gases. To model the ionization of the gases one needs to understand all the interactions between gas molecules.

- **Optimization of the design and structure of the device.**

The modeled device was fabricated experimentally in our laboratory. Its structure and function needs to be optimized. Doing this experimentally will be very time consuming and expensive task as several parameters are affecting the function of the device. For this we have considered all the essential parameters in our model and simulations to modify the design and function of GIS.

- **Extension of the model to detect greenhouse gases.**

In this work we have enhanced the model to measure the breakdown voltages of greenhouse gases like SF<sub>6</sub>, CF<sub>4</sub>, CO, CO<sub>2</sub>, O<sub>2</sub>, and NH<sub>3</sub>.

- **Extension of the model to detect impurities in mixed gases.**

In this work we have enhanced the model to measure the breakdown voltages of gas mixtures like Ar&Ne, Ar&He, N<sub>2</sub>&O<sub>2</sub>, N<sub>2</sub>&O<sub>2</sub>&CO<sub>2</sub>. The results are not conclusive but we have proposed alternatives to our design to detect the impurities in mixed gases.

## 1.6 Organization of the Thesis

**The remaining document is organized as follows.**

Chapter 2 reviews the ionization phenomena in gases to provide a reasonable understanding of the complex physics inside the GIS. These phenomena are important as they will lead to the induced electric field which is responsible for the breakdown of the gases.

In chapter 3 the electrostatic field inside the GIS is studied. At first, a brief description of the field enhancement at the tip of the nanowires is provided followed by an analytical work to model the local and total electric field in the designed device once with one single nanowire and then considering a multi nanowires model.

The COMSOL simulation results and analysis of various parameters effect on the GIS are covered in chapter 4.

In chapter 5 the simulation tools applied in this work are presented, starting with the studies on the XOOPIE-GIS simulation software. It follows by a discussion over the Monte Carlo Collision method implemented in XOOPIE-GIS, which is the fundamental technique in modeling the collision between the particles and target species. Various electron collision cross sections and their implementation through our developed software tool are presented in detail. The development of XOOPIE-GIS to accommodate various gases in our modeled GIS is discussed. The flowcharts of the developed software are presented in this chapter.

In chapter 6 the simulation results of XOOPIC-GIS are presented. Detection of several elemental gases as well as detection of greenhouse gases and mixed gases is discussed.

Chapter 7 covers the summary of the works done in this research project. Finally, suggestions for future works in the field bring the end of this dissertation.

# Chapter 2

## Theoretical Background

### 2. 1. Electrical Phenomena in Gases

#### 2.1.1 Ionization and Breakdown of Gases

The gas ionization is dominated by an interaction of gas molecules called 'collisions'.

Collisions determine the nature and intensity of the radiation emitted by a gas, the state and distribution of particles present in the gas.

Collisions could be elastic or inelastic. The first only modify the magnitude and direction of the velocities, while the second can also give rise to changes in internal energy or in the nature of the particles present.

In our modeled GIS device gases are identified by breakdown voltage due to the ionization of gases inside the device. In this chapter we will focus on the ionization process, especially on field ionization and electron impact ionization mechanism that lead to the breakdown of gases.

## 2.1.2 Principles of Ionization

Under normal conditions, any sample of gas contains a number of electrons and ions. Adding or subtracting an electron from the electrons cloud ionizes the neutral atoms or molecules. Mechanisms that ionize neutral gas atoms or molecules could be:

**a) *Field Ionization (FI)*** - to ionize the gases high electric fields in the range of  $10^9$ - $10^{10}$   $\text{Vcm}^{-1}$  are required. Such electric field can be obtained between two closely parallel plates or between the sharp metal needle tips or a sharp needle tip and a plate. Therefore, the formation of the high electric fields in the developed GIS device depends on the sharpness of the nanowires and separation of the tip of the nanowires from the second electrode. The intensity of electric fields necessary for FI depends upon the ionization energy of the residing atom or molecule.

**b) *Impact Ionization***, due to the collisions between energetic particles and gas molecules. Other phenomena that induce ionization are ***Thermal Ionization*** - binding energies will break due to the sufficiently high temperature, ***Photo/Radioactive-Ionization***-energy absorption from photons or radioactive particles may cause the breakdown of the energy bonds in gases.

## 2.1.3 Discharge of Gases

In a two parallel plates system due to the cosmic/thermal radiations a few electrons are always available in the subject gases. The various mechanisms presented in section 2.1.2 will enable the ionization of neutral molecules inside the system. By applying an external electric field between the two electrodes electrons are accelerated with high speed, they can excite the gas molecules and ionize them.

As the voltage increases, electron impact ionization occurs between electrons and gas molecules leading to increase the current density until the breakdown happens at  $V_B$ .

Figure 2.1 shows the current-voltage,  $I$ , gaseous discharges characteristics up to the breakdown voltage  $V_B$  [35].

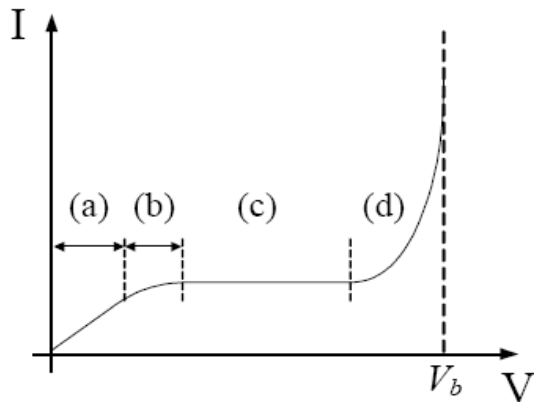


Figure 2.1  $I$ - $V$  gaseous discharges characteristic in uniform fields, up to the breakdown point  $V_b$ .

(a) Ohmic region, (b) transition to saturation, (c) saturation, (d) pre-breakdown Townsend discharge [35].

When no electric field applied, the gas is under equilibrium state and the rate of the generation of charged particles  $G$  is equal to the rate of their recombination  $R$ .

$$G=R, \quad \text{therefore } dn/dt =0 \quad (2.1)$$

where  $dn/dt$  is the net rate of charged particles production per unit volume per unit of time.

When an electric field is applied the equilibrium state is affected and the induced phenomenon is described by the different regions in Figure 2.1 as following.

(a) is an *Ohmic* region, when the applied electric field is very small and current between the electrodes is proportional to the mobility of particles (almost constant), i.e. the current density  $J$ , is proportional to the field strength  $E$ :

$$J = (n_e \mu_e + n_i \mu_i) eE \quad (2.2)$$

Where  $n_e$  and  $n_i$  are the number of electrons and ions, and  $\mu_e$  and  $\mu_i$  are their mobility's respectively.

(b, c) At a higher  $E$ , electrons and ions are neutralized once they reach the electrodes, the recombination rate  $R$  increases and affects the equilibrium. If the generation rate  $G$  remains constant, a limiting condition is reached as  $E$  increases when all the electrons and ions reach the electrodes before they have time to recombine. The total number of charges arriving at the electrodes is then equal to the number being produced, so that:

$$J = d_{gap} e \frac{dn}{dt} \quad (2.3)$$

Where  $d_{gap}$  is the distance between the electrodes,  $e$  is the electron charge, and  $dn/dt$  is the total rate of production of charged particles per unit volume, assuming all to be singly charged. Under these conditions the current density  $J$  (independent of  $E$ ) is called *saturation current density* (c region), b region is the transition between 'a' and 'c' region [35].

(d) Once the voltage increases further the current increases until the breakdown happens. The nature of the increase depends on the gas pressure and type.

Assuming that the number of electrons per second leaving the cathode is  $n_0$ , it is shown that the number of electrons reaching anode follows the following equation known as Townsend's formula [35-37]:

$$n_a = \frac{n_0 e^{\alpha d}}{1 - \gamma(e^{\alpha d} - 1)} \quad (2.4)$$

Where  $\alpha$  is called Townsend's ionization coefficient and  $\gamma$  is the number of electrons ejected from the cathode per incident positive ion. From the  $I$ - $V$  characteristics of the GIS (Figure 2.1) it can be seen that at the breakdown voltage,  $V_B$ , the current  $I$  highly increases. If in equation (2.4) the denominator is zero then the Townsend current becomes theoretically infinite. This condition is equivalent to

$$\gamma(e^{\alpha d} - 1) = 1 \quad (2.5)$$

The characteristic may therefore, be interpreted as when the voltage increases and thus electric field, in the Townsend region (region (d) in Figure 2.1) to affect  $\alpha$  and  $\gamma$  in a way that this unstable condition is reached and the current rises uncontrollably until some other limitation sets in. The condition forms a possible breakdown criterion, known as the Townsend criterion, or the sparking criterion. In this criterion free electrons existing in the ionization cell ionize the gas molecules, therefore creates more free electrons and if the process continues, the number of free electrons increases exponentially which results in the flow of a very large current that leads to breakdown.

## 2.1.4 Paschen's Law

Paschen's Law states that for uniform fields (two parallel plates), the breakdown voltage is proportional to the product of the surrounding gas pressure,  $P$ , and the gap distance,  $d$  [35-36]:

$$V_B = f(Pd) \quad (2.6)$$

From the general law of gases, the gas pressure  $P$  is related to the gas density,  $n$ , as:

$P = nk_bT$  ( $n$  is the gas density,  $T$  is the absolute temperature, and  $k_b$  is the Boltzman's constant). Therefore the breakdown voltage can be approximated as a function of the gas density [35-36]:

$$V_B = f(nd) \quad (2.7)$$

Figure 2.2 represent some experimental results for the breakdown voltage versus  $Pd$  for various gases.

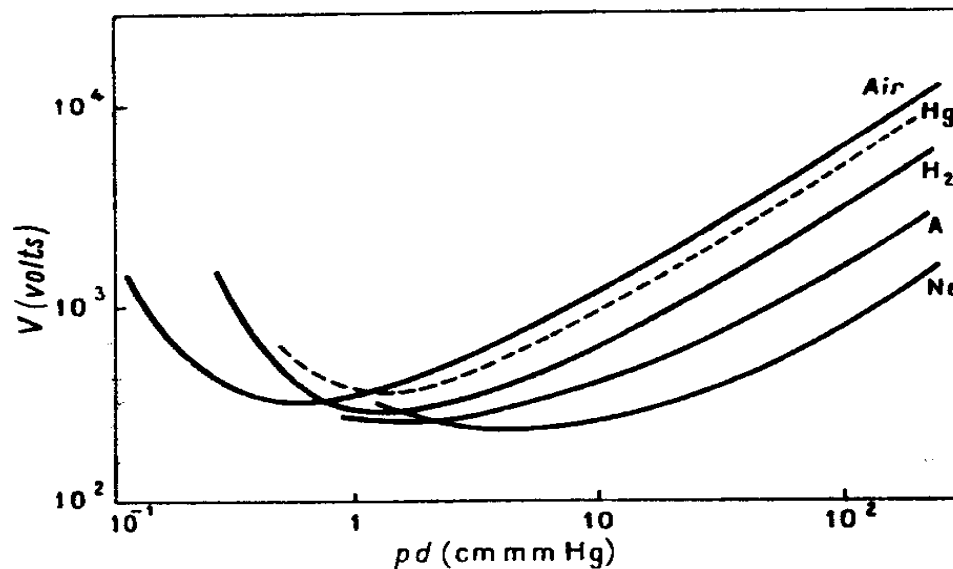


Figure 2.2 Variation of the voltage with respect to  $Pd$  (Paschen's Curves) [35].

The curves show a clear minimum, which can be explained as follows.

At low pressure, for a given distance between the electrodes, the mean free paths (MFP) of electrons are very long and the probability of collisions is very small. At high pressures, the MFP's are so short that the electrons cannot acquire enough energy between two successive collisions. Between the two, at medium pressure, the probability of the collisions between electrons and the gas molecules is maximized, generating an avalanche and eventually the breakdown of the gases at  $V_B$ . Therefore the breakdown voltage passes through the minimum of the curve.

The minimal value of  $V_B$  is called the minimum sparking, or breakdown potential,  $(V_B)_{\min}$ , and is in the order of several hundred volts. The Paschen's law can be also applied for non uniform field produced by some simple geometry like parabolic point-to-plane geometry, but not for more complex geometries.

## 2.2 Field Ionization

The techniques of field ionization (FI) consist of passing a valance electron of a gas atom or molecule having an ionization potential of  $U_I$ , through a potential barrier into a vacant energy state of the conduction band of a metal with a work function of  $\varphi$  [38-45].

Figure 2.3 shows the energy band illustration of hydrogen atom during Field Ionization [39].

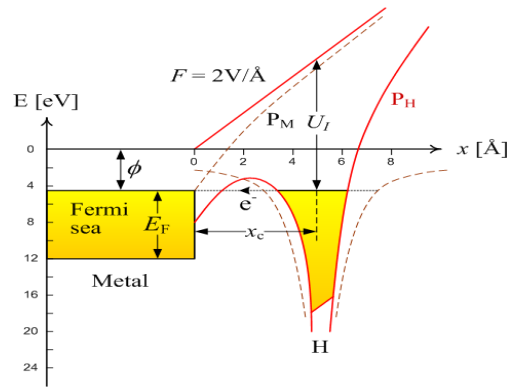


Figure 2.3 Potential energy diagram for a 1s electron of a hydrogen atom in a field of  $2\text{V}/\text{\AA}$  at a distance of  $5.5\text{\AA}$  from a tungsten surface.  $E_F$  is the Fermi level;  $U_I$ , ionization potential,  $P_M$ , atom potential;  $P_H$ , superposition of applied and pseudo image potential;  $x_c$ , critical distance. Dashed lines

The necessary condition for tunneling is that the atom is at a distance from the surface greater than critical distance  $x_c$ ; otherwise the electron energy level of the gas will be below the Fermi level and in the conduction band of the metal would be no vacant energy levels, available for tunneling.

Figure 2.4 describes the process of FI of gas atoms. The gas atoms are polarized near the nanowire tip and then attracted and accelerated to the surface by the field gradient.

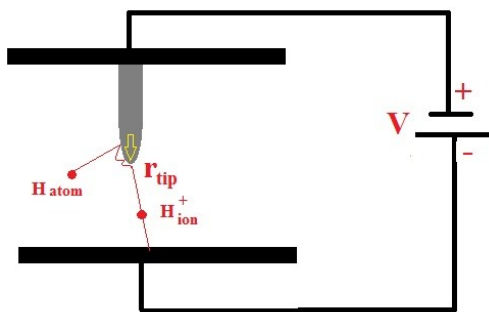


Figure 2.4 Field ionization of hydrogen atoms in a two parallel plate GIS with nanowires grown at the anode side.

As  $U_I$  is specific to any gas particle, the resulted tunneling current can be used to fingerprint the unknown gas type.

# Chapter 3

## Electrostatic Field inside a GIS

Electric field is responsible for the breakdown of gases inside the gas chamber, so detailed knowledge about it is very essential to optimize the GIS structure, the goal of this project. The study of the field emission on nanowires is done in order to obtain the highest current density at a lowest applied electric field. Investigation of the magnitude of the local electric field emitting from nanowires is the most dominant factor to achieve this goal.

### 3.1 Field Enhancement Factor at the Tip of the Nanowires

The applied electric field between two parallel plates often called the *applied macroscopic field*, is defined as

$$E_{app} = V/d, \quad (3.1)$$

where  $V$  is the voltage applied between the two electrodes and  $d$  is the gap distance between them. The applied electric field  $E_{app}$  is uniform in the gap space between the anode and cathode electrodes.

When nanowires are grown at one electrode side, strong nonlinear electric field is created in the vicinity of the sharp tips of the nanowires. One can say that the electric field is enhanced.

The upper-limit of the local enhanced electric field  $E_{loc}$  at the apex of a hemisphere is given by [46]:

$$E_{loc} = V/k_f r \quad (3.2)$$

where  $r$  is the apex radius, and  $k_f$  is a numerical constant which depends on the taper angle of the protrusion, with an average approximate value of 5. The field-enhancement factor is defined by the ratio between the local electric field  $E_{loc}$  to the applied field  $E_{app}$ , or

$$\beta = E_{loc}/E_{app} , \quad (3.3)$$

In order to estimate the enhancement factor  $\beta$ , several computational and experimental investigations are reported in the literature. These studies are reported to calculate the  $\beta$  factor value based on the geometrical model for the microprotrusion or nanoprotrusion [47-50]. These geometrical models include “hemisphere on a plane”, “hemisphere on a post” and “hemi-ellipsoid on plane”.

The model “hemisphere on a post” [47] suits the most to the grown NWs positioned in between the two parallel plates (Figure 3.1).

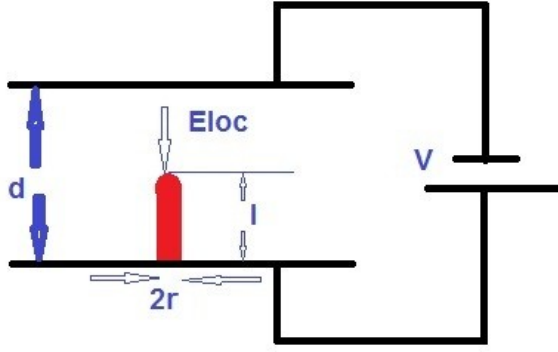


Figure 3.1 Geometrical model for a field- enhancing hemisphere-on-a-post ( $r$  = nanowire radius;  $E_{loc}$  = local electric field at the tip;  $l$  = nanowire length,  $d$  = distance between the two parallel plates;  $V$  = applied voltage between the two parallel plates)

In this model the nanowire length  $l$  is much smaller than the distance between the two electrodes ( $d$ ) in order that the field enhancement factor ( $\beta$ ) is properly estimated. Miller [49] showed that the effective value of  $\beta$  depends on  $d$ , according to the relation:

$$\beta(d) = \beta|_{d=\infty} [1 - l/d]. \quad (3.4)$$

A suitable unifying expression of various results for  $\beta$  was given as:

$$\beta \approx 2 + l/r \quad (3.5)$$

In the limit of  $l \gg r$ , equation 3.5 reduces to

$$\beta \approx l/r \quad (3.6)$$

which is used often as a rough approximation. Using this simple expression will largely underestimate the value of enhancement factor.

One of the best estimations for  $\beta$  is given by Read and Bowring [50] as:

$$\beta = 1.0782(l/r + 4.7)^{0.9152} \quad (3.7)$$

With fitted value of 0.6%. However, within a reasonable approximation the enhancement factor by many researchers is taken into account as:

$$\beta \approx 0.7 l/r \quad (3.8)$$

In practice, nanowires often exist as extended arrays and the electrostatic interaction between the nanowires will affect the overall value of the field emission. We have shown above that for one single nanowire the local electric field ( $E_{loc}$ ) is expressed as  $\beta * E_{app}$ , where  $E_{app}$  is the applied electric field between the two parallel plates and  $\beta$  is the field enhancement factor. In a device with an array of nanowires sandwiched between the two electrodes, the field enhancement factor is affected by the screening effect of the neighboring nanowires. The electric field for an infinite array of conducting structures in nano scales has been the subject of many researches [50-59].

In their work, Read and Bowring [50] analytically analyzed the local electric field of regular aligned nanosized carbon nanotubes, assuming that they are parallel and have the same length.

Keeping the same parameters, simulations were done using commercially available software based on the boundary element method. From the simulation results they implemented a mathematical approach for the enhancement factor due to the screening effect.

In their simulation they considered an array of regular nanotubes with the length of  $l$ , radius of  $r$  and intertube distances of  $s$ . Using various combinations of aspect ratio ( $l/r$ ) and ( $s/l$ ) values they have calculated the enhancement factor  $\beta$ . By calculating the field strength at the tip of the nanotubes and comparing with the applied voltage (far field value), they determined the enhancement factor  $\beta$  under various conditions. Table 3.1 shows the computed and mathematical fitted results for several combination of  $s/l$  and  $l/a$ .

Table 3.1 Values of the computed and fitted values of the enhancement factor  $\beta$  of evenly spaced linear arrays for various combinations of  $l/r$ , and  $s/l$  [50].

$s/l$	$l/r$	$\beta$
0.16	200	83.42
0.16	400	161.9
0.16	800	315.4
0.32	200	104.2
0.32	400	199.8
0.32	800	385.0
0.64	200	123.5
0.64	400	233.6
0.64	800	445.7

The values in the Table 3.1 were then fitted in a relation like [50]:

$$\beta = \beta_0 (1 - \exp(-c(l/r)(s/l)^n)) \quad (3.9)$$

where  $\beta$  is the effective enhancement factor,  $\beta_0$  is the enhancement factor of a single isolated nanostructure given in Eq. 3.6, and  $c$  is an empirical parameter introduced to fit the computed values of the enhancement factor  $\beta$ .

The fitting parameter  $c$  in Eq.3.9 was found to have a form as [50]:

$$c(x) = \ln(b * x^m) \quad (3.10)$$

With the values of  $n=0.60$ ,  $b = 3.96$ , and  $m = 0.25$ . However the  $x$  value was not reported in their publications.

As these computations are done for metallic type of CNT, we have considered that equation 3.9 should also hold for metallic nanowires used in our model.

As the  $x$ -value was not clear from the published work, based on eq. 3.9 and tabulated values in Table 3.1, we found a curve to describe a function like  $x = f(l, r)$ , (curve fitting

method using MATLAB software). The values were fitted in an equation as 3.11 and used to plot  $c$  versus  $x$  as shown in Figure 3.2.

$$x = -5.97e-010*(l/r)^2 + 8.502e-007*(l/r) + 0.003706 \quad (3.11)$$

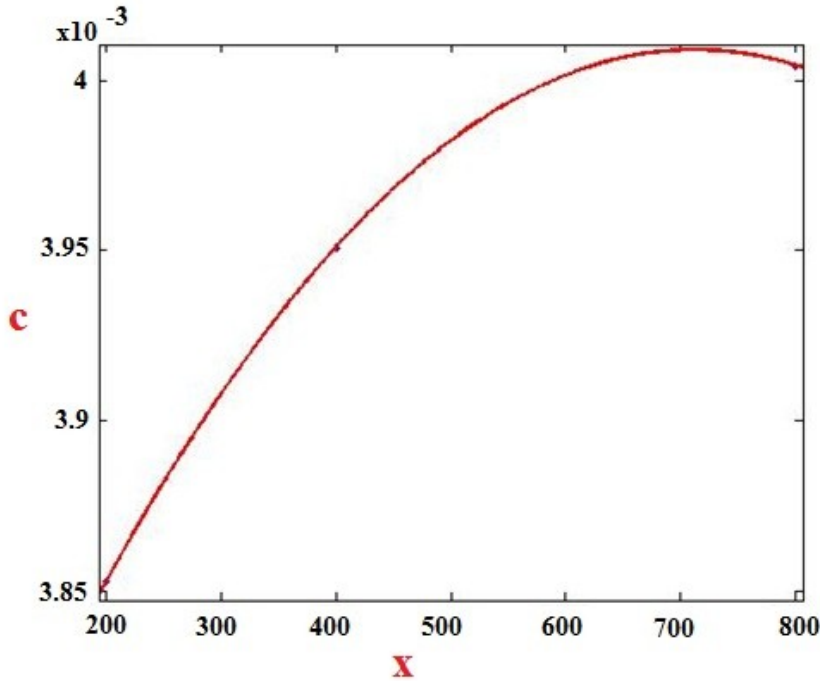


Figure 3.2 Variation of the empirical parameter  $C$  versus  $x$ , used into the fitting formula of the computed values of the enhancement factor  $\beta$ .

Substituting (3.11) and (3.10) into (3.9) the resulting value of local electric field affected by the screening effect ( $E_{loc}$ ) is plotted versus the interwire distances,  $s$ . Figure 3.3 shows that the screening effect is decreasing with the distance between the nanowires. As the distance between the nanowires increases the effective enhancement factor increases, and when  $s$  is around 4 times of the nanowires height the screening effect is minimized and remains constant. At this point  $\beta$  is almost equal to the enhancement factor of a single nanowire  $\beta_0$ .

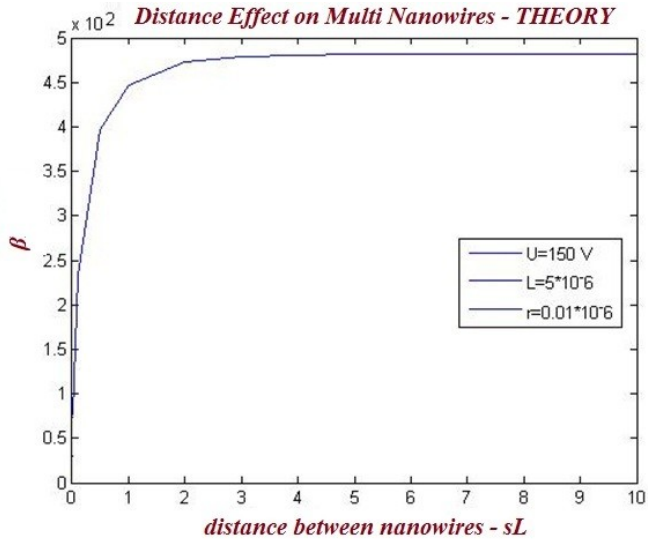


Figure 3.3 Theoretical works on screening effect versus distance between nanowires ( $sL$  is an integer number of the nanowire length).

To validate these results, we have used COMSOL to simulate the same curve while keeping all the parameters, ( $U$ ,  $l$ ,  $r$ ), the same as described in figure 3.3. The result is shown in figure 3.4.

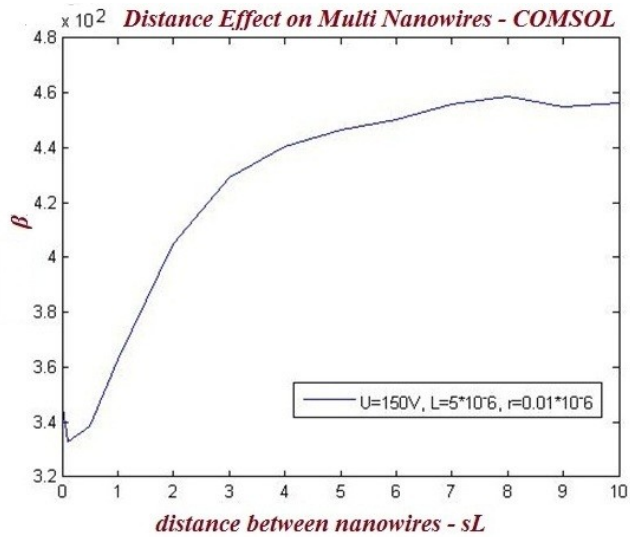


Figure 3.4 COMSOL simulations on screening effect versus distance between nanowires ( $sL$  is an integer number of the nanowire length).

Both figures show the same pattern, the screening effect decreases as the interwire distances increases. Then  $\beta$  remains constant for the large interwire distances. So, due to the electrostatic interaction between nanowires, the enhancement factor of nanowire arrays decreases with decreasing the interwire distances.

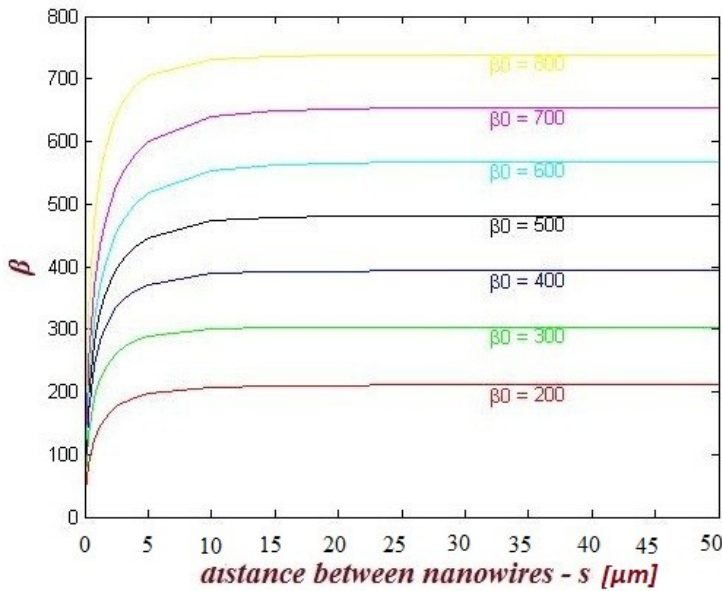


Figure 3.5 Theoretical works on screening effect versus distance between nanowires for different  $\beta_0$  factor–MATLAB simulation.

The field emission was also plotted with respect to interwire distance for various enhancement factors,  $\beta_0$ , by varying the nanowires length from 10  $\mu\text{m}$  to 40  $\mu\text{m}$  by a step of 5. Other parameters were kept constant, applied voltage of 150V, and  $r = 0.05 \mu\text{m}$ . The distance between nanowires is varied from 0  $\mu\text{m}$  to 50  $\mu\text{m}$  with a step of 5  $\mu\text{m}$ .

Figure 3.5 shows that the shape of effective enhancement factor component versus  $s$  remains the same as  $\beta_0$  changes.

Almost all the works done and reported in literature regarding the enhancement factor for nanostructure grown on an electrode, considered regular arrays of the structures,

however, in practice nanowires/nanotubes are grown in a very random structures (in terms of length, radius, and shape) and configurations. There are not many conclusive works regarding the screening effect of electrostatic interaction between nanowires available in the literature. Obviously, for the nanowires grown with a random configuration, lengths, shape and the diameter, not all of them participate in the structure of field emission and as a result the enhancement factor will be somehow different from what it was discussed above.

### 3.2 The Electric Field at Tip of the Nanowires

Figure 3.6 shows the configuration of the needle-to-plane electrode system where the needle electrode is represented by the hyperboloid surface [56].

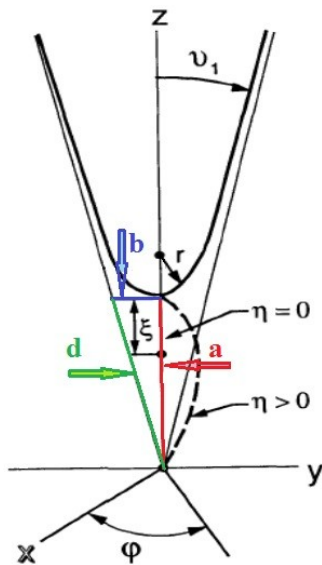


Figure 3.6 Configuration of the needle-to-plane electrode system where “ $\xi$ ” is the distance from the needle tip, “ $a$ ” is the distance between needle and plane electrodes and “ $r$ ” is the radius of the needle tip (modified from [56]).

The electric field between a needle and a plane (Figure 3.6) in the z-y plane is reported by Florkowska and Wlodek [56]. In this configuration using the relationship between the prolate spheroidal coordinates  $(\eta, \nu, \varphi)$  and the Cartesian coordinates one can write [57]:

$$\begin{aligned}x &= d \sinh \eta \sin \nu \cos \varphi \\y &= d \sinh \eta \sin \nu \sin \varphi \\z &= d \cosh \eta \cos \nu\end{aligned}\tag{3.12}$$

Where  $\eta \geq 0$ ,  $0 \leq \nu \leq \pi$ ,  $0 \leq \varphi \leq 2\pi$ , and  $d = (a^2 + b^2)^{1/2}$

According to Barbara Florkowska and Romuald Wlodek [56] the value of  $\cos(\nu_1)$  can be expressed as the ratio between the distance from needle tip to the plane electrode and the hemi focal distance d:

$$\cos(\nu_1) = \frac{a}{d} = \frac{1}{\sqrt{1 + r/a}}\tag{3.13}$$

When  $\varphi = \pi/2$  and  $\nu = \nu_1$ , the electric field in the z-y plane is given as [56]:

$$E = \frac{V}{a \sqrt{1 + \frac{r}{a}} * \sqrt{\sin^2 \eta + \sin^2 \nu_1 \ln(\cot[\nu_1/2])}}\tag{3.14}$$

where ‘V’ is the applied potential between the two electrodes, ‘a’ the distance between needle and plane electrode and ‘r’ is the radius of the needle tip.

For  $\nu = \nu_1$  and  $\varphi = \pi/2$  the parametric equations of the needle electrode in the z-y plane obtained from (3.12) are:

$$\begin{aligned}y &= d \sinh \eta \sin \nu \\z &= d \cosh \eta \cos \nu\end{aligned}\tag{3.15}$$

From equation (3.13) and (3.15) one obtains the  $\sinh^2(\eta)$  as:

$$\sinh^2(\eta) = \frac{\sqrt{\left(y^2 + z^2 - \left(a\sqrt{1 + \frac{r}{a}}\right)^2\right)^2 + 4 * \left(a\sqrt{1 + \frac{r}{a}}\right)^2 * y^2}}{2\left(a\sqrt{1 + \frac{r}{a}}\right)^2} \quad (3.16)$$

From (3.13) for  $a/r \gg 1$ , we have [56]:

$$\sin^2 v_1 = \frac{r}{a} \quad (3.17)$$

And then

$$\cot \frac{v_1}{2} \approx 2\sqrt{\frac{a}{r}} \quad (3.18)$$

Substituting (3.16), (3.17) and (3.18) into (3.14) the equation of the electric field becomes:

$$E_{loc} = \frac{V}{a\sqrt{1 + \frac{r}{a}} * \ln\left(\cot\left(2\sqrt{\frac{a}{r}}\right)\right) \sqrt{\frac{\sqrt{\left(y^2 + z^2 - \left(a\sqrt{1 + \frac{r}{a}}\right)^2\right)^2 + 4 * \left(a\sqrt{1 + \frac{r}{a}}\right)^2 * y^2}}{2\left(a\sqrt{1 + \frac{r}{a}}\right)^2} + \frac{r}{a}}} \quad (3.19)$$

Knowing that

$$z = a - \xi \quad (3.20)$$

where “ $\xi$ ” is the distance from the needle and “ $a$ ” the distance between needle and the plane electrode represented by the  $y$  axis, one can calculate local electric field with respect to  $y$  (distance from the center of the nanowire).

$$E_{loc} = \frac{V}{a \sqrt{1 + \frac{r}{a}} * \ln(\cot(2\sqrt{\frac{a}{r}})) \sqrt{\frac{(y^2 + (a - \xi)^2 - a^2(1 + \frac{r}{a}))^2 + 4 * a^2(1 + \frac{r}{a}) * y^2}{2a^2(1 + \frac{r}{a})}} + \frac{r}{a}} \quad (3.21)$$

Based on (3.21) we have used MATLAB to plot the electric field surrounding the nanowires.

We first considered a system as in Figure 3.7 with one single nanowire between two electrodes separated by a distance  $d = a + l = 100\mu\text{m}$ . A voltage of  $V = -150\text{V}$  was considered between the two plates.

The nanowire length is  $l = 25\mu\text{m}$  and radius  $r = 0.5\mu\text{m}$  and the distance between the tip of the nanowire and cathode is  $a = 75\mu\text{m}$ ;

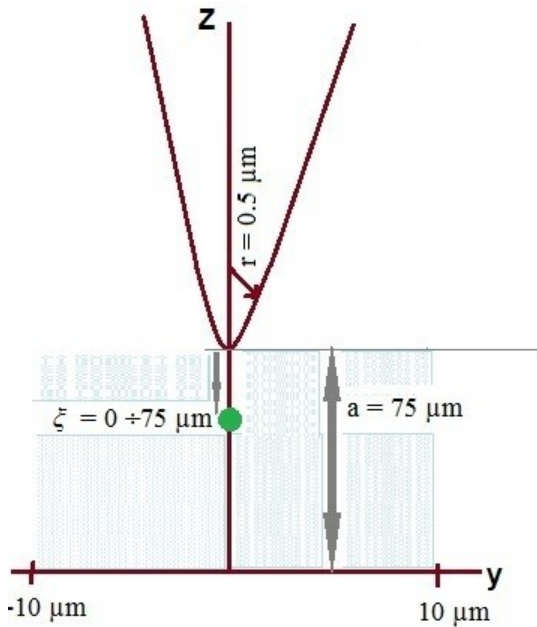


Figure 3.7 The local electric field calculated in z-y plane in a needle to plan electrode system; nanowire length  $l = 25\mu\text{m}$ , tip radius  $r = 0.5\mu\text{m}$  and gap distance  $d = 100\mu\text{m}$ .

The local electric field is computed on every  $\zeta$  point on a surface defined by the coordinates (-10, 75) for the left corner down and (10, 0) for right corner up, where  $\zeta$  (0, 0) corresponds to the point at the nanowire tip.

As it can be seen from Figure 3.8, the maximum electric field is reached at the nanowire tip, due to the field enhancement.

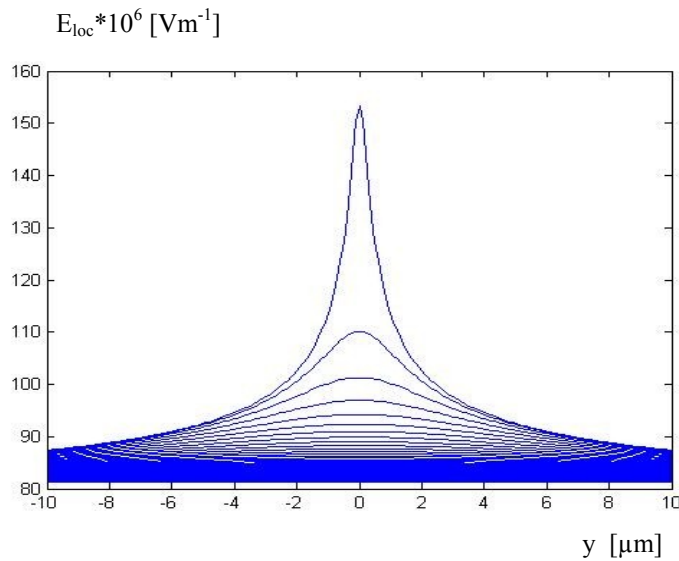


Figure 3.8 The local electric field calculated in z-y plane, for a GIS system with a single nanowire of tip radius  $r = 0.5 \mu\text{m}$ .

We have plotted the variation of electric field versus the nanowires radius. The results show that as the radius of the nanowires was increased (keeping other parameters constant) the maximum value of the electric field falls down. For the case when  $r$  was increased to 1 micron the maximum electric field was down by half as it is shown in Figure 3.9.

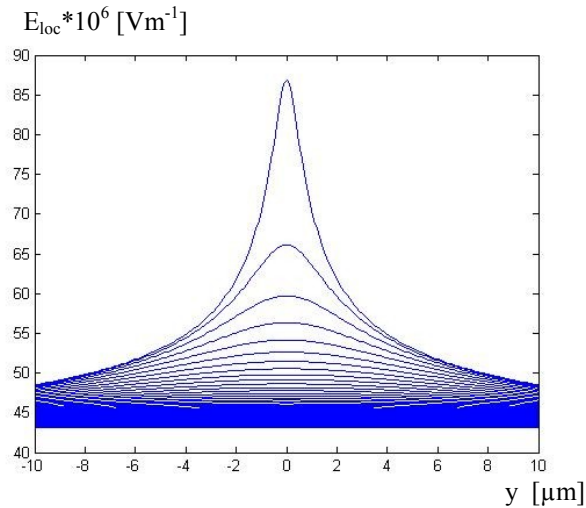


Figure 3.9 The local electric field calculated in z-y plane, for a GIS system with a single nanowire of tip radius  $r = 1 \mu\text{m}$ .

### 3.3. Screening Effect

Keeping the parameters constants as in the simulation with one single nanowire ( $d = 100\mu\text{m}$ ,  $V = -150\text{V}$ ,  $l = 25\mu\text{m}$ ,  $r = 1\mu\text{m}$ ) the simulations were carried out for an array of nanowires, with a distance of  $1\mu\text{m}$  between them.

The enhanced electric field is finally derived by multiplying the local electric field described in equation 3.21 by the effective enhancement factor,  $\beta$ , from (3.9). Using MATLAB tool the resulting electric field was plotted in the z-y plane.

As can be observed from Figure 3.10, when an array of nanowires is taken into consideration due to the electrostatic interaction between individual nanowires the total electric field is reduced (screening effect).

The resulting electric field drops down by more than twenty times.

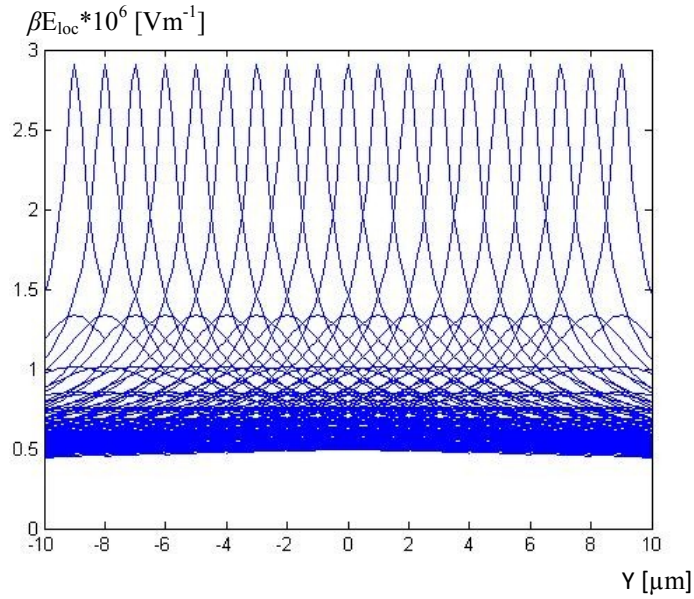


Figure 3.10 Electric field intensity versus distance from the nanowires tip calculated in z-y plane, tip radius  $r = 1 \mu m$ .

### 3.4 Conclusion

In this chapter we have presented the enhancement factor for a single nanowire. The discussion was expanded for an array of nanowires as in practice we are always dealing with large number of these nanostructures grown on one of the electrodes in the model device. The effect of electrostatic interaction between nanowire field emission is studied. It was shown that the interwire distances will influence the enhancement factor significantly. The phenomenon is called screening of the field emission, or simply screening effect. It is shown that as the distance between the nanowires decreases the screening effect increases and for the distances larger than 4 times of the nanowires

height this effect is minimized and  $\beta$  will be close to enhancement factor of a single nanowire.

The electric field between the nanowires and the opposite plate is introduced and the variation of the field emission around a single nanowire as well as around an array of nanowires is demonstrated.

# Chapter 4

## Simulations of the Modeled Electric Field generated around Nanowires

In this chapter we introduce the simulations of electric field emission of nanowires grown between two parallel plate electrodes. We have used the multiphysics simulation tool, COMSOL, to investigate the structure of the electric fields surrounding nanowires. As well, we have studied the electrostatic interaction between the electric fields emitted from nanowires (screening effects) for arrays of the nanowires.

COMSOL calculates the electric fields based on the theoretical models we described in Section 3.2. Not only the applied voltage and nanowires structure are implemented in COMSOL, but also information regarding background gas chamber, nanowires and electrodes materials, distance between the two parallel plates and shape of the nanowires tips are included in the simulation of the electric field magnitude and field lines.

The COMSOL Multiphysics is a high-precision numerical simulator used to model and study various physical, mechanical and chemical processes with high flexibility and accuracy in the fields of science and engineering.

Using this software tool we have simulated the electrostatic field inside the gas chamber under the various nanowires structures and configurations.

In these studies we have considered the amplifications of the local electric field due to the implemented nanowires.

## **4.1 Electrostatic Field inside the GIS**

In the following we have investigated the effects of various structural parameters on local and total electric field inside the GIS. In these studies we have considered the same design for GIS device as explained in section 1.1.3 and unless otherwise is mentioned a voltage value of 150V was applied between the two parallel plates, the background gas was assumed to be Ar and, the temperature was considered constant at 300K.

Our point of interest is to simulate the intensity and distribution of the electric field, responsible for breakdown of gases inside the GIS chamber.

At first we have considered only one nanowire between the two parallel plates to study the shape effect of nanowires tips. Figure 4.1 shows the electric field line intensity induced around a nanowire.

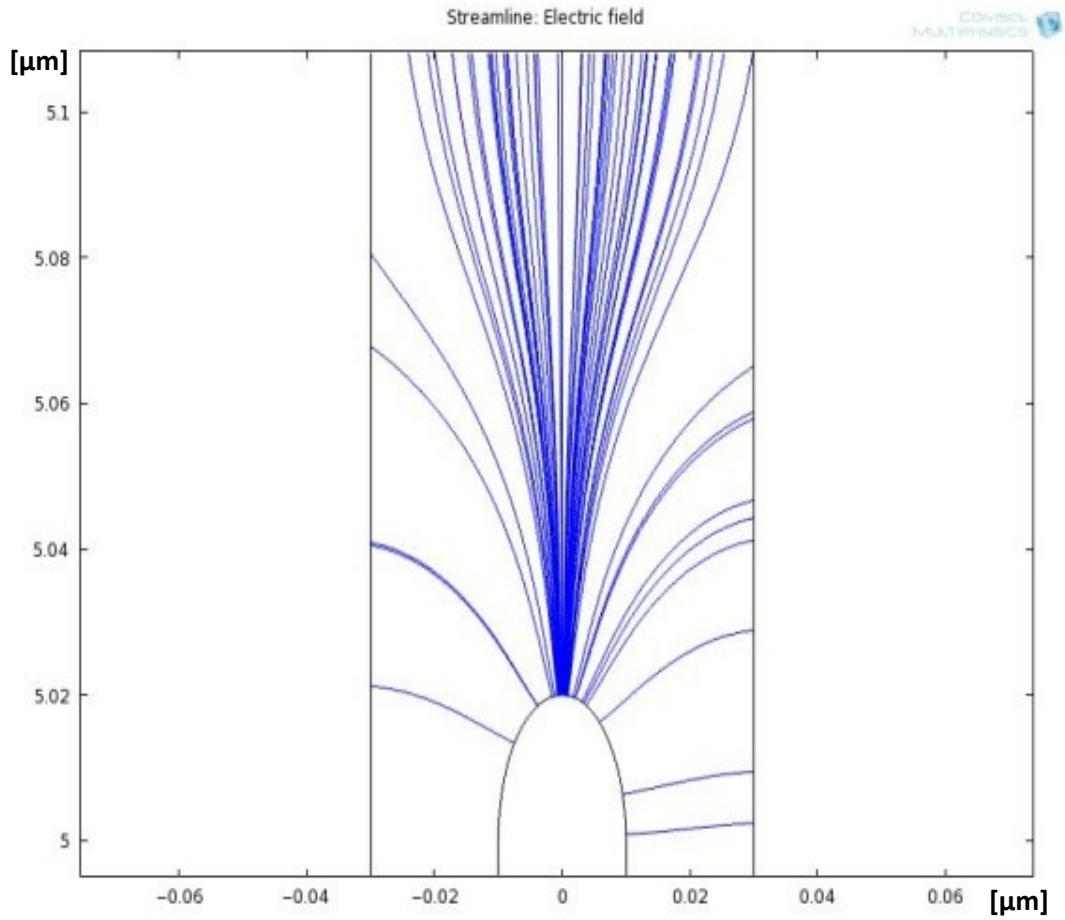
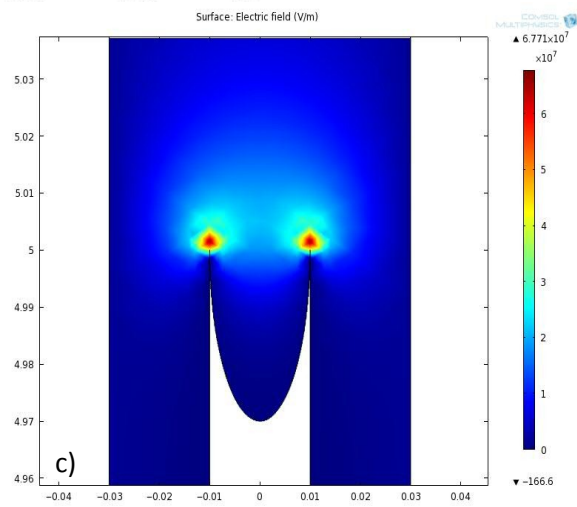
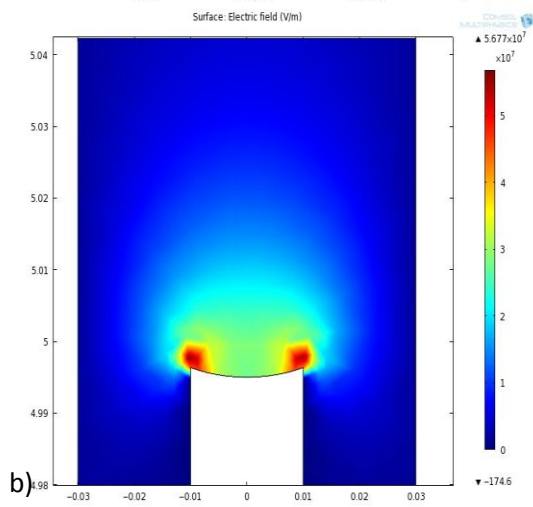
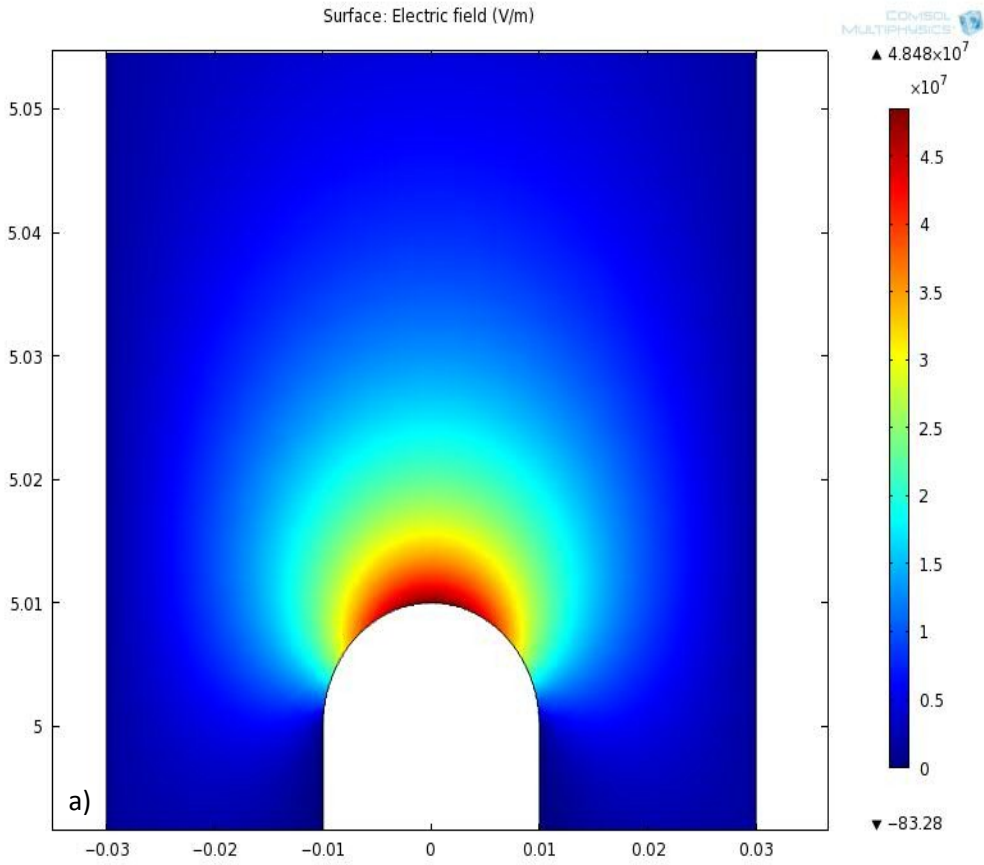


Figure 4.1 The electric field line intensity induced around a nanowire grown between two parallel plates GIS system; background gas Ar, applied voltage  $V = -150\text{V}$ ; working temperature  $T = 300\text{k}$ .

The electric field intensity lines shown in figure 4.1 are consistent with those we have calculated in Chapter 3, and plotted in Figure 3.8.

### **4.1.1 The Shape Effect of Nanowires tips.**

In this study we have modeled the nanowires tips with typical shapes produced experimentally by other researchers. The shapes include semi spherical, convex and concave ellipsoid, conical, sharp triangle and square flat. To avoid the interaction between electric field induced by individual nanowires we have only considered one single nanowire grown between the plates. The results of the simulations are shown in Figure 4.2 for various tips' shapes and sizes. The sizes of the nanowire tips are given in the figure caption. The highest values at the top of the scales on the right side of the figures, also given in Table 4.1, correspond to the (maximum) electric fields at the tip of the nanowires. As it is shown the highest electric field was generated by nanowires with sharp ellipsoid shapes (see Figure 4.2.c and Table 1). However, the distribution of electric field around the nanowires with convex circle shape is the widest compare to the other cases. This is clear from Figure 4.2.a.



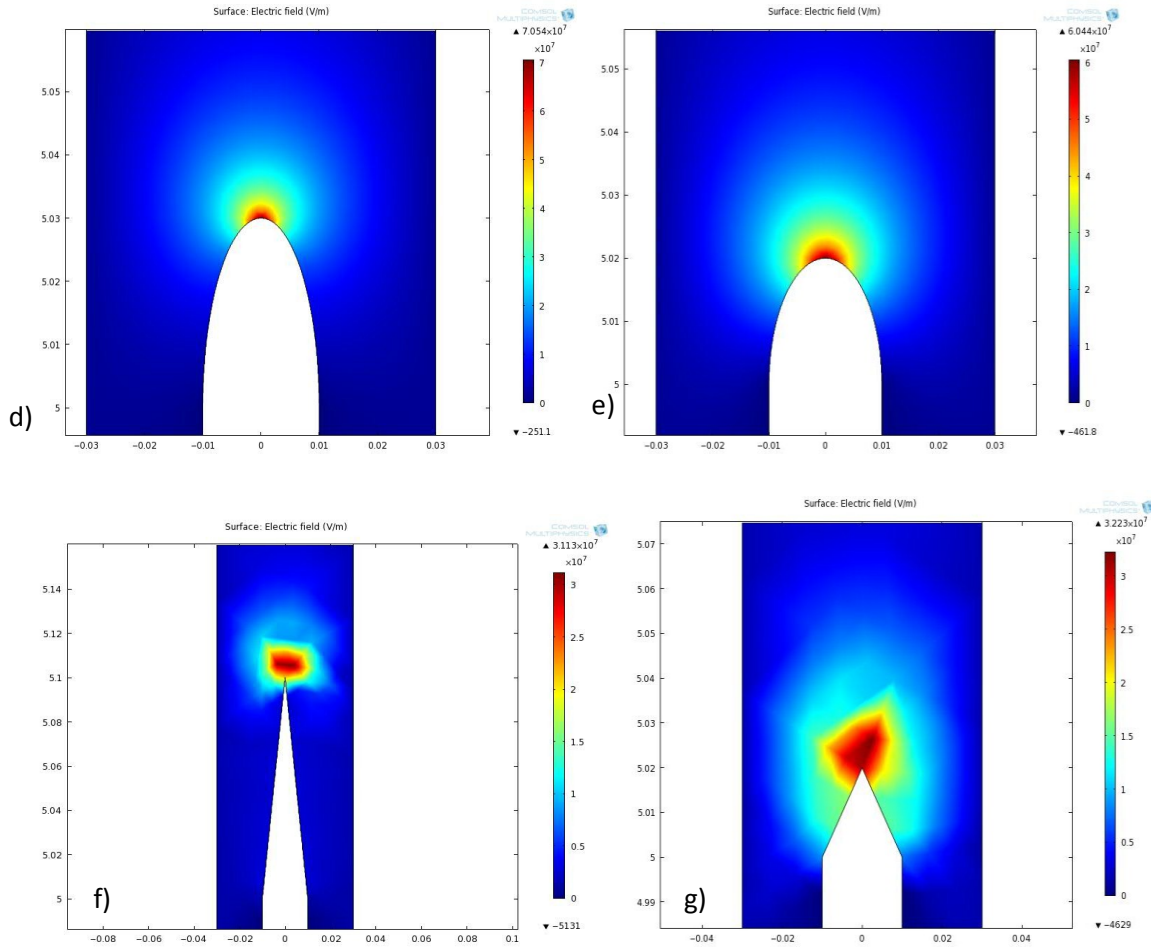
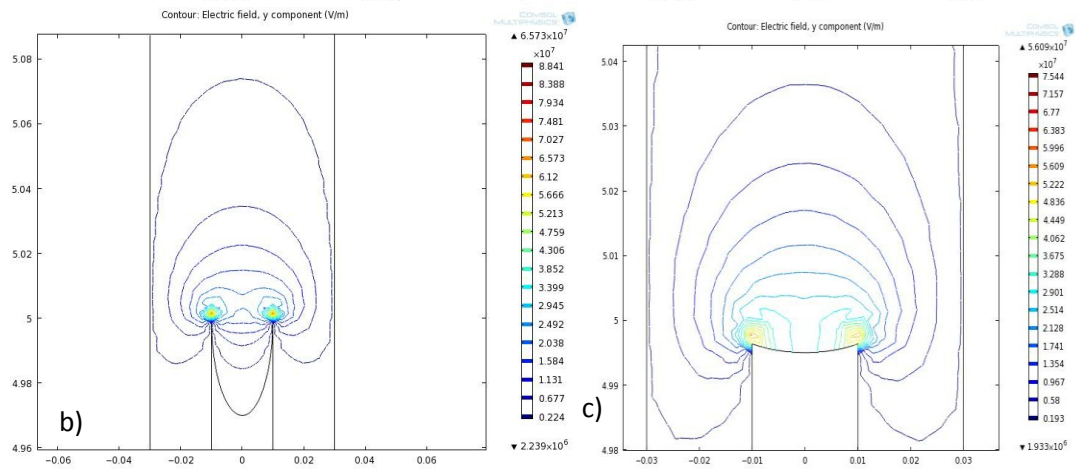
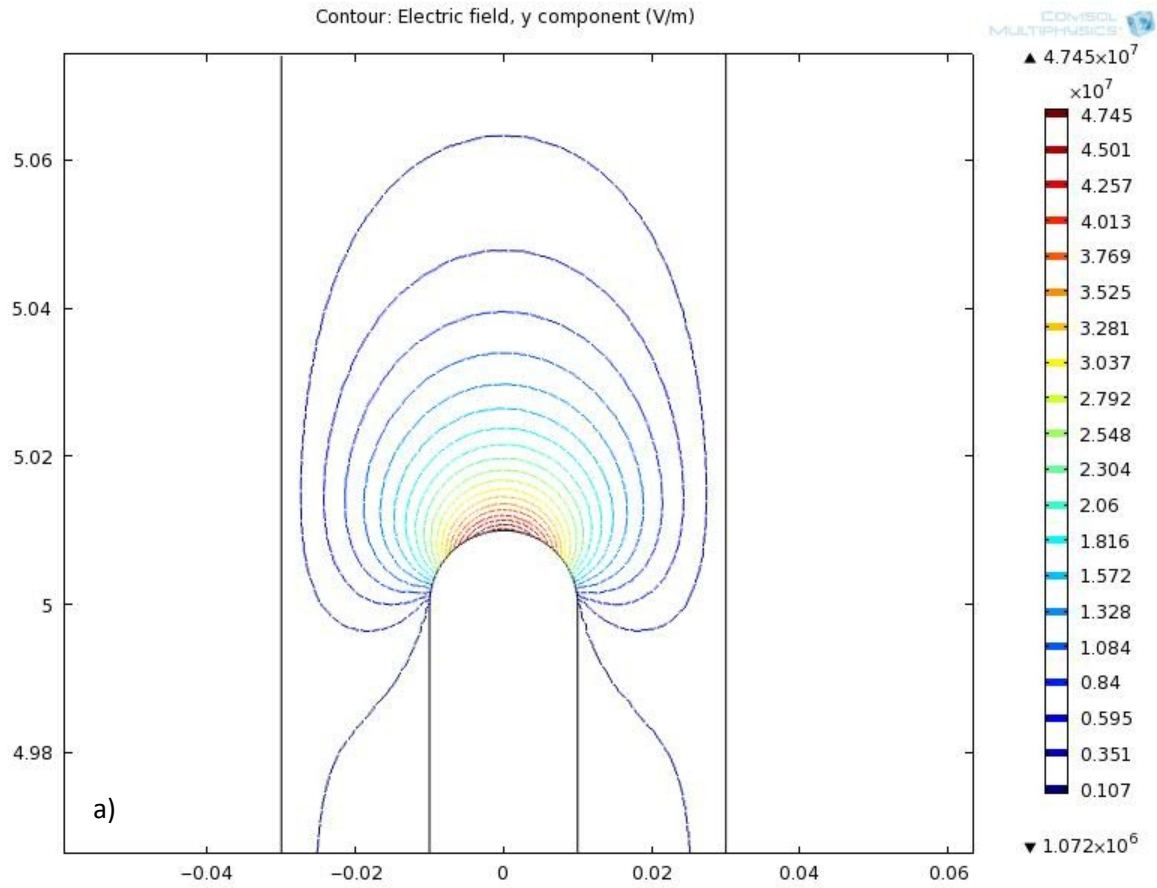


Figure 4.2 Electric field intensity for one nanowire grown between two parallel plates GIS system; background gas Ar, applied voltage  $V = -150V$ ; working temperature  $T = 300k$  a) convex circle shape tip; radius  $r = 0.01\mu m$ ; b) convex ellipsoid shape tip; semi axes  $a = 0.01\mu m$ ,  $b = 0.02\mu m$ ; c) convex ellipsoid shape tip; semi axes  $a = 0.01\mu m$ ,  $b = 0.03\mu m$ ; d) concave ellipsoid shape tip; semi axes  $a = 0.01\mu m$ ,  $b = 0.02\mu m$ ; e) concave ellipsoid shape tip; semi axes  $a = 0.01\mu m$ ,  $b = 0.03\mu m$ ; f) triangle shape tip,  $h = 0.1\mu m$ ; g) triangle shape tip,  $h = 0.02\mu m$ ;

This has been confirmed by generated electric field contours around the nanowires tip. Figure 4.3.a (for semi-spherical shape) shows the most intensive contours around the nanowires tip.



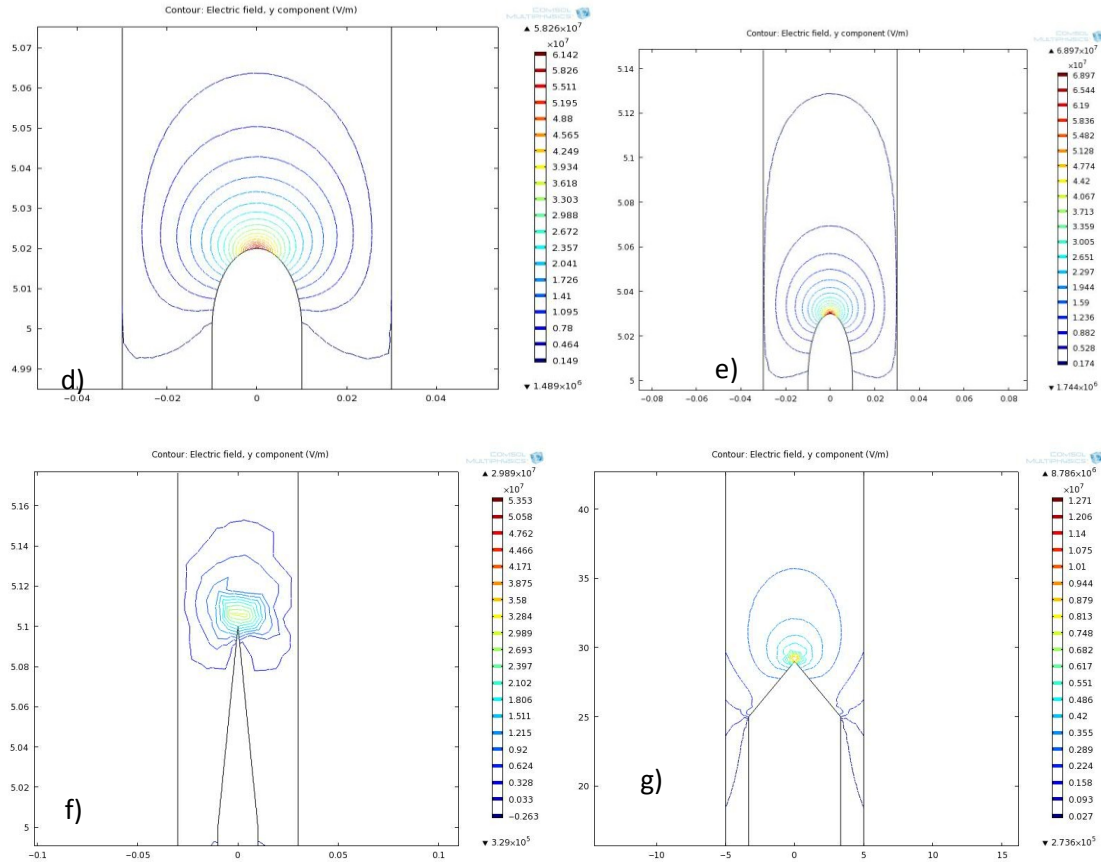


Figure 4.3 Electric field contour for different shape of nanowires tips inside a two parallel plates GIS system; background gas Ar, applied voltage  $V = -150V$ ; working temperature  $T = 300k$  ; a) convex circle shape tip; radius  $r = 0.01\mu m$ ; b) convex ellipsoid shape tip; semi axes  $a = 0.01\mu m$ ,  $b = 0.02\mu m$ ; c) convex ellipsoid shape tip; semi axes  $a = 0.01\mu m$ ,  $b = 0.03\mu m$ ; d) concave ellipsoid shape tip; semi axes  $a = 0.01\mu m$ ,  $b = 0.02\mu m$ ; e) concave ellipsoid shape tip; semi axes  $a = 0.01\mu m$ ,  $b = 0.03\mu m$ ; f) triangle shape tip,  $h = 0.1\mu m$ ; g) triangle shape tip,  $h = 0.02\mu m$ ;

Table 4.1 shows a summarized electric field intensity observed around nanowires tips with various shapes. From table 4.1 one can see that the structure with a sharp ellipsoid shape tip gives the highest electric field.

Table 4.1 Electric field intensity for different shape of nanowires tips.

Shape of the NWs tip	Electric field*10 <sup>7</sup> [V/m]
Fig. 2.f - triangle	3.113
Fig. 2.g - triangle	3.223
Fig. 2.a- convex circle	4.848
Fig 2.b - convex ellipsoid	5.677
Fig. 2.c- convex ellipsoid	6.044
Fig. 2.d - concave ellipsoid	6.771
Fig. 2.e - concave ellipsoid	7.054

## 4.1.2 The Effect of Whiskers on the Electric Field Enhancement

Although the local field intensity is larger for the nanowires with one single whisker, the electric field contours show that distribution of a large electric field is more extended for the nanowires with multi-whiskers.

During nanowires growth, it is shown [24] that the tip of the nanowires are not smooth, usually some narrow whiskers grow on top of the tips. The tinny structures are treated as the secondary amplifiers in the design of the GIS. It is shown that the local electric field, responsible for the breakdown of gases, will be increased even further if one includes the effect of these nanowhiskers [24]. For this reason we have investigated the effect of these structures on the local electric field induced at the tip of the nanowires. Starting with a nanowire having a circular shape, whiskers were grown on the top

surface. Analyses were done for one single whisker in the middle of the tip then we have carried on studying the effect of multi whiskers grown on nanowires tips (Figure 4.4 and Figure 4.5).

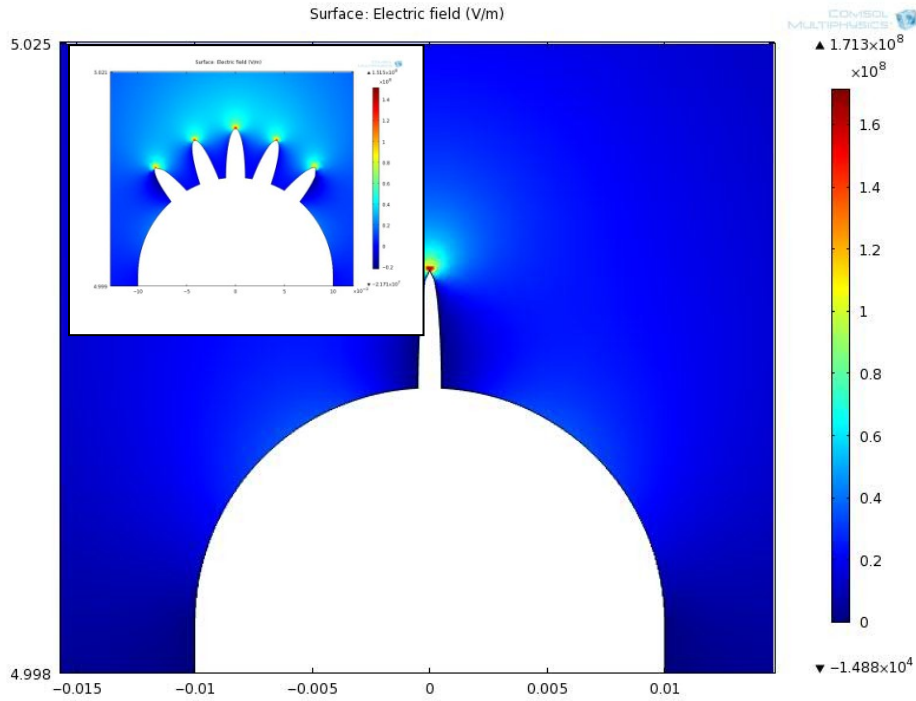


Figure 4.4 Electric field intensity for circular nanowires with grown whiskers on their tips grown between two parallel plates GIS system; background gas Ar, applied voltage  $V = -150V$ ; working temperature  $T = 300k$  ; a) one single whisker; b) multiple whiskers.

Figure 4.4 shows that the maximum electric field intensity for the structure of circular nanowires with one single whisker is  $1.713 \times 10^8$  V/m and for the multi whiskers grown on the tip is  $1.515 \times 10^8$  V/m.

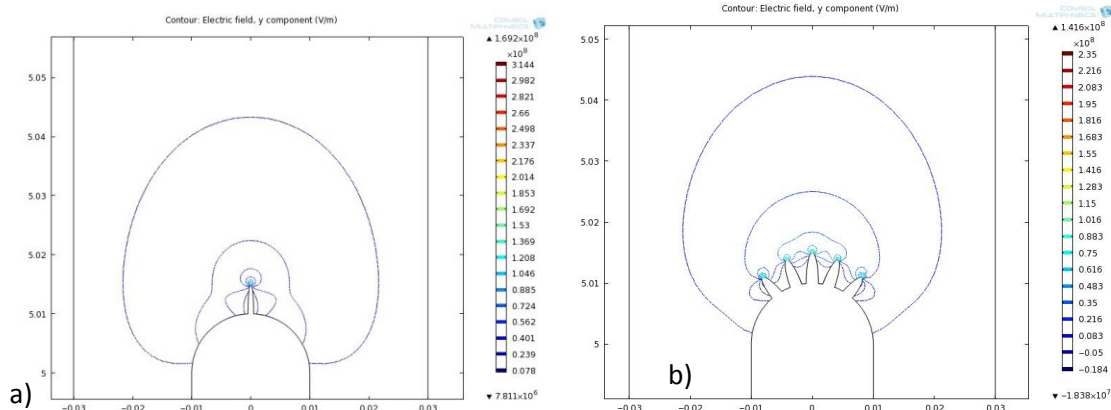


Figure 4.5 Electric field contours for circular nanowires with grown whiskers on their tips for a two parallel plates GIS system; background gas Ar, applied voltage  $V = -150V$ ; working temperature  $T = 300k$   
 a) one single whisker; b) multiple whiskers.

The simulation results listed in Table 4.2 shows that the overall electric field is significantly increased when whiskers are grown on the tip surface. The enhancement factor for nanowire with one whisker was increased by almost 4 times compare to those of nanowires without whiskers.

Table 4.2 Electric field intensity for different nanowires tips:

Shape of the NWs tip	Electric field* $10^7$ V/m	Comments
Circular	4.848	
Circular with one whisker	17.13	<ul style="list-style-type: none"> <li>the local electric field intensity increased when one nanowhisiker added to the tip;</li> </ul>
Circular with multi whiskers	15.15	<ul style="list-style-type: none"> <li>when the tip has multi whiskers, the local electric field decreased a bit compare to the tip with one whisker structure, however, as it is seen in Figure 4.5.b the overall electric field has enhanced significantly.</li> </ul>

### **4.1.3 The Effect of the Nanowires Separation on Electric Field Distribution**

In order to study the effect of interactions between electric fields induced by individual nanowires on the total electric field inside the gas chamber, we have considered a model of the device with nanowires grown with various separations. In these studies we have considered 4 nanowires with equal length and with semi-spherical tip shape.

The lengths of the nanowires are kept the same as in previous model (given in Chapter 3), equal to  $5\mu\text{m}$  and a voltage of  $-150\text{V}$  was applied between the two parallel plates.

The space between the nanowires,  $S$ , is varied from  $0.5\mu\text{m}$  to  $50\mu\text{m}$  and the corresponding values of the electric field were recorded. Figures 4.6 to 4.8 show the electric fields, electric field contours, and electric field intensity lines respectively. In these figures only a few examples of measurements are demonstrated but complete results are summarized in Table 4.3.

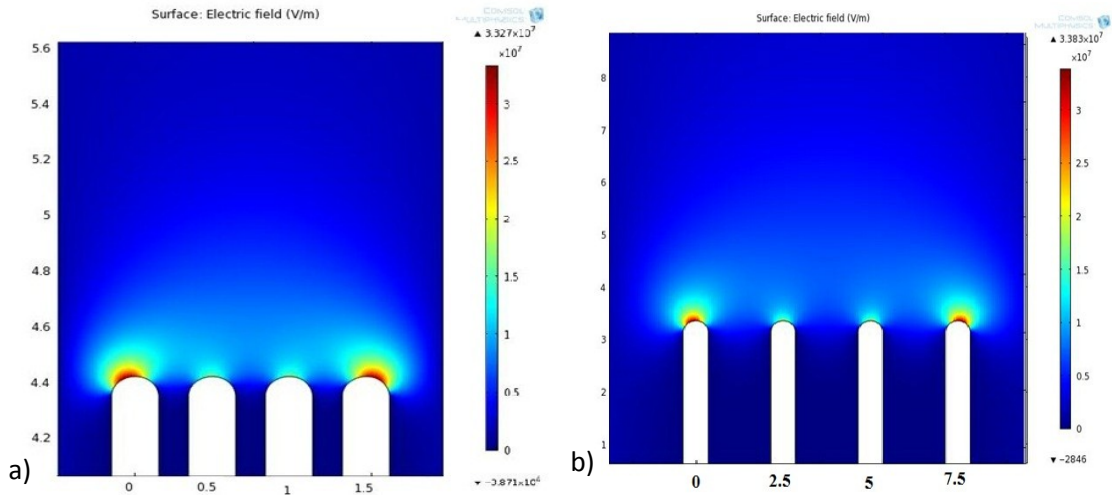


Figure 4.6 Electric field intensity variation versus distances between the nanowires grown between two parallel plates GIS system; background gas Ar, applied voltage  $V = -150V$ ; working temperature  $T = 300k$  ( $l = 5\mu m$ ,  $r = 0.01\mu m$ ,  $V = -150V$ ); a)  $S = 0.5\mu m$ ; b)  $S = 2.5\mu m$ ;

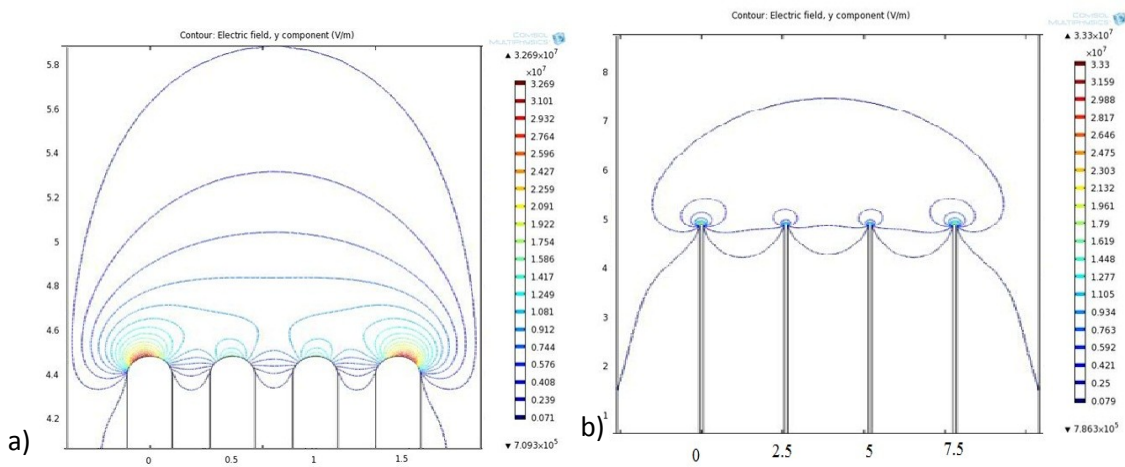


Figure 4.7 Electric field contour evolution upon nanowires distance ( $l = 5\mu m$ ,  $r = 0.01\mu m$ ,  $V = -150V$ ); a)  $S = 0.5\mu m$ ; b)  $S = 2.5\mu m$ ;

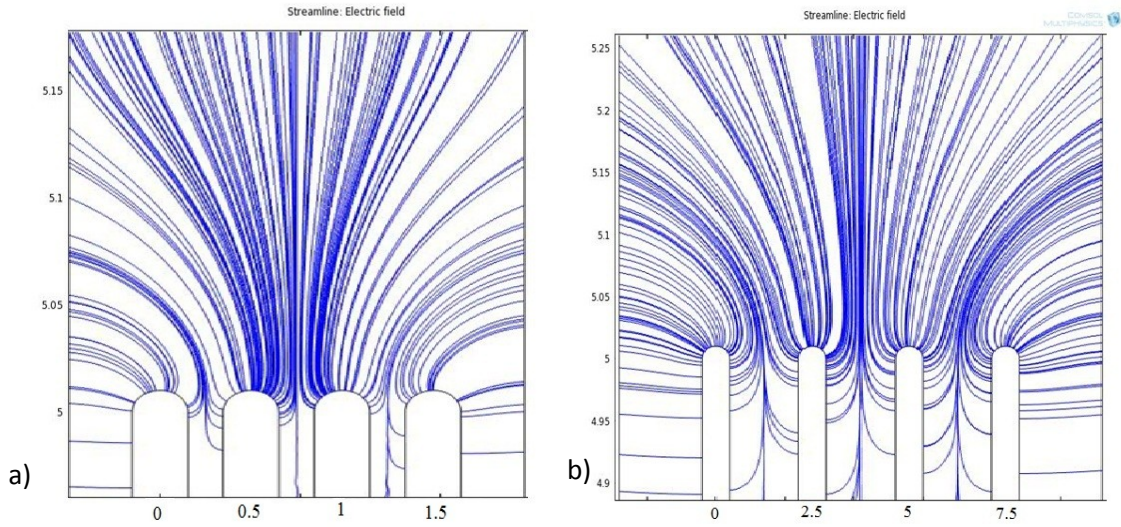


Figure 4.8 Electric field lines evolution upon nanowires distance in a two parallel plates GIS system; background gas Ar, applied voltage  $V = -150\text{V}$ ; working temperature  $T = 300\text{k}$  ( $l = 5\mu\text{m}$ ,  $r = 0.01\mu\text{m}$ ,  $V = -150\text{V}$ ); a)  $S = 0.5\mu\text{m}$ ; b)  $S = 2.5\mu\text{m}$ ;

Table 4.3 Electric field intensity for different distances between the nanowires:

Distance between nanowires [ $\mu\text{m}$ ]	Local Electric Field * $10^7$ [V/m]
0.5	3.327
2.5	3.383
5	3.632
10	4.051
15	4.291
20	4.406
25	4.464
30	4.502
35	4.559
40	4.588
45	4.552
50	4.552

The simulation results show that for an array of nanowires, the electric fields interfere with each other and change the maximum electric field at the tip of nanowires as well as its overall value- screening effect.

As it is shown in Table 4.3 the electric field at tip of the NWs increases as the interwire distance increases. However, as the separation between NWs extends over 15 $\mu\text{m}$ , the maximum intensity of the electric field increases by only a small fraction. Nevertheless, as it is shown in Figure 4.7 the distribution of the field (electric field contours) is uniformly extended in a large area between the nanowires grown with small separation between them.

#### **4.1.4 The Effect of Aspect Ratio**

In these studies we have considered the same device with four nanowires structure. We assumed the nanowires with a radius of  $r = 0.01\mu\text{m}$ . The applied voltage between the anode and cathode was again taken as -150V. The distance between nanowires was chosen as 250nm and the distance between the two parallel plates was assumed as 100 $\mu\text{m}$ . The nanowires lengths ( $l$ ) were varied between 5 $\mu\text{m}$  to 25 $\mu\text{m}$  with an increasing step of 5 $\mu\text{m}$  (Figure 4.9 - 4.11). Therefore the aspect ratio,  $l/r$ , was varied from 500 to 2500.

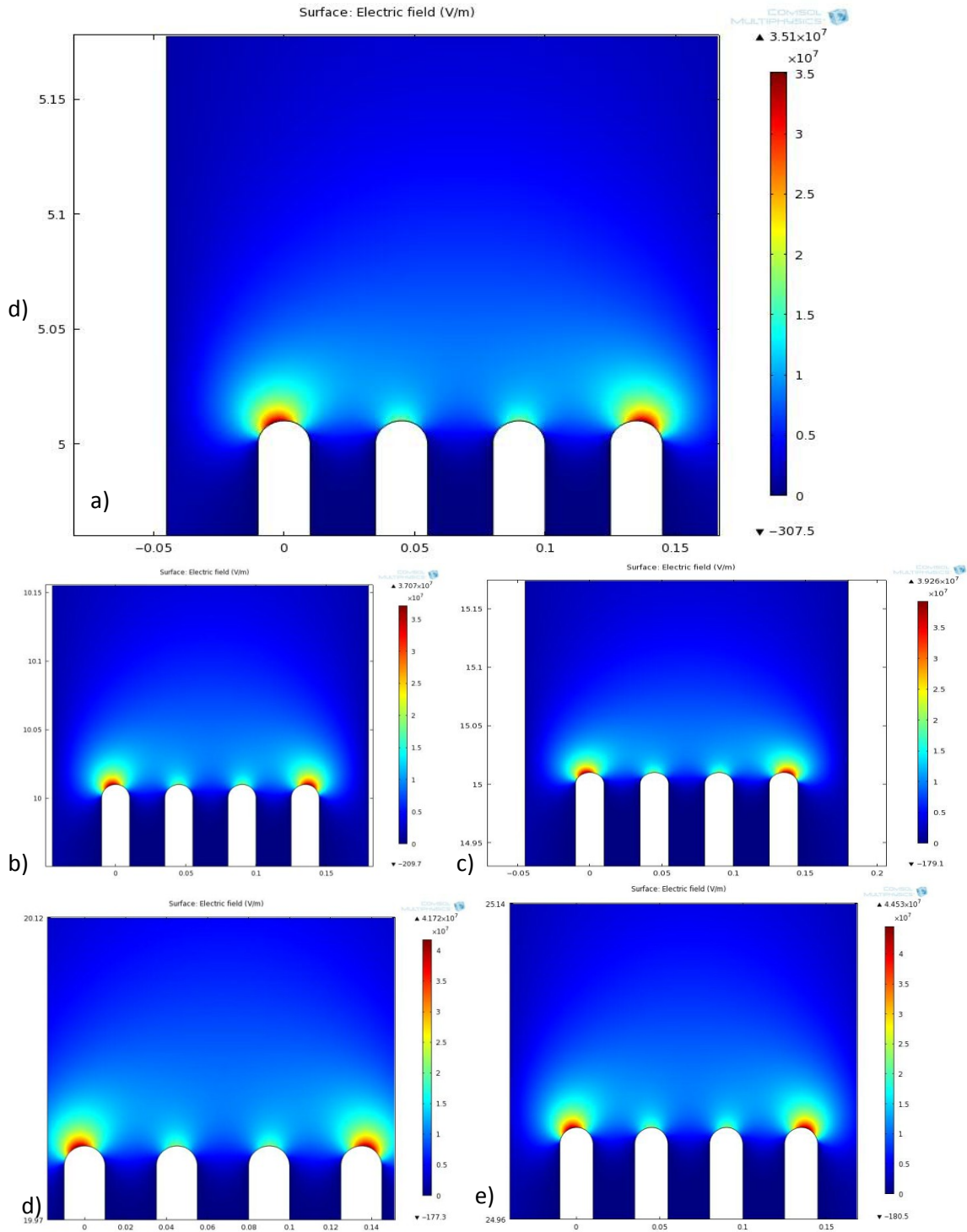


Figure 4.9 Electric field intensity evolution upon nanowires length in a two parallel plates GIS system; background gas Ar, applied voltage  $V = -150\text{V}$ ; working temperature  $T = 300\text{k}$  ( $\beta = 500$ ;  $s = 0.025\mu\text{m}$ ,  $d = 100\mu\text{m}$ ,  $V = -150\text{ V}$ ); a)  $l = 5\mu\text{m}$ ; b)  $l = 10\mu\text{m}$ ; c)  $l = 15\mu\text{m}$ ; d)  $l = 20\mu\text{m}$ ; e)  $l = 25\mu\text{m}$ ;

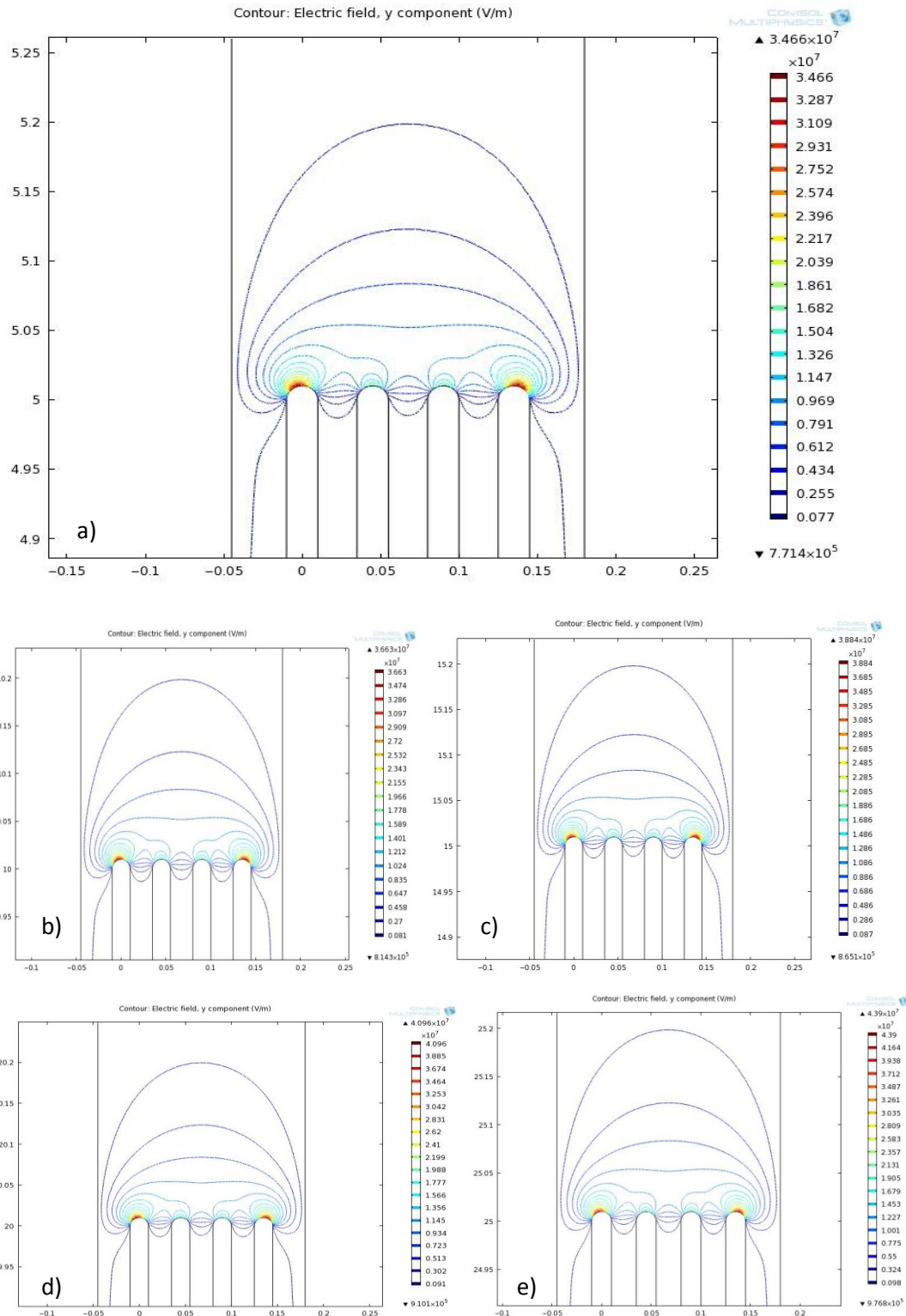


Figure 4.10 Electric field contour evolution upon nanowires length in a two parallel plates GIS system; background gas Ar, applied voltage  $V = -150V$ ; working temperature  $T = 300k$  ( $\beta = 500$ ;  $s = 0.025\mu m$ ,  $d = 100\mu m$ ,  $V = -150V$ ); a)  $l = 5\mu m$ ; b)  $l = 10\mu m$ ; c)  $l = 15\mu m$ ; d)  $l = 20\mu m$ ; e)  $l = 25\mu m$ ;

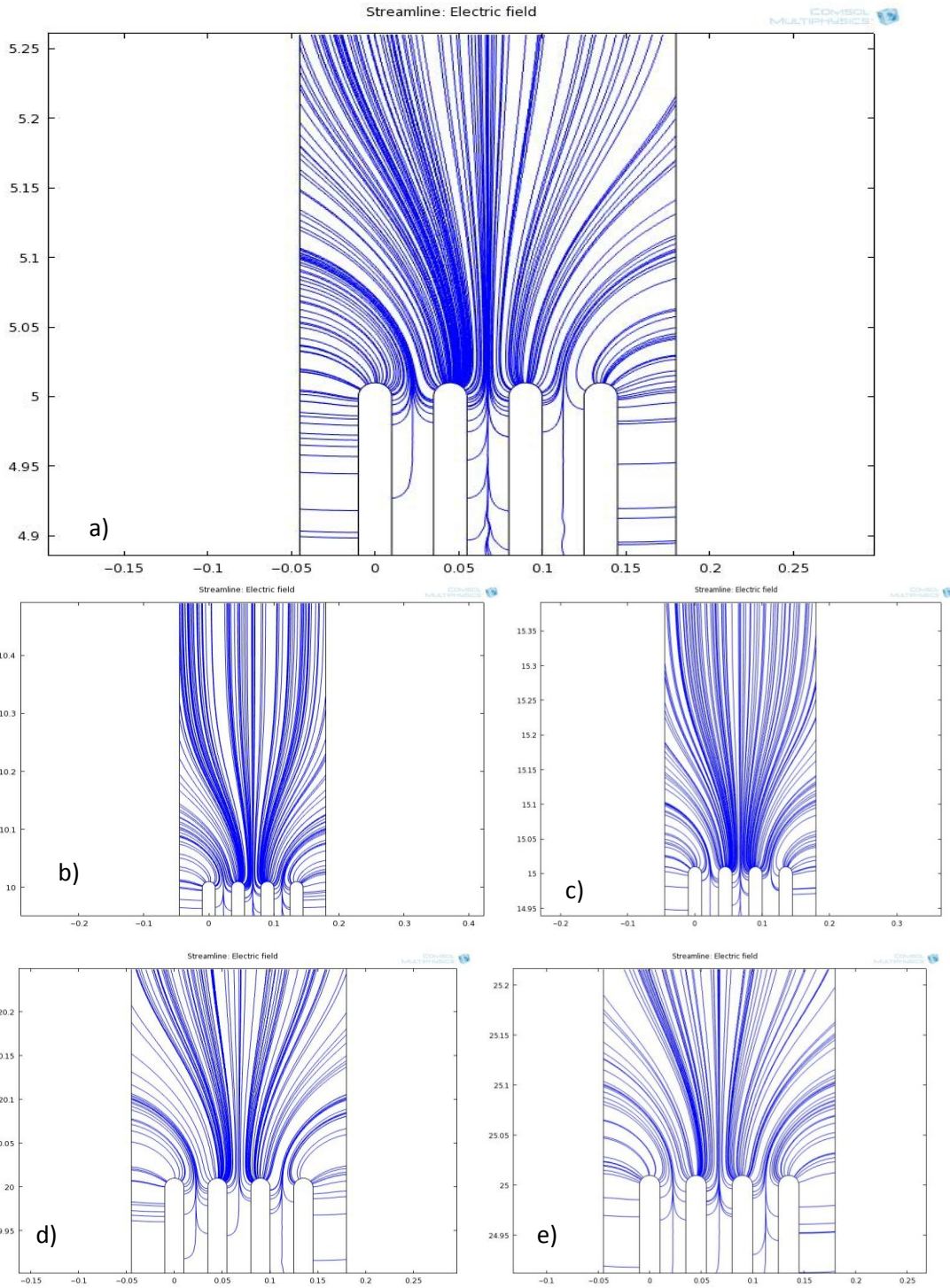


Figure 4.11 Electric field lines evolution upon nanowires length in a two parallel plates GIS system; background gas Ar, applied voltage  $V = -150\text{V}$ ; working temperature  $T = 300\text{k}$  ( $\beta = 500$ ;  $s = 0.025\mu\text{m}$ ,  $d = 100\mu\text{m}$ ,  $V = -150\text{ V}$ ); a)  $l = 5\mu\text{m}$ ; b)  $l = 10\mu\text{m}$ ; c)  $l = 15\mu\text{m}$ ; d)  $l = 20\mu\text{m}$ ; e)  $l = 25\mu\text{m}$ .

The simulation results listed in Table 4.4 show that the local electric field increases as the nanowire length increases. However, experimentally it is very difficult to grow arrays of long nanowires with very small diameters. We propose considering an enhancement factor of about 500 as a reasonable value to use in practice.

Table 4.4 Electric field intensity for nanowire with various lengths,  $l$ .

$l$ [ $\mu\text{m}$ ]	Electric field* $10^7$ [V/m]	Comments
5	3.51	<ul style="list-style-type: none"> <li>the local electric field intensity increased with nanowire length when the same gap distance and the same distance between nanowires is kept;</li> </ul>
10	3.707	
15	3.926	
20	4.172	
25	4.453	

### 4.1.5 The Effect of Parallel-Plates Distances

In order to study the effect of the distance between the two plates on the electric field we varied the distance between them from  $100\mu\text{m}$  to  $50\mu\text{m}$ , with steps of  $25\mu\text{m}$ . The nanowires are kept with the same radius  $r = 0.01\mu\text{m}$  and, at the distance  $s = 0.025\mu\text{m}$  from each other. The applied voltage between the anode and cathode was considered as  $V = -150\text{V}$ .

Simulations were done for different values of the nanowires length ( $5\mu\text{m}$ ,  $25\mu\text{m}$ , and  $35\mu\text{m}$ ).

From the simulation results given in Table 4.5, it is seen that the electric field is increasing when the gap is decreasing. Further, as it shown as the distance between the nanowires and the opposite electrode decreases the electric field will enhance even larger.

The variation of field emission versus the gap between the nanowires and the opposite electrode is shown in Figure 4.12.

Table 4.5 Electric field intensity for different gap distance. Each color corresponds to a specific gap between the plates.

NWs length $l$ [ $\mu\text{m}$ ]	$d$ [ $\mu\text{m}$ ]	Electric field* $10^7$ [V/m]	Comments
5	100	3.51	<ul style="list-style-type: none"> <li>the local electric field intensity decreased with the gap distance between the nanowires tip and the plate electrode (anode).</li> </ul>
5	75	5.138	
5	50	7.971	
25	100	4.453	
25	75	6.666	
25	50	13.32	
35	100	5.148	
35	75	8.355	
35	50	22.14	

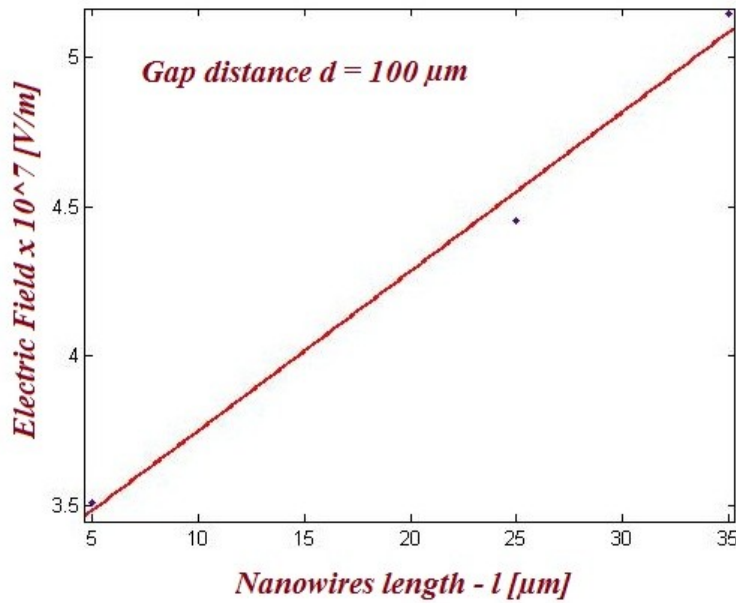


Figure 4.12 Electric field versus the gap between the nanowires and the opposite electrode.

## 4.1.6 Electric Field Study for Non Parallel Plates

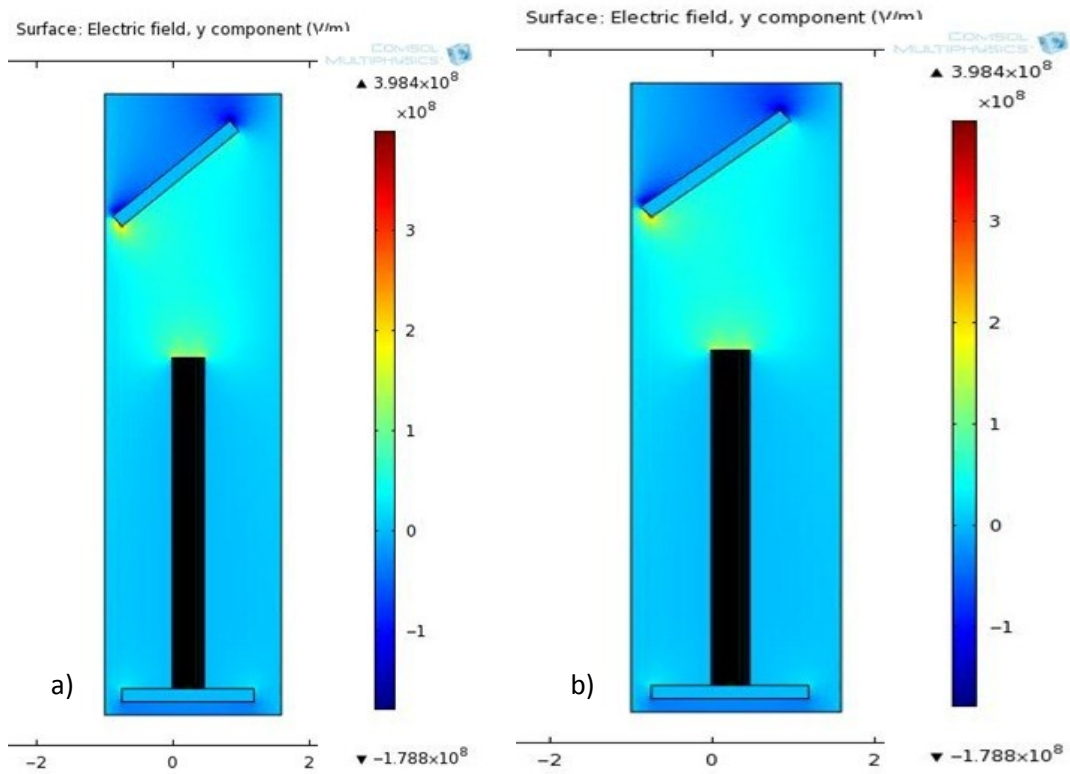
The above studies done so far we considered devices made of nanowires sandwiched between two-parallel plates. These devices can be used to detect a specific gas in any environment, however to monitor several gases at a time or to identify any unknown gas, or single out a gas among mixed gases we need to modify the design of the device. One possibility is to make a grid of these devices with implemented different circuitry on individual electrodes. By applying various potential differences on each grid in the range of breakdown voltages of target gases one can identify several gases (or odor) simultaneously. We are here proposing a simpler design to make the device suitable to detect several gases without necessity of tuning the applied voltages on the sensor. In this design the two electrodes are not parallel. The upper electrode makes an angle with respect to the lower electrode. With this technique, as the distance between the two plates is not the same along the sensor, the drop of potentials along the device varies, as it is shown in Figure 4.13. For a given angle between the two plates one can use the device to detect various gases in any environment by applying a single external voltage between the two electrodes.

In the following step, we have modified the device by changing its configuration as presented in Figure 4.13. The device parameters for the simulations were chosen as follows:

- ✓ Nanowires length  $l = 5\mu\text{m}$
- ✓ Nanowires radius  $r = 0.01\mu\text{m}$
- ✓ Number of nanowires  $n = 16$

- ✓ Distance between the nanowires  $s = 0.01\mu\text{m}$
- ✓ Shortest distance between the two plates  $d = 7\mu\text{m}$
- ✓ The voltage applied between the anode and cathode  $V = -150\text{V}$

The anode plate is designed to rotate with angles of  $0^\circ$  (parallel),  $10^\circ$ ,  $20^\circ$  and  $40^\circ$  with respect to cathode. The resulted electric field magnitudes are recorded in Table 4.6.



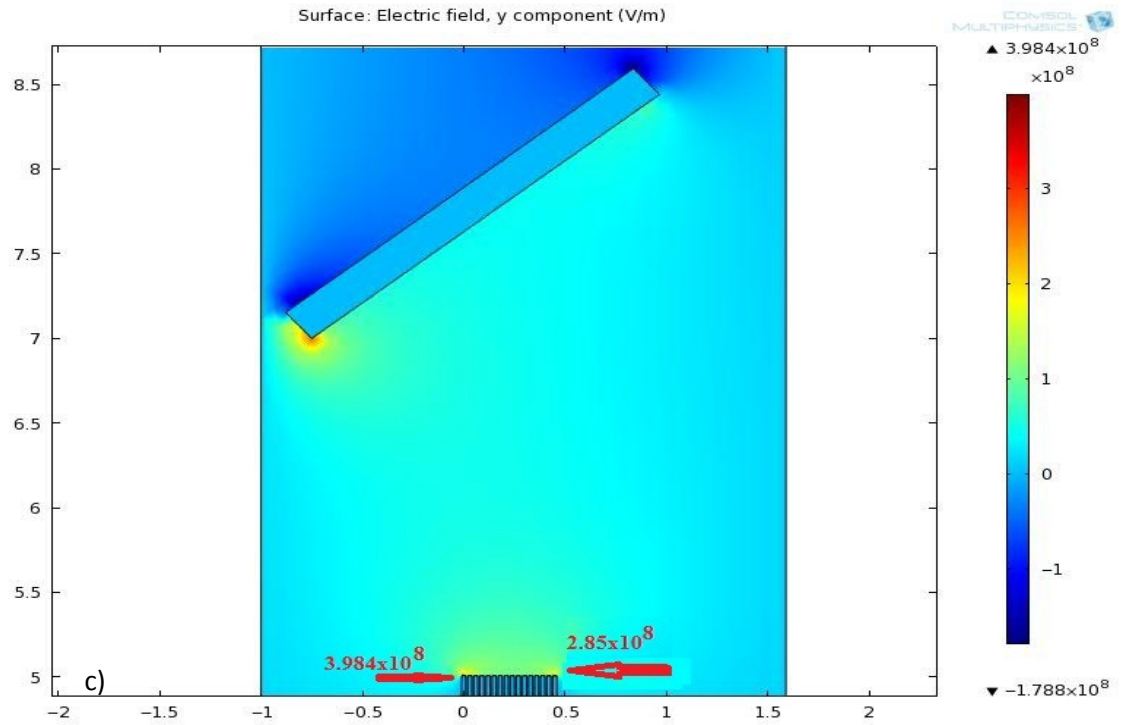


Figure 4.13 Electric field intensity evolution in a two non-parallel plates GIS system; background gas Ar, applied voltage  $V = -150V$ ; working temperature  $T = 300k$  ; a) anode is rotated by  $10^\circ$  with respect to the cathode; b) anode is rotated by  $40^\circ$  with respect to the cathode; c) detailed view of 4.12.( b).

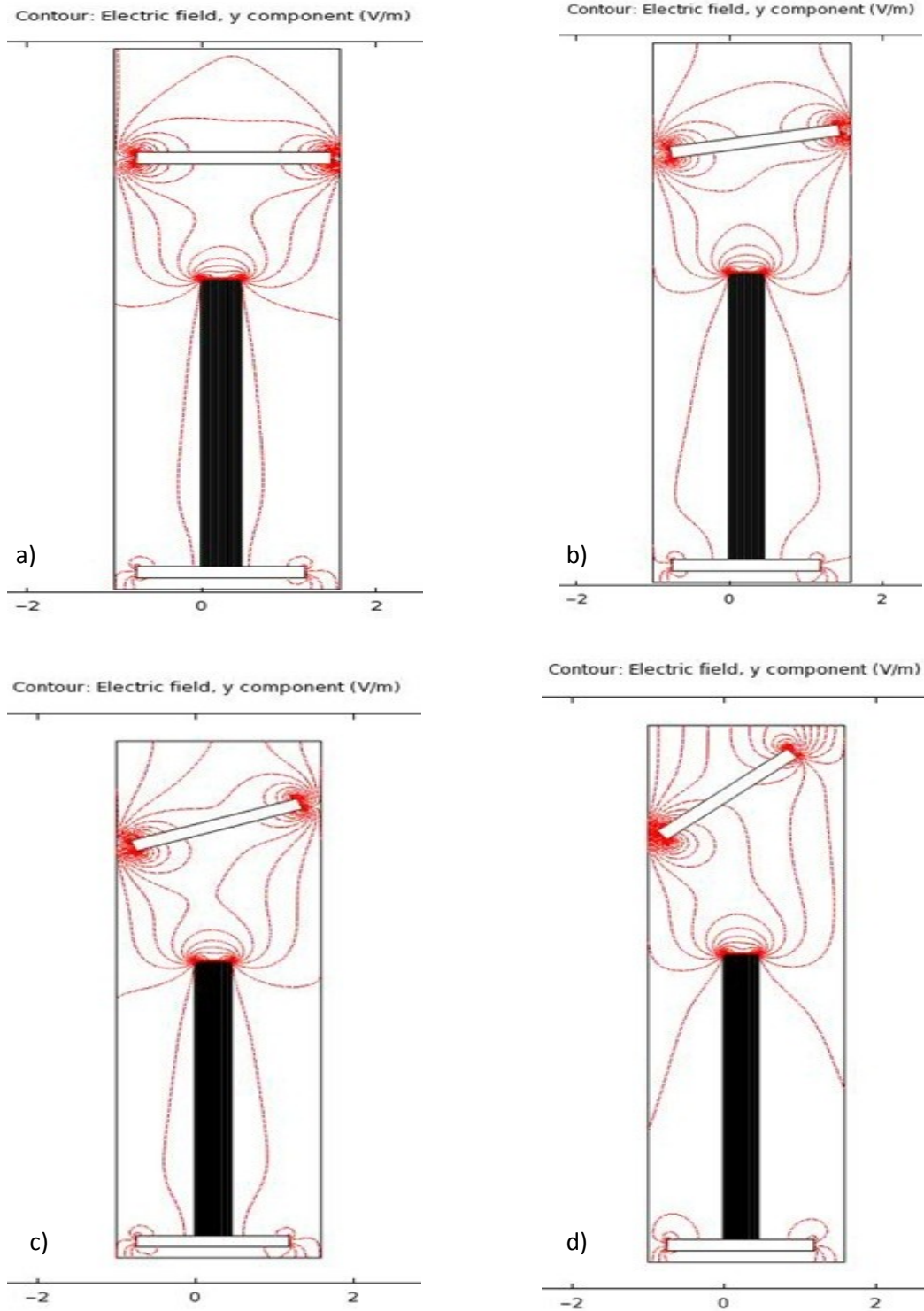
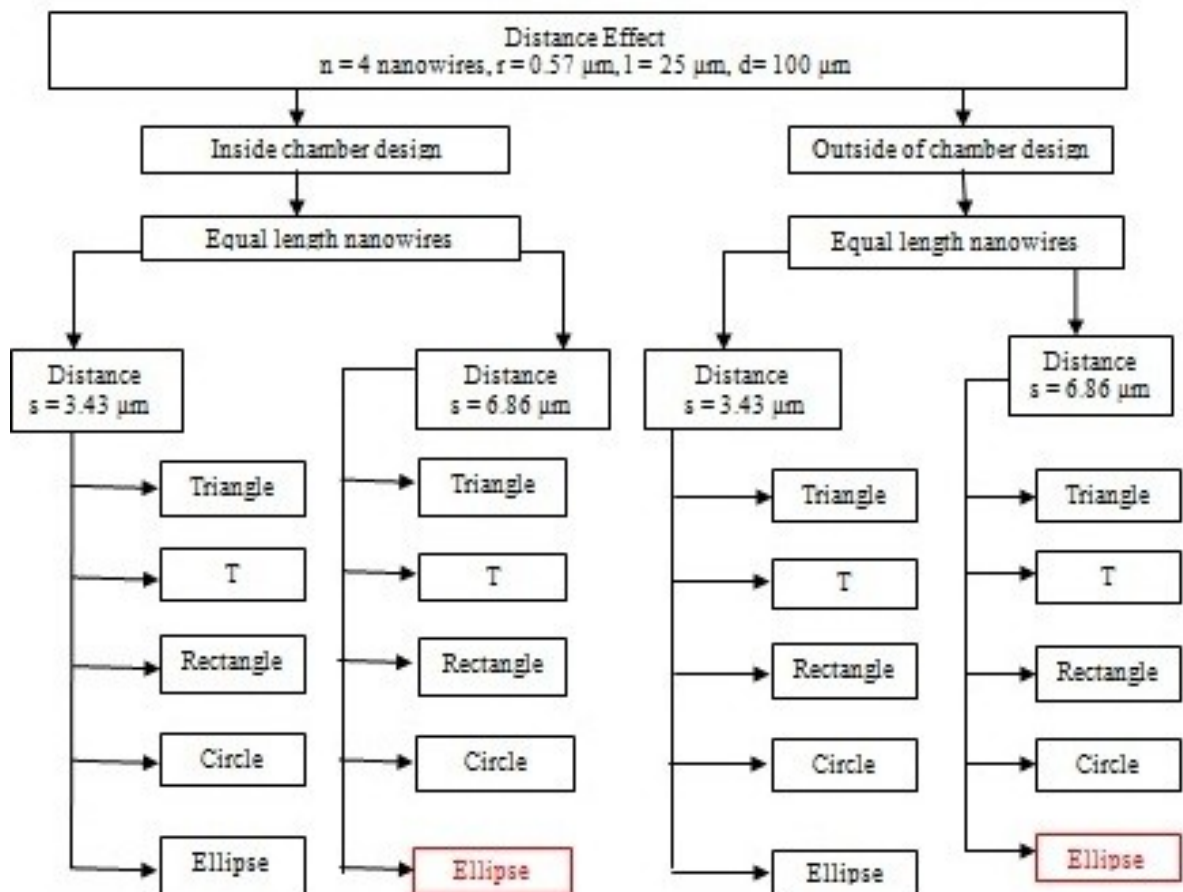
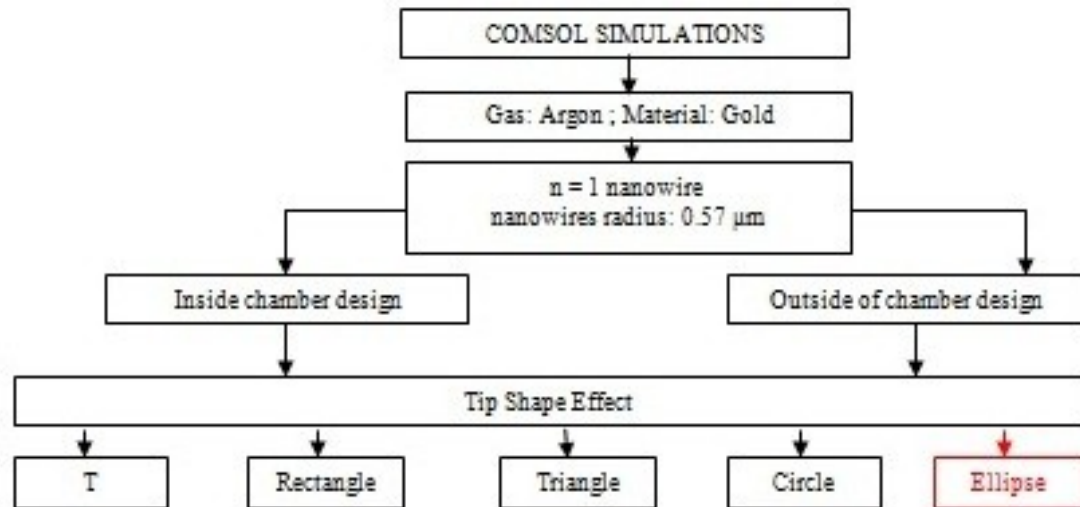


Figure 4.14 Electric field contour in a two non-parallel plates GIS system; background gas Ar, applied voltage  $V = -150\text{V}$ ; working temperature  $T = 300\text{k}$  ; a) Anode is parallel with cathode; b) Anode is rotated with  $10^\circ$  with respect to the cathode; c) Anode is rotated with  $20^\circ$  with respect to the cathode; d) Anode is rotated with  $40^\circ$  with respect to the cathode;

As one can see the electric field is varying along the x-axis (Fig. 4.13. b), although the applied voltage on the electrodes is the same. As a result the breakdown of various gases will happen at different axis along y. By tuning the angle between the two plates, and applying proper external voltage one can modify the device to detect several gases simultaneously.

## 4.2 Conclusions

In order to investigate the effect of design parameters on breakdown voltage systematically, we have developed the following two flowcharts presented in Figure 4.14. As the calculation of  $V_B$  using XOOPIE-GIS through MCC method is very time consuming, sometimes up to few days for each simulation, we have studied the induced local electric field inside the gas chamber (responsible for the  $V_B$ ) prior to application of XOOPIE-GIS. Therefore, the flow charts demonstrate the systematic simulations done on calculating the static electric field inside the gas chamber using finite element method analyzer COMSOL. The effects of nanowires tips on electric field were investigated numerically using COMSOL simulation tool (described in the beginning of this chapter). The chart in Fig. 4.14 shows the steps we have taken systematically to study the electric field intensity inside the gas chamber. We have also investigated the screening of the electric field due to the close vicinity of nanowires. The screening happens due to close vicinity of nanowires that influences the local electric field on each nanowire. In all measurements the gas was assumed to be Ar and material is chosen as gold nanowires. Finally, we have simulated the electric field inside a device with nonparallel plates.



(a)

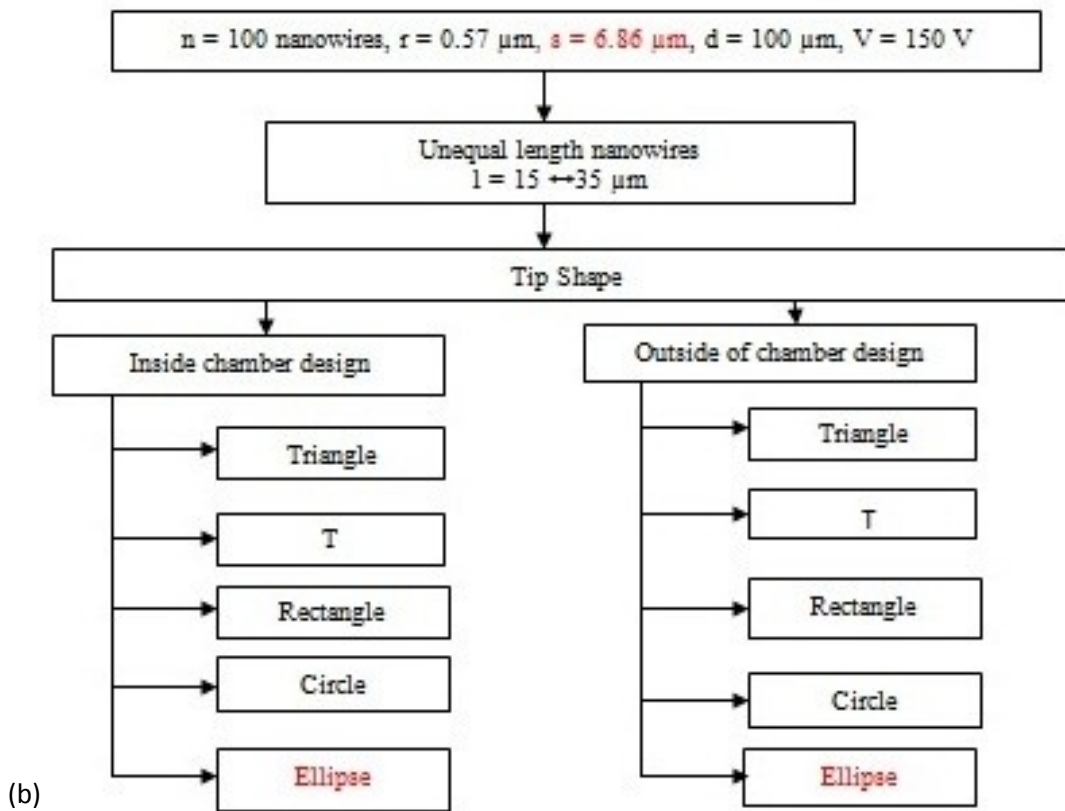


Figure 4.14 COMSOL simulations flowchart – steps taken to study the electric field intensity inside the GIS chamber.

# Chapter 5

## Simulations of the Modeled GIS Device

In this section we study the simulation of the gas ionization sensor based on the model we described in Chapter 1.

The open source XOOPIIC is a 2D particle-in-cell plasma simulation developed at University of California at Berkeley, used in modeling and simulation of plasma sources, microwave devices, laser/beam plasma interaction, etc. The XOOPIIC tool has been used by researchers since 1995 to solve problems in design, optimization and to diagnose problems faster.

XOOPIIC open codes are written in C++ including an intuitive XGrafix user interface. This interface allows the user to model and design the input file, to set the simulation parameters, to plot the data of interests and to verify at the run time the evolution of the simulation.

XOOPIIC has electrostatic field solvers for 2D geometries in x-y (slab) and r-z (cylindrical) coordinates and includes Monte Carlo collision (MCC) algorithms for modeling collisions of charged particles with a variety of neutral background gasses.

## 5.1 Monte Carlo Collisions

Particle-in-cell (PIC) Monte Carlo Collision (MCC) has become a very effective tool for modeling collisional plasma and self-sustained discharges. The conventional Monte Carlo Collision scheme calculates the time and the distance between the collisions of each particle, using random numbers. This method it is not enough for PIC, where the charged particles' trajectories are all integrated simultaneously in time. To solve the compatibility between Monte Carlo Collision method and Particle in Cell, additional collisions between charged particles and neutrals were added into the MCC package.

Over the past four decades several particle-in-cell Monte Carlo collision (PIC-MCC) simulations, were developed which include charged-particle collisions with neutral atoms [62-69].

A particularly attractive feature of this method is that it allows the simulation of physical processes, which cannot always be observed or deduced directly from laboratory experiments.

The idea of this technique is to simulate the electron motion using random numbers to account for the random nature of this motion. The free electron flights are interrupted by the scattering process and are resumed again and again, each time from a new starting point.

If a single electron is observed for a sufficiently long time, the distribution of times that the electron spends in the vicinity of different points will reproduce the shape of the distribution function [63].

The plasma region is divided by a mathematical grid in order to create charge and current densities ( $\rho$ ,  $J$ ) at the grid points, shown in Figure 5.1 [64].

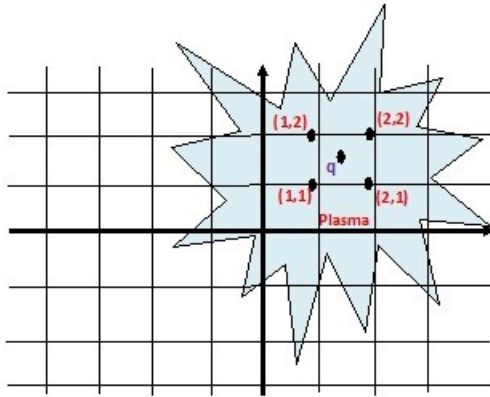


Figure 5.1 The mathematical grid set into the plasma region used by Monte Carlo Collision technique.

Figure 5.2 shows our GIS model. The GIS is schematically defined by two parallel plates as electrodes, connected in series with an external circuit.

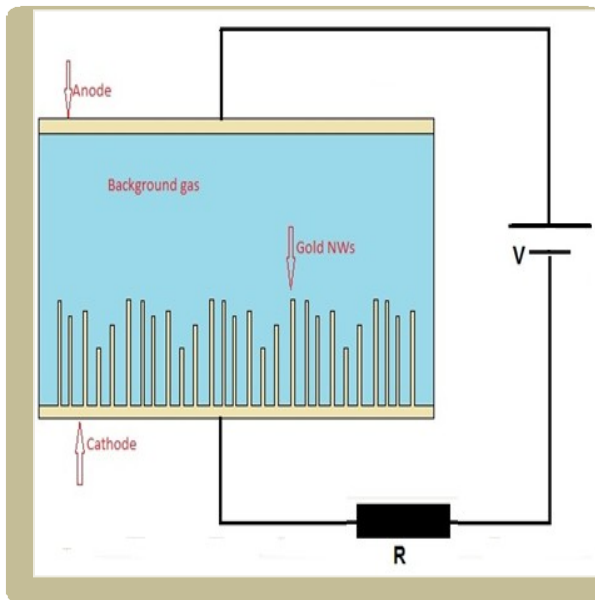


Figure 5.2 GIS Model defined as two parallel plate electrodes with nanowires grown at the cathode side and an external circuit connected in series with the device.

The external circuit consists of a constant voltage source  $V$ , and a series resistance  $R$  connected to one of the electrodes- usually the cathode, while the anode is grounded. When a sufficiently high voltage  $V$  is applied over the two electrodes the electrons and ions of the background gas are accelerated. Due to the created new charged particles, a current ( $I$ ) flows in the discharge and affects the potential difference between the electrodes.

As a result the potential difference across the electrodes is now a function of previous time step voltage and the voltage-drop across the resistance  $R$ , at any given time.

### **5.1.1. Steps in MCC Mechanism Applied to Model the Gas Discharge Inside of the GIS Device**

Due to the cosmic radiations, inside the GIS described in Figure 5.2, a few charged particles exist at any time. When a sufficiently high voltage  $V$  is applied between the two electrodes, the corresponding electric field inside the chamber,  $E = V/d$ , will create the electrostatic force applied on particles  $F = qE$ , where  $q$  is the elementary charge. Due to this electrostatic force, the electrons start moving towards the anode, changing their position and velocity.

## I. Integration of equations of motion, moving particles.

Let's consider the moving charged particles inside the gas space. The position and velocity of the charged particles within a time of  $\Delta t$  can be calculated by the equation of motions as follow:

$$m \frac{\Delta v'}{\Delta t} = F = qE; \quad \frac{\Delta x}{\Delta t} = v' \quad (5.1)$$

where  $F$  is the electrostatic force applied on the particle;  $x$  and  $v'$  are the position and the velocity of the particle respectively,  $m$  is the mass of the particle,  $\Delta v' = v'_{new} - v'_{old}$  and  $\Delta x = x_{new} - x_{old}$ .

$$m \frac{v'_{new} - v'_{old}}{\Delta t} = F_{old} = m \frac{dv'}{dt} \quad (5.2)$$

$$\frac{x_{new} - x_{old}}{\Delta t} = v'_{new} = m \frac{dx}{dt} \quad (5.3)$$

It is assumed that  $\Delta t$  is very small.

## II. Monte Carlo Collision

If at the end of the time interval  $\Delta t$  the charged particle collides with a neutral background gas, then the collisions occur and the particles velocity changes its value.

The collision probability  $P$  between the charged particles and the gas molecules is given as [68]:

$$P = 1 - \exp(-\Delta x \cdot \sigma_T(E) n_t(x)) = 1 - \exp(-\Delta t \cdot v' \cdot \sigma_T(E) \cdot n_t(x)) \quad (5.4)$$

where  $v'$  is the particle velocity,  $\sigma_T(E)$  is the total collision cross section and  $n_t(x)$  is the density of the target molecules and  $E$  is the particle's kinetic energy.

The collisions between the charged particle and the background species inside the GIS are modeled by the MCC mechanism.

To decide if a collision takes place or not in the interval of time  $[t, t+\Delta t]$  a random number  $RN_1$  is generated in the interval  $[0, 1]$ . If this number is less than the collision probability,  $P$ , then it is assumed that a collision has occurred at the end of that time step. Otherwise, the particle continues on its way, moving without any collision.

In the Equation 5.4, the total collision cross section  $\sigma_T$  is sum of the various cross sections components of the electron-molecule collisions:

$$\sigma_T = \sigma_{Exc} + \sigma_{El} + \sigma_{Ioniz} + \sigma_{Att} + \sigma_V \quad (5.5)$$

where  $\sigma_{Exc}$  is the excitation cross section,  $\sigma_{El}$  is the elastic cross section,  $\sigma_{Ioniz}$  is the ionization cross section,  $\sigma_{Att}$  is the attachment cross section and  $\sigma_V$  is the vibrational cross section.

The collision probability for each type of cross section will be:

$$\begin{aligned} P_{exc} &= \sigma_{Exc} / \sigma_T \\ P_{El} &= \sigma_{El} / \sigma_T \\ P_{Ioniz} &= \sigma_{Ioniz} / \sigma_T \\ P_{Att} &= \sigma_{Att} / \sigma_T \\ P_V &= \sigma_V / \sigma_T \end{aligned} \quad (5.6)$$

When a collision occurs, another random number  $RN_2$  between 0 and 1 is chosen to determine its type. The relationship between  $RN_2$  with the collision probabilities described in Equation 5.6 determines the collision type. For example if:  $P_{exc} < P_{El} < RN_2 < P_{Ioniz} < P_{Att} < P_V$  it means that an ionization collisions occurred during that process.

Kinetic energy,  $ke$ , is the energy that is related to the motion of the charged particle and is depending on the particle mass and velocity.

$$ke = \frac{1}{2}mv'^2 \quad (5.7)$$

When a certain type of collision occurs, the velocity and position of the particle(s) is/are changed and some energy is lost. The amount of this energy loss is equal to the threshold energy required for that specific type of collision. For example, when a charged particle collides with a gas molecule if an excitation collision occurs, the kinetic energy after collision is equal to:

$$KE = ke - Eex \quad (5.8)$$

Where  $ke$  is the energy prior to the collision and  $Eex$  is the threshold excitation energy necessarily to excite the charged particle from one state to another.

The new velocity after the collision,  $v$ , is defined as:

$$v = \sqrt{\frac{KE}{EnergyScale}} \quad (5.9)$$

Where  $KE$  is the kinetic energy after collision and  $EnergyScale$  is defined as:

$$EnergyScale = \frac{1}{0.5m} \quad (5.10)$$

where  $m$  is the mass of electron.

### III. Weighting

Using the new position and velocity after the particle collision calculated in steps II, the charge density and current density are computed as below:

$$\rho(x, y) = \sum_{n,m} \frac{q_{n,m}}{\Delta x \Delta y} W(x, y) \quad (5.11)$$

$$J(x, y) = \frac{\rho(x, y)}{\Delta t} \quad (5.12)$$

where  $W(x,y)$  is an interpolation scheme (explained in Figure 5.4). To model our GIS by the PIC-MCC mechanism, the space charged between the two electrodes is divided into a certain number of cells, by a mathematical grid as shown in Figure 5.3 [69].

The charge and current density are calculated at the grid points, by weighting the total charge inside of one cell to the corners of the cell.

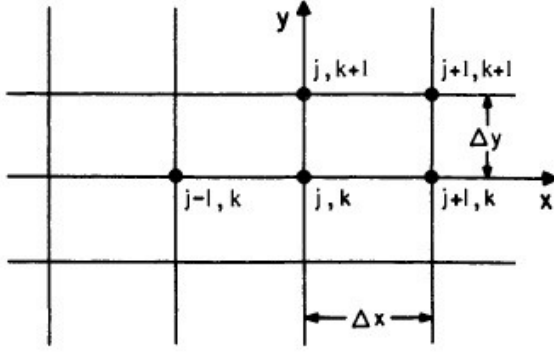


Figure 5.3 Two dimensional grids used to weighting the charge density at the grid points [69].

The weights of the charge density into the grid points are given by [69]:

$$\begin{aligned} \rho_{j,k} &= \rho_c \frac{(\Delta x - x)(\Delta y - y)}{\Delta x \Delta y} \\ \rho_{j+1,k} &= \rho_c \frac{x(\Delta y - y)}{\Delta x \Delta y} \\ \rho_{j+1,k+1} &= \rho_c \frac{xy}{\Delta x \Delta y} \\ \rho_{j,k+1} &= \rho_c \frac{(\Delta x - x)y}{\Delta x \Delta y} \end{aligned} \quad (5.13)$$

where  $\rho_c$  is the cell charge density ( $q/\text{area}$ ). Figure 5.4 describe the geometrical interpretation of the weighting scheme used in Equations 5.13, which is called the bi-linear interpolation or area weighting. If a charged particle  $q$  lies inside of the grid cell, by bi-linear interpolation the area 'a' is assigned to grid point A, area 'b' to grid point B, etc.

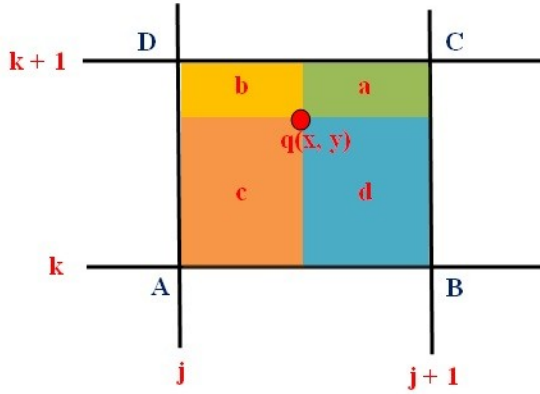


Figure 5.4 PIC bilinear interpolation interpretation; areas are assigned to grid points with the particle center located at  $q(x, y)$ .

#### IV. Integration of field equations on grid

Solving the Poisson equations the potential  $\Phi$  and electric field strength  $E$  is acquired:

$$\nabla^2 \Phi = -\rho(x, y) \quad (5.14)$$

$$E(x, y) = -\nabla \Phi \quad (5.15)$$

At the grid points the  $E(x)$  as shown in Figure 5.5 is [69]:

$$(E_x)_{j,k} = \frac{(\Phi_{j-1} - \Phi_{j+1})_k}{2\Delta x} \quad (5.16)$$

Similarly for  $E_y$  we have:

$$(E_y)_{j,k} = \frac{(\phi_{k-1} - \phi_{k+1})_j}{2\Delta y} \quad (5.17)$$

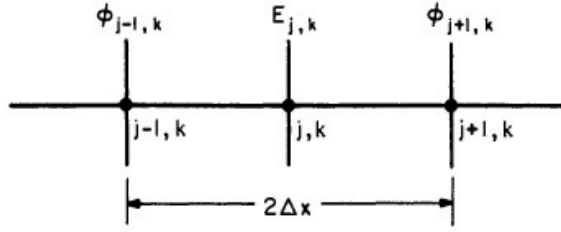


Figure 5.5 Location of the  $E_{j,k}$  in relation with  $\phi_{j,k}$  at the grid points of the mathematical grid used in Monte Carlo Collision technique [69].

So the Poisson equations at the grid points become:

$$\nabla^2 \phi(x, y) = -\rho(x, y) = \rho_{j,k} + \rho_{j,k+1} + \rho_{j+1,k+1} + \rho_{j+1,k} \quad (5.18)$$

From equation (5.15), applying the Gauss' theorem on a cell, the total charge  $q(x,y)$  is determined as:

$$\oint \epsilon_0 E dx dy = q(x, y) \quad (5.19)$$

Due to this charge, a current ( $I$ ) flows in the GIS chamber and affects the potential difference between the electrodes. The new potential difference alters the electric field between the two electrodes, causing to change the force,  $F$ , on the particles and a new cycle of process. The cycles will continue until the potential drop on the electrodes is large enough to cause the breakdown of the gases.

That above model is calculated using MCC. The following chart presented in Figure 5.6 shows the steps are done during one cycle of the process described above.

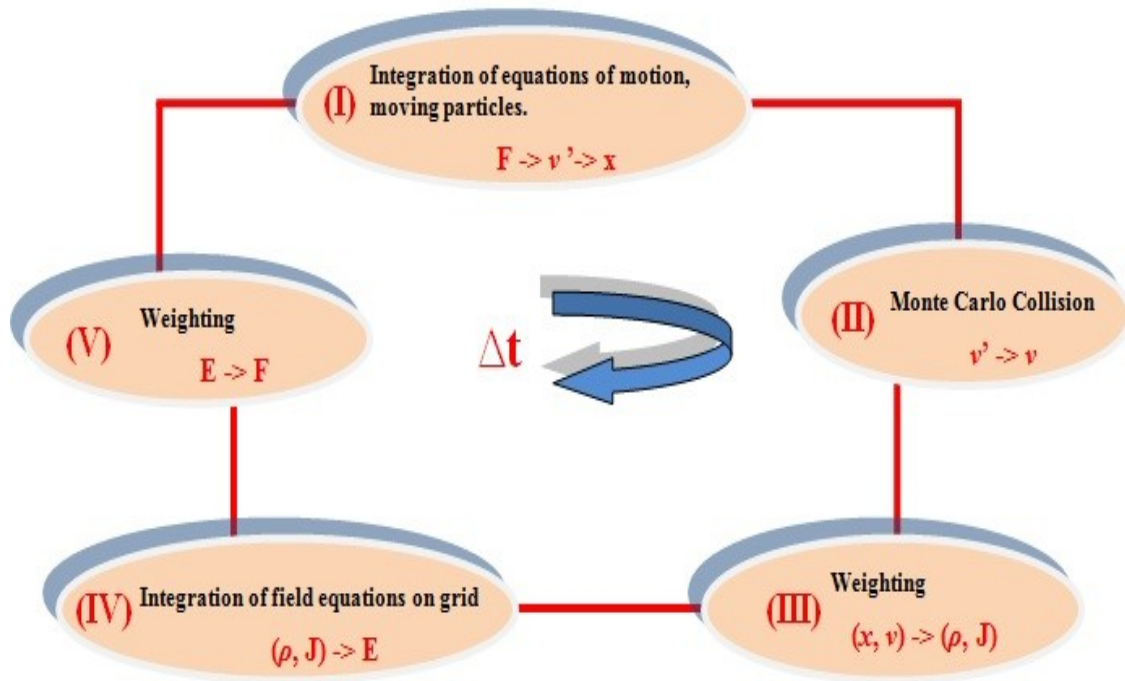


Figure 5.6 Classical PIC – MCC schemes

## 5.1.2 The Breakdown of the Device

After each time step the potential difference across the electrodes is changed causing a voltage drop across a series resistance,  $R$ , implemented externally to the device. The electronic circuit including the external series resistance is shown Figure 5.2 and the voltage computation by our simulation tool is shown in the flowchart in Figure 5.7.

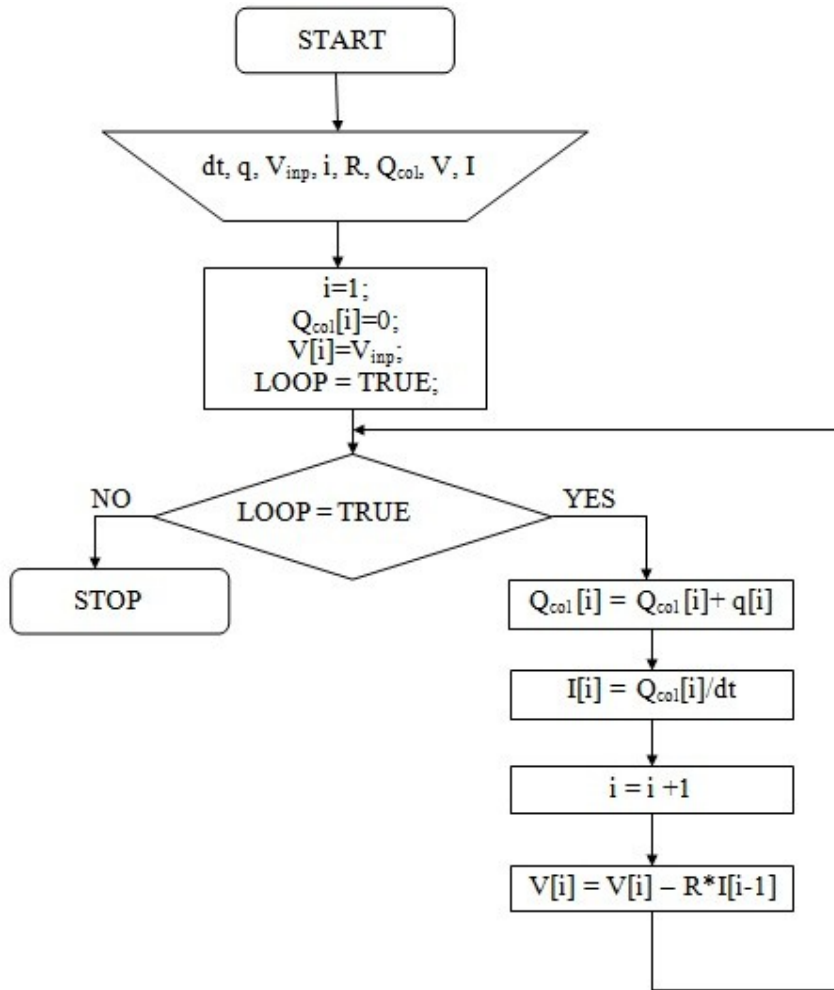


Figure 5.7 Flowchart of the voltage computation between the two electrodes GIS affected by the potential drop across the series resistance  $R$ .

The input of the computation consists of the applied voltage between the two parallel plates of the device,  $V_{in}$ , the series resistance  $R$ , the particle charge  $q$ , and of the calculation time step  $dt$ . Beside the above inputs related to the device, computational variables are also implemented as well. At the first step the potential drop across the series resistance  $R$  is initialized to the applied voltage  $V_{in}$ . In each “ $j$ ” cycle ( $j$  is a counter that keeps the number of cycles in each time interval of  $dt$ ), the total collected charge  $Q_{col}$  will induce a current flow through the circuit,  $I$ . This current causes a potential drop

across R ( $Vr = RI$ ).  $Vr$  depends on the charges accumulated on the electrodes and is changing with time. The breakdown of the gases happened when there are enough charges accumulated on the electrodes to make the resultant potential drop on the device equal to  $V_B$ .

## 5.2 XOOPIC Monte Carlo Collisions Package

As a starting point we used a uniform distribution of all particles inside of the GIS chamber. The main particle types used in this work are: neutrals, primary electrons, secondary electrons, single charged positive ions and single charged negative ions. Primary electrons are ejected from the nanowires tips by field emission and move toward the anode. Their position and velocity is affected by the electric field strength, by the collisions with other particles and collisions with the walls. When a primary electron collides with a neutral particle, the collision can be one of the following types:

1. A primary electron elastically collides with a neutral, with no energy lost but a change in the particles velocity occurs.
2. A primary electron collides and ionizes a neutral particle, with energy loss and change into the particles velocity. The neutral atom becomes a single positive charged ion and a secondary electron is released from its orbit.
3. A primary electron collides and excites the neutral particle, with energy loss and change into the particles velocity.
4. A primary electron collides and attached to the neutral particle. The neutral

particle becomes a single negative charged ion.

The electrons movement through the anode is maintained by the electric field between anode and cathode. Once an electron reaches the anode it is absorbed and lost from the plasma discharge. Similar processes occurs in the ion-neutral interactions, but due to the lack of available cross sections data in the literature, in the present work we don't take into account the ion-neutral interactions

The electron collisions are the driving mechanism in plasma processes. In the designed GIS, the electrons and ions produced by the electron collision with the neutral background gas are responsible of the breakdown mechanism. In the present work four types of electron collision cross sections are modeled: Attachment, Elastic, Ionization, and Excitation (vibrational and electronic) as it is shown in Figure 5.8.

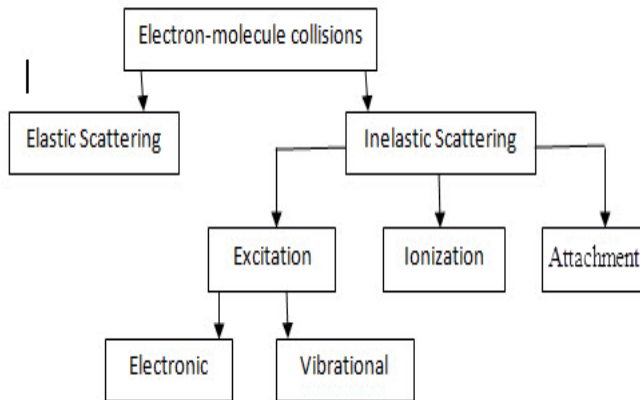


Figure 5.8 – Principle of Electron-molecule collisions inside of the GIS chamber represented by: ionization cross section, elastic cross section, electron attachment cross section and excitation cross section.

A negative voltage is applied to the cathode; the electrons would move to the positive electrode. When the electrons travelling toward the positive electrode, electron elastic

scattering, electron attachment, electron excitation and impact ionization would occur and produce more and more electrons as well as positive and negative ions. All these phenomena will enhance the emission current, lower the working voltage, and improve the sensitivity of the sensor (Figure 5.9).

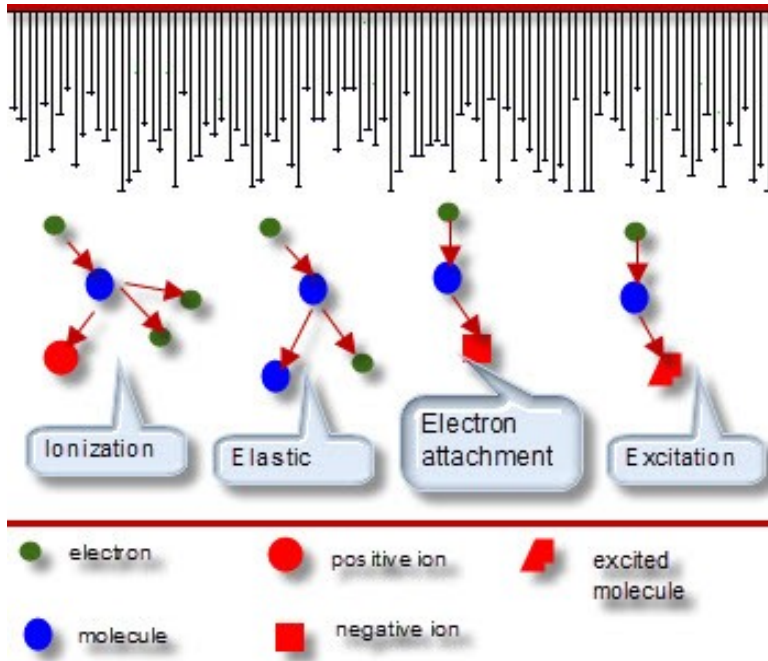


Figure 5.9 –Flow chart of the electron-molecule collisions inside of the gas discharge represented by the elastic and inelastic electron collision.

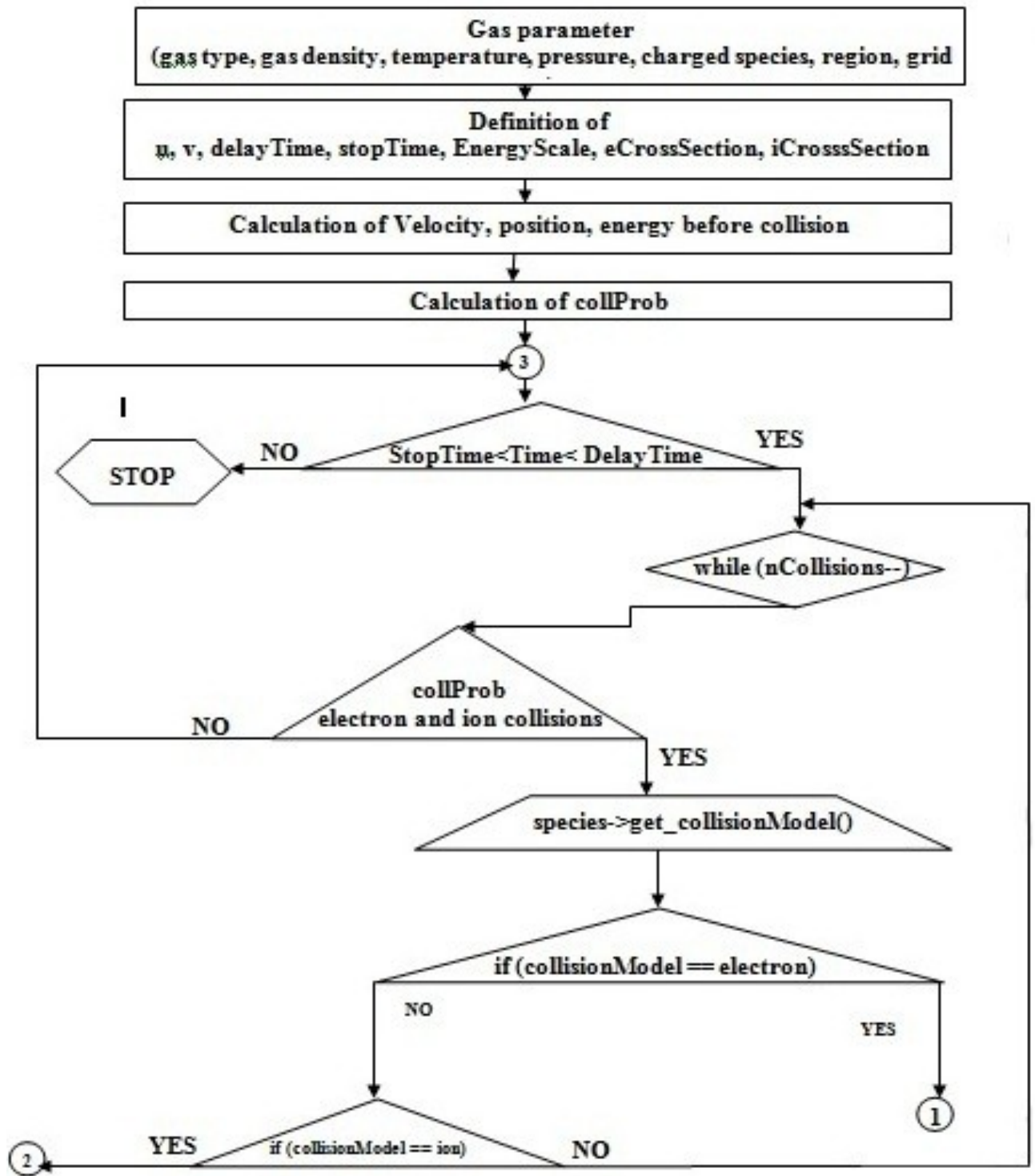
The cross sections values are depended on the particles energy level and each cross section represent a probability that a specific type of collision can occur. The various cross sections are collected from the literature [70-77]. Using interpolation equations we have identified cross section in range of energies. The results were implemented into XOOPIC-GIS.

The XOOPIC MCC class provides collisions by operating on particles. Individual MCC packages were deployed in XOOPIC-GIS to accommodate simple gases like N<sub>2</sub>, O<sub>2</sub>

as well as complex gases like SF<sub>6</sub>, CO<sub>2</sub>, CO, CF<sub>4</sub>, NH<sub>3</sub> and mixture of gases. Based on the specific cross section equations previously computed in MATLAB, the following electron collisions type were diploid in XOOPIC-GIS: elastic, excitation, vibrational, ionization, attachment. The MCC is implemented in two different regions of the XOOPIC-GIS package: advisor and physics.

1. The file **Advisor\mccg.cpp** defines the MCCParams class, which contains the Monte Carlo collision parameters such as gas name, neutral gas pressure and temperature, ion and electron species for ionization, negative ion species for ionization, double ionized species, number of the ions created in ionization event (ionization fraction), minimum and maximum x1, x2 position defining neutral gas region, the delay time before MCC algorithm activates and stop time when the MCC algorithm ends.

2. The file **Physics\mcc.cpp** defines the Monte Carlo collision class describing the physics of the particles collisions (Figure 5.10).



(a)

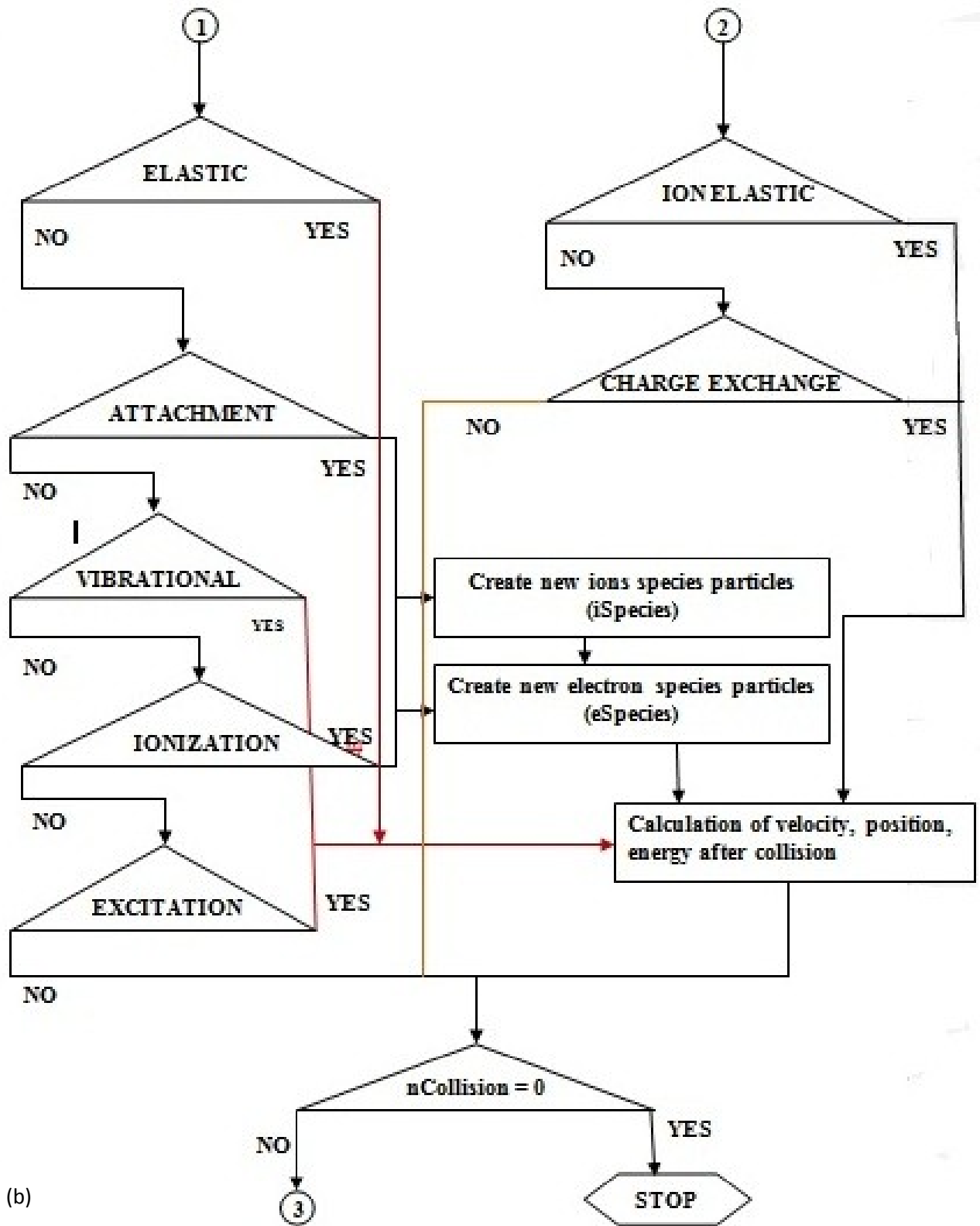


Figure 5.10 XOOPIIC – MCC class flowchart of the implemented MCC technique into the two packages of XOOPIIC-GIS software - advisor and physics.

1. Through the advisor package of the XOOPIIC-GIS, the following gas parameters are read from the input file and sent to the MCC class: gas type, density, temperature, pressure. Also the spatial region that owns the collision model is defined together with the grid associated with this spatial region. The maximum grid coordinates are set also from the input file. Electron and ions species are created in Monte Carlo Collisions and the gas may be confined to a portion of the grid.
2. In the next step the particle's velocity ( $u$ ) and its magnitude ( $v$ ), the `delayTime` and `stopTime` used for simulation time comparison, the electron cross section (`eCrossSection`) and ion cross section (`iCrossSection`), and the `energyScale` variable for both electron and ions species are defined and initialized.
3. The position vector, velocity and simulation time of particle that might undergo collision are saved;
4. In order to check for electron and ion collisions, the electron and ion collision probability is calculated as.
5. Return if simulation time is not within the specified time interval (function terminates)
6. Loop over random selection of particles and see if collision occurs. If  $n$  is the total number of particles in all relevant particle groups then the number of potential collisions is  $n$  times the maximum collision probability ( $n * \text{collProb}$ ).
7. Get the collision type; if electron collision
  - *attachment [defined in section 5.3]*

- *elastic [defined in section 5.3]*
- *excitation [defined in section 5.3]*
- *ionization [defined in section 5.3]*
- *vibrational [defined in section 5.3]*

## 5.3 Electron Collision Cross Sections

A cross section is the effective area in which a certain type of collision can occur. In the electron-atom collision, the cross section is a hypothetical area around the target particle – in this case the atom. When the electrons cross this area, certain interactions will take place, as described below.

### *Attachment Cross sections*



In the electron attachment collision the electron is attached to the neutral atoms and creates a negative ion, losing kinetic energy.

### *Elastic collision cross section*



(where X can be any of the SF<sub>6</sub>, CO<sub>2</sub>, CO, CF<sub>4</sub>, NH<sub>3</sub> gases)

After an elastic collision the electron gets scattered and loses little or none of its kinetic energy. Some of its energy of motion can be transferred to the motion of the particle with which it is colliding even though none of the energy goes into increasing the internal energy of the particle.

***Excitation collision cross section***

The excitation collision occurs when an electron moves from a lower energy state to a higher energy state. The electron loses at least the excitation threshold energy and gets scattered after the collision. The excitation threshold energy is the amount of energy required to excite a neutral atom to the next energy level.



***Ionization collision cross section***

In an ionizing collision the electron ionizes the neutral atoms and creates a secondary electron, losing kinetic energy equal to or greater than the amount of energy required to ionize the neutral atom. This energy is known as the ionization threshold energy.



### *Vibrational excitation cross section*

Vibrational excitation is a mixture of direct excitation and indirect excitation via resonances. The atoms in molecules are in a periodic motion with a frequency known as a vibration frequency. When the molecular vibration absorbs a quantum of energy equal to the vibration frequency, then it says that the molecular vibration is excited.



( $\nu_1$  = the symmetric stretch frequency; for the  $\text{CF}_4$  molecule,  $h\nu_1 = 0.112 \text{ EV}$  [70]).

## **5.4 Applying Cross Sections in XOOPIG-GIS**

In present work, for each tested gas an instance of the corresponding MCC class is created into `xoopic/physivs/mcc.cpp` file. The parameters as grid size, pressure, temperature, and particle species are all read from the input file and passed to the MCC module through advisor module.

Inside of the MCC class, the `MCC::addCrossSections` implements new functions to accommodate the cross sections types as attachment, elastic, excitation, ionization, vibrational.

Starting from the experimental data cross sections available in literature the best fitting equations done in MATLAB are implemented into XOOPIG-GIS MCC package to add the new background gases.

## 5.5 XOOPIC-GIS Input File

The XOOPIC was modified to accommodate our GIS structure. Figure 5.11 shows the XOOPIC-GIS input file diagram. The input file includes the structure of the device and field ionization effect. Parameters that affect the design and the function of the device are included in the input file and they could be varied as simulate the design to reach the optimized values for each parameter.

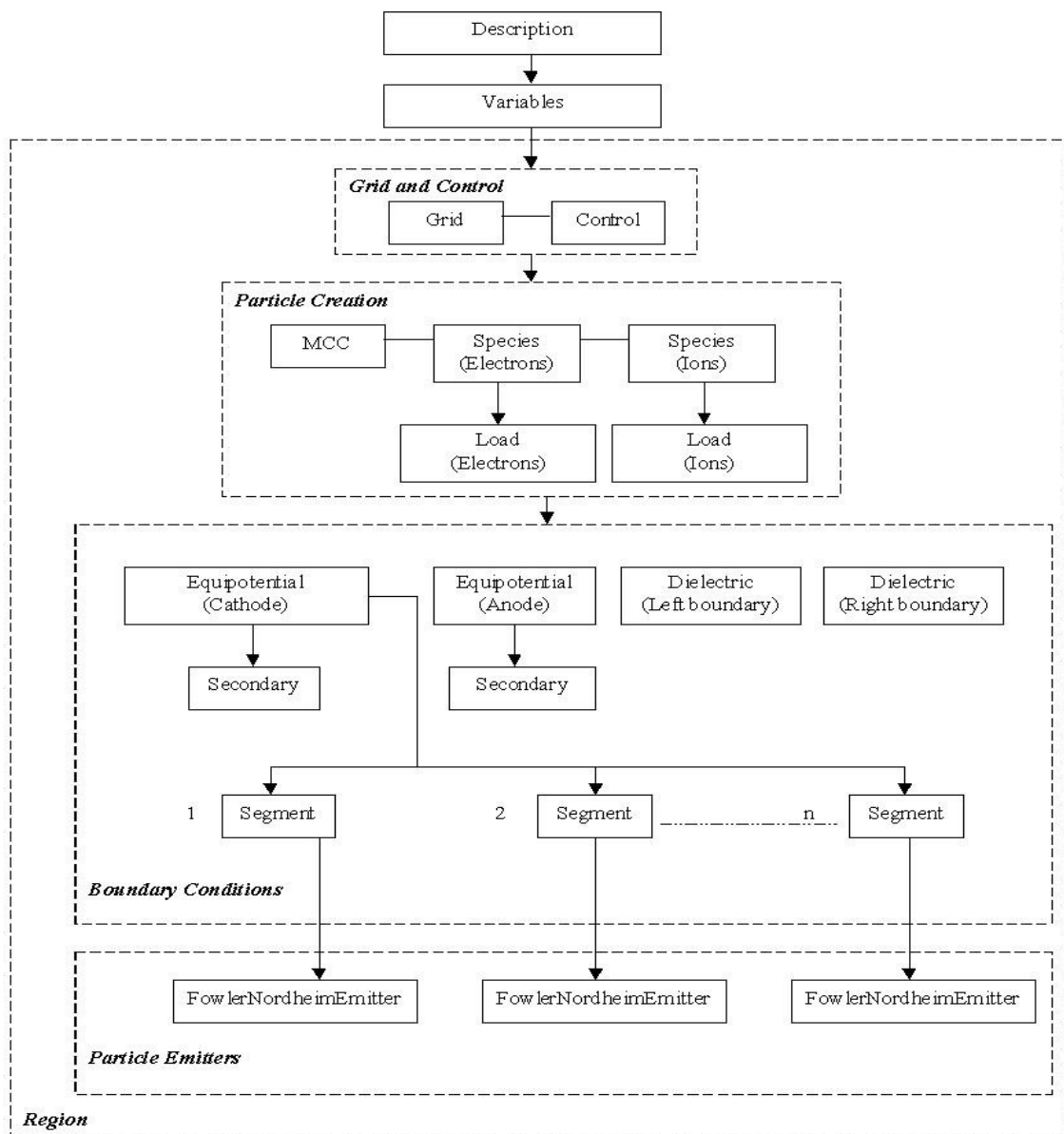


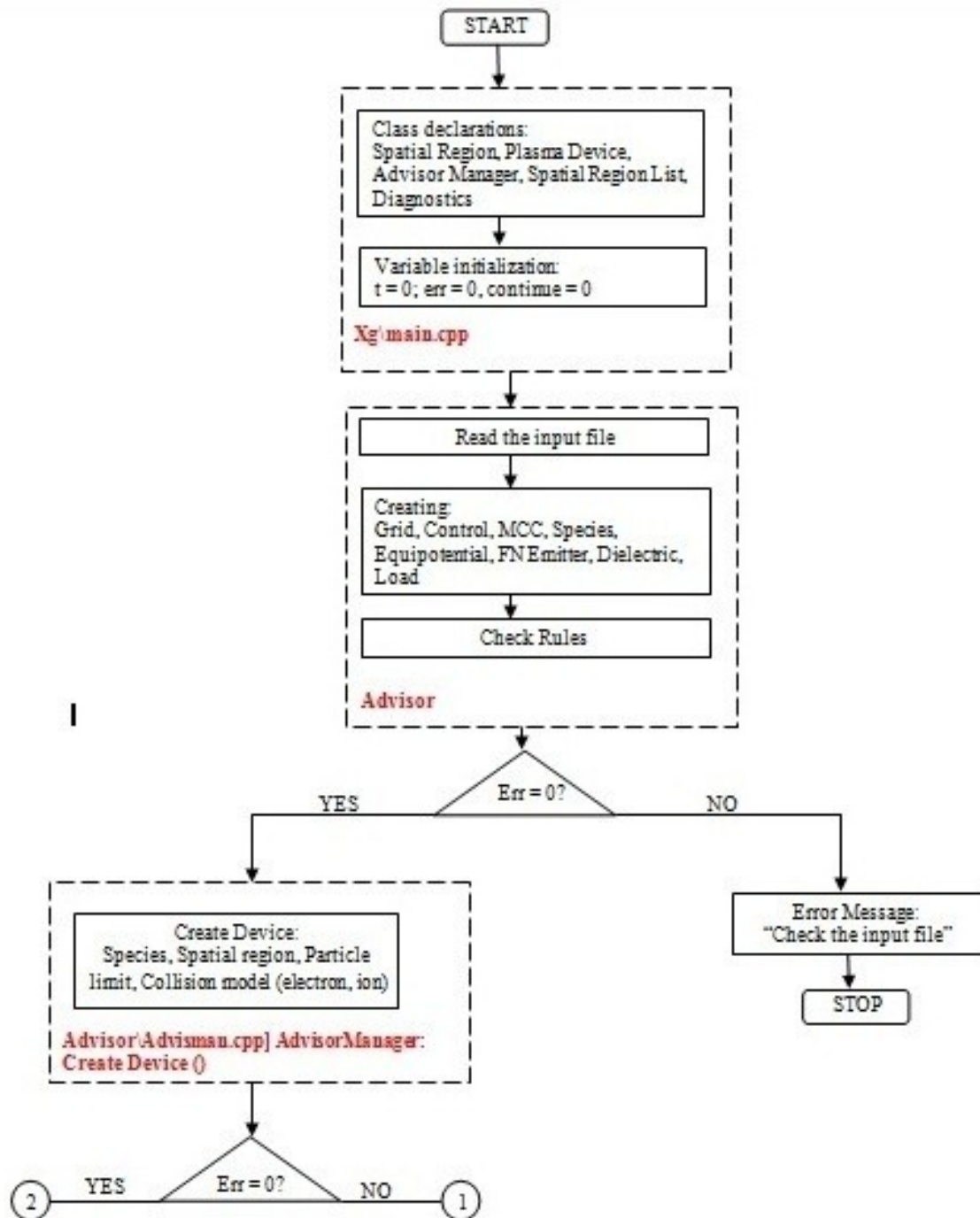
Figure 5.11 XOOPIC-GIS Input File flowcharts – physics and device structure.

Our XOOPIC-GIS input file includes also all physics that happened inside of the device:

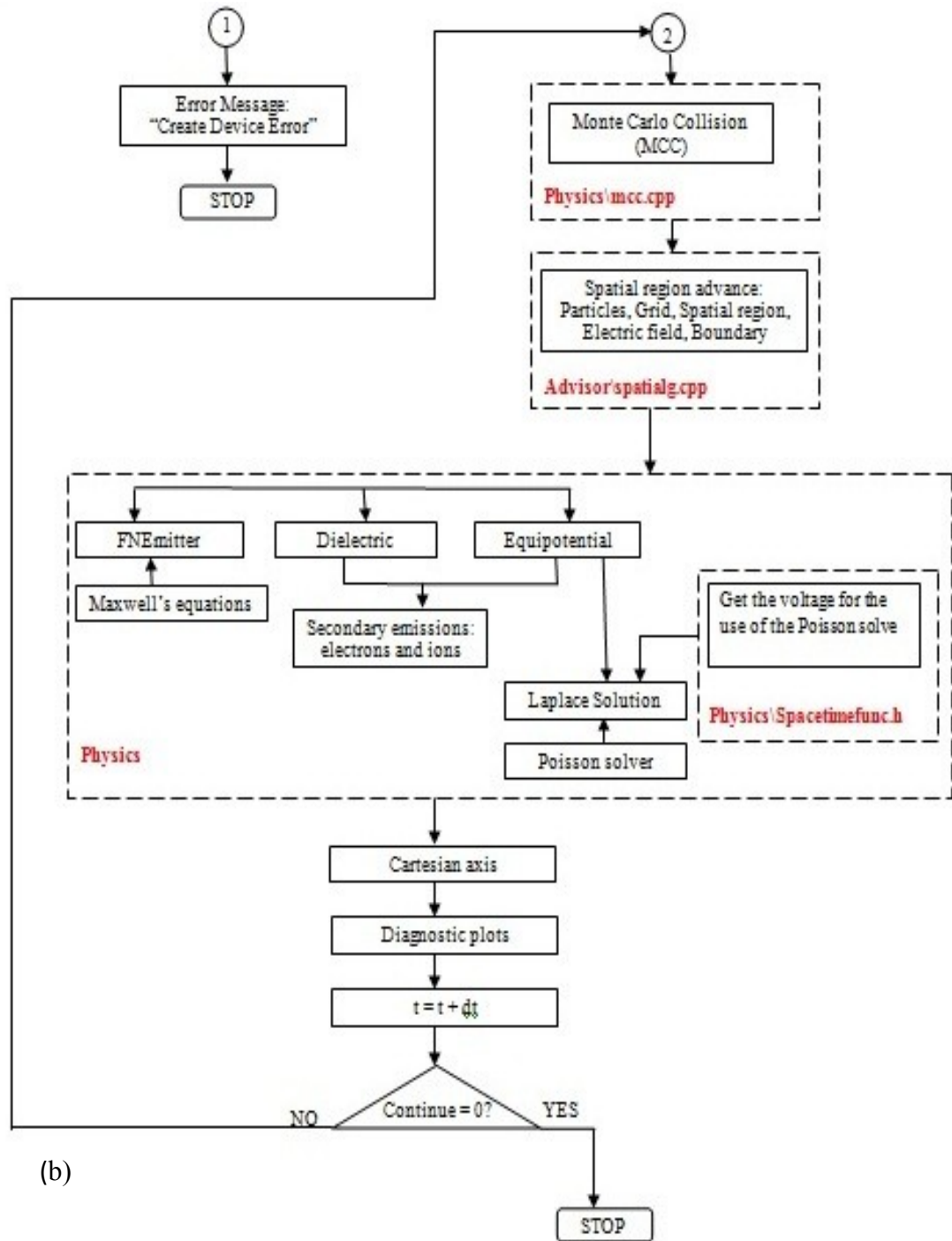
- the gas ionization phenomenon is demonstrated by electron impact ionization;
- atoms are ionized in collision with these electrons, using a Monte Carlo Collision model;
- at the nanowires tips, Fowler Nordheim Emission (FNE) is considered;
- the secondary electrons emissions is taken into account;
- the diagnostics of how much energy they have upon arrival at the far wall, are kept.

As boundaries, the nanowires are equipotential surfaces and the rest of the top boundary is dielectric. The bottom boundary is a perfect conductor -equipotential surface and left and right boundaries are simple dielectric.

## 5.6 The Flow Chart of the XOOPIC-GIS



(a)



(b)

Figure 5.12 XOOPIC GIS Flow Chart.

## 5.7 XOOPIE-GIS Parameters Optimization

Further we have carried the results of the COMSOL studies presented in Chapter 4 to optimize the gas breakdown voltages in our modeled device. We have incorporated the results of COMSOL simulations with XOOPIE-GIS and several different designs were considered in this work as it is presented in the simulation flowchart in Figure 5.14. The breakdown of gases in designed devices with nanowires with rectangular shapes and various concentrations were tested. For the high nanowires concentration, the breakdown voltages increased significantly, probably due to the screen effects between closely packed nanowires. We also tested the design for various device widths (reducing size of the device even further). The results showed that no breakdown will achieve if the width of the device is smaller than 500 microns. This may be due to the fact that the gas concentration will be very small and the flow of the gases throughout the device will be more difficult. In most observations, the intensity of the induced electric field in XOOPIE-GIS is somehow different from those observed in COMSOL as it is shown in Figure 5.13. This difference can be due to the fact that in our XOOPIE-GIS simulation tool, the entire plasma physics reactions are incorporated.

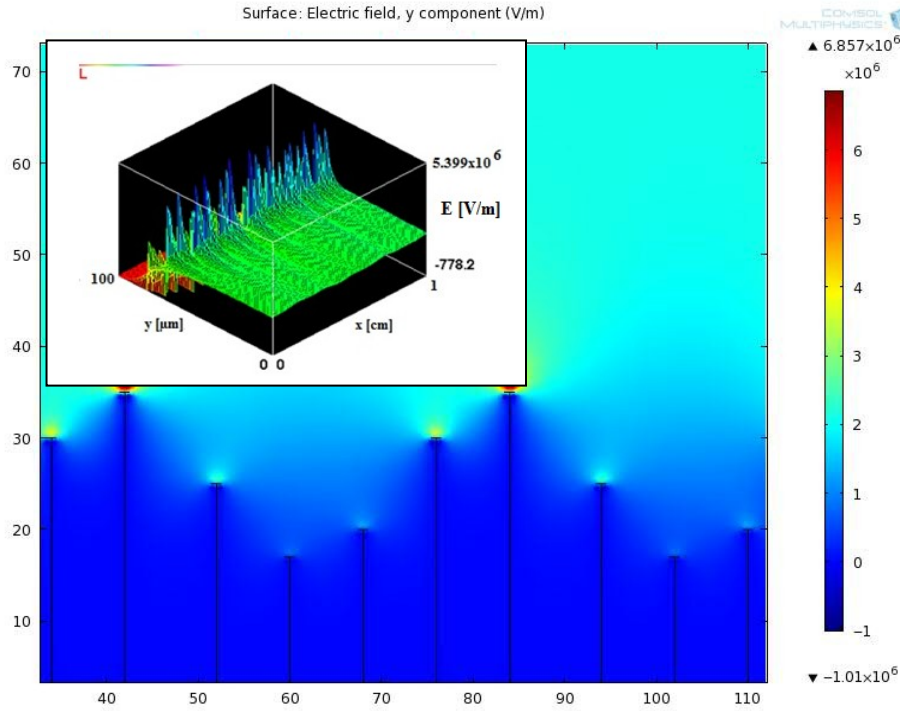


Figure 5.13 The electric field intensity - COMSOL simulation Figure 5.11 XOOPIC-GIS; the inset shows the same electric field intensity from XOOPIC-GIS simulations.

Table 5.1 shows that the devices designed having nanowires with rectangle tip shape have lowest breakdown and avalanche achieved faster than other designs.

Table 5.1 The effect of the nanowire tip shape on breakdown. All other parameters were taken the same.

The measurements are done for Ar gas.

Nanowire's tip shape	Nanowire Width	Distance between Nanowires	Breakdown voltage [V]	Time of breakdown [s]
Rectangle	6.666 $\mu\text{m}$ ,	3.333 $\mu\text{m}$	200	$1.5 \times 10^{-9}$
<b>T</b>	<b>6.666 <math>\mu\text{m}</math>,</b>	<b>3.333 <math>\mu\text{m}</math></b>	<b>200</b>	<b><math>1.7 \times 10^{-9}</math></b>
Triangle	6.666 $\mu\text{m}$	3.333 $\mu\text{m}$	200	$1.68 \times 10^{-9}$

Also, as it is seen from Table 5.2, the distance between the nanowires plays an important role, due to the screening effect of neighboring nanowires. As the distance increases, the

screening is weaker and breakdown can happen at a lower applied voltage.

Table 5.2 The time of breakdown for devices versus the distances between nanowires. All other parameters were taken the same. The measurements are done for Ar gas.

<b>Nanowire's tip shape</b>	<b>Nanowire Width</b>	<b>Distance between Nanowires</b>	<b>Breakdown voltage</b>	<b>Time of breakdown [s]</b>
T	6.666 $\mu\text{m}$ ,	1.333 $\mu\text{m}$	200V	2.1x10 <sup>-9</sup>
T	6.666 $\mu\text{m}$ ,	3.333 $\mu\text{m}$	200V	1.7x10 <sup>-9</sup>
<b>T</b>	<b>6.666 <math>\mu\text{m}</math></b>	<b>8.333 <math>\mu\text{m}</math></b>	<b>200V</b>	<b>5.6x10<sup>-10</sup></b>

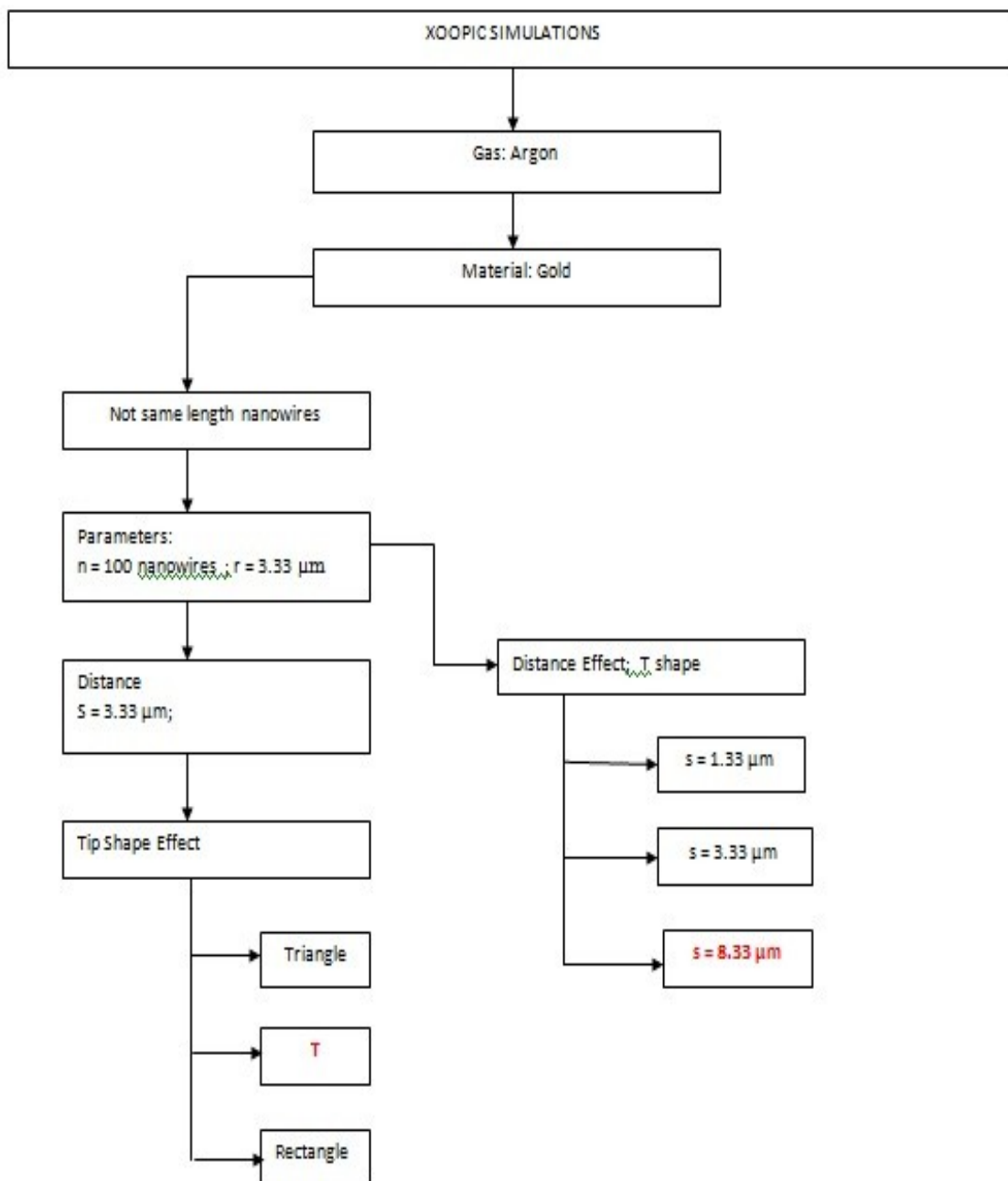


Figure 5.14 XOOPIE simulations flowchart.

## 5.8 Conclusions

In this chapter we have introduced a software tool called XOOPIC-GIS. We have discussed the application of the tool and how the measurements are implemented. The modeling of GIS by MCC technique is presented in details. Various collisions between the electrons and neutral molecules which are the main phenomena modeled by MCC are implemented in our developed software tool. Complete flow charts of the MCC XOOPIC-GIS package are presented and explained. The device structure, field ionization effect as well the parameters which affects the device functionality are introduced into the input file of the XOOPIC-GIS.

# Chapter 6

## XOOPIC-GIS Simulation Results

In this chapter, results of the simulated modeled gas sensor using the developed XOOPIC-GIS tool are presented.

As it was discussed before the device was modeled as two parallel plates with nanowires sandwiched between them. A gas flows inside the device with various pressures. Under various conditions (described in the following sections) the minimum voltage that led to formation of an avalanche, was recorded as the breakdown voltage,  $V_B$ .

As in practice an associated external circuit connected to the device, we have added a series resistance connected to one of the electrodes.

Due to the applied voltage,  $V$ , between the two electrodes and induced electric field inside the device, negative charges accumulate on the anode and positive charges on the cathode electrode (Figure 6.1). The current,  $I$ , corresponding to these charges will cause a potential drop,  $V_R$ , across the resistance  $R$ .

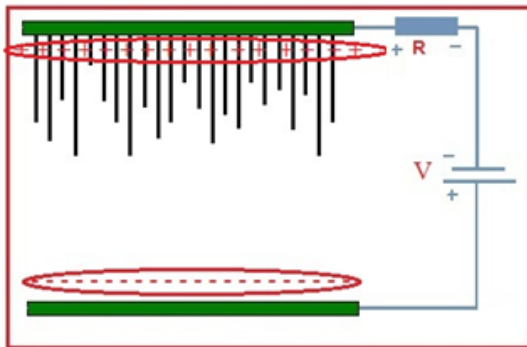


Figure 6.1 The GIS schematic device with series resistance  $R$  showing the charge accumulation at the anode.

At the beginning of the ionization process among the gas molecules, this potential drop is much smaller than the applied voltage  $V$ . As the process continues, more and more charges are building up on the electrodes, the voltage drop across the resistance  $R$  becomes significantly larger than the applied voltage and the total voltage across the plates,  $V - V_R$ , increases until the breakdown is reached.

## 6.1 General Description of Gas Ionization in GIS

Figure 6.2 shows the 2-D model containing radiation-induced electrons residing in the space between the nanowires and the counter electrode at  $P = 1\text{Torr}$ , before the external voltage was applied ( $t = 0$ ).

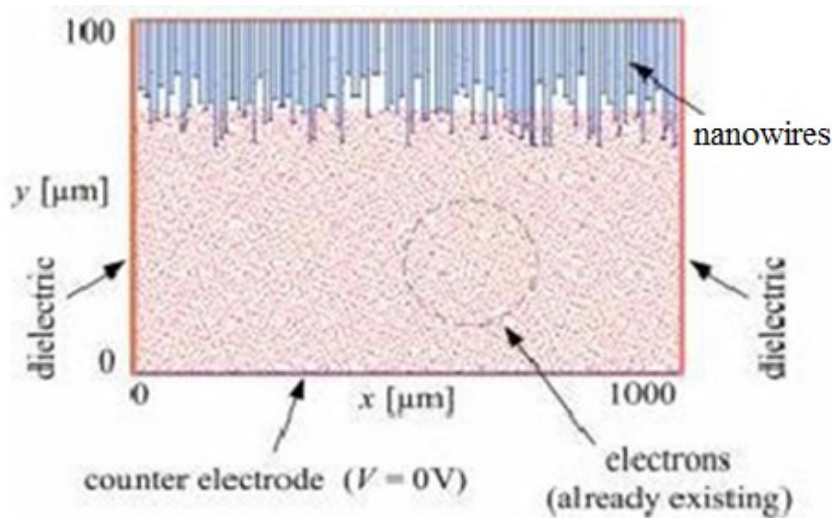


Figure 6.2 The 2 – D model for the device showing the radiation- generated electrons (or ions) before a bias voltage was applied.

When a voltage is applied between the two plates, due to the generated electric field between the two plates, the electrons present in the gas (due to the thermal and radiation energies) are accelerated towards the anode making collisions with atoms of the background gas. The electric field enhanced proportionally with aspect ratio of the nanowires causes the carriers to travel much faster inside the device. Figure 6.3 shows the electric field intensity inside the sensor for an applied external voltage of -150V.

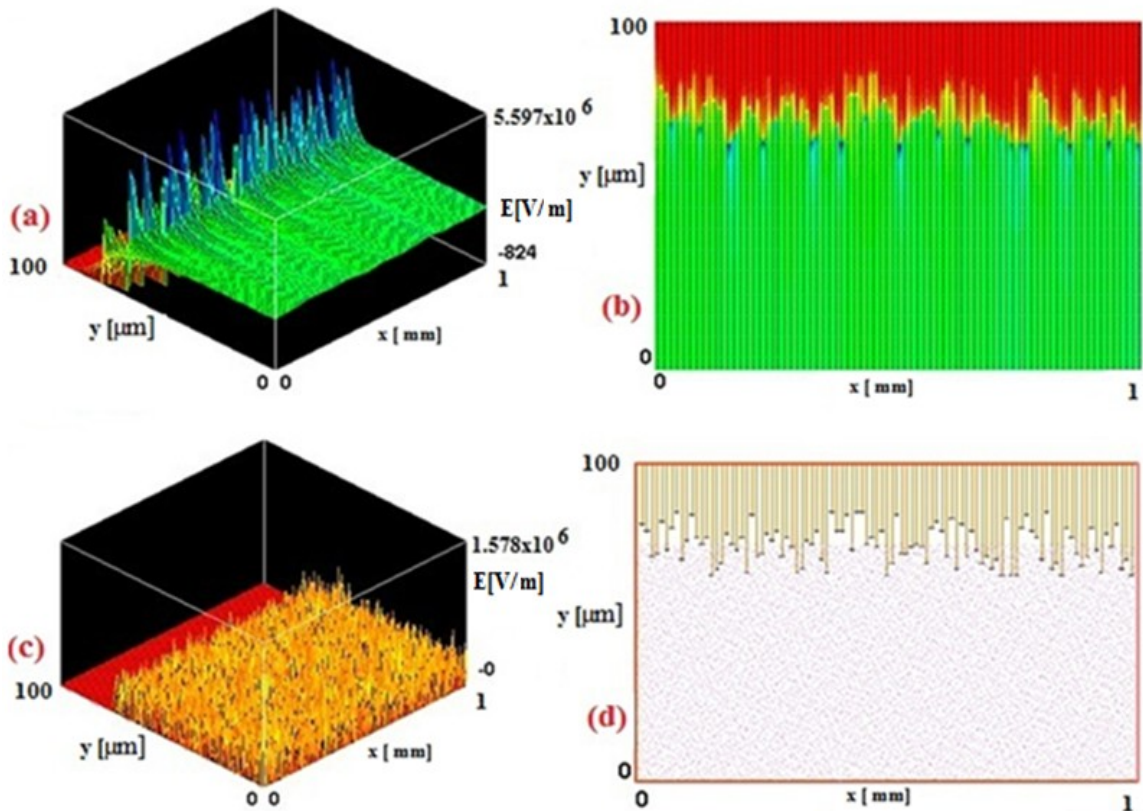


Figure 6.3 The electric field intensity between the two electrodes for the external applied field of  $V = -150\text{V}$ ;  $x$  axes represents the chamber device length, on  $y$  axes is represented the gap distance between the two plates; a) 3D view with electric field intensity shown on  $Z$  axes; b) 3-D view with a section cut along the  $z$  axes, c) 3D view of charge distribution shown on  $Z$  axes; d) 3-D view of charge distribution with a section cut along the  $z$  axes.

As it is clearly seen from the figure the field due to the aspect ratio of the nanowires is enhanced greatly compared to the applied field at the bottom of the cell on cathode electrode side. The enhanced electric field is responsible for the fast gas ionization, which in turn lowers the breakdown voltage by several hundred volts compared to parallel plate devices. The mathematical axes  $x$  and  $y$  corresponds to the 1mm chamber width and to the gap distance of 100  $\mu\text{m}$  respectively. The electric field intensity reaches a maximum of  $5.6 \times 10^{06}$  V/m at the tip of the nanowires. Figure 6.3 c) and Figure 6.3 d) show that there is no charge distribution between the nanowires, as a result the electric field (represented by the red zone on the graphs) is zero in these regions.

The total field inside the device is equal to the external applied field plus the local field induced at the tip of the nanowires. As it was shown in Chapter 4, the induced local electric field depends on the sharpness, aspect ratio and the separation of the nanowires.

When collisions in the gas occur, more negative and positive charges are formed, moving toward the oppositely charged electrodes. Since the electrons have much smaller mass and higher mobility than those of ions, they drift faster than ions.

The generated electrons may interact further with ions present inside the chamber causing to emit other electrons, called secondary electrons. The carriers are built up with time on the two opposite plates and eventually an avalanche occurs, causing the breakdown of the gases.

Figure 6.4 shows the plot of the electrons and ions avalanches, for Ar gas at  $P = 1\text{Torr}$  and  $P = 0.05\text{Torr}$ , when a high population of charges is reached. The applied external voltage was considered at -155V and -180V for the above pressures respectively.

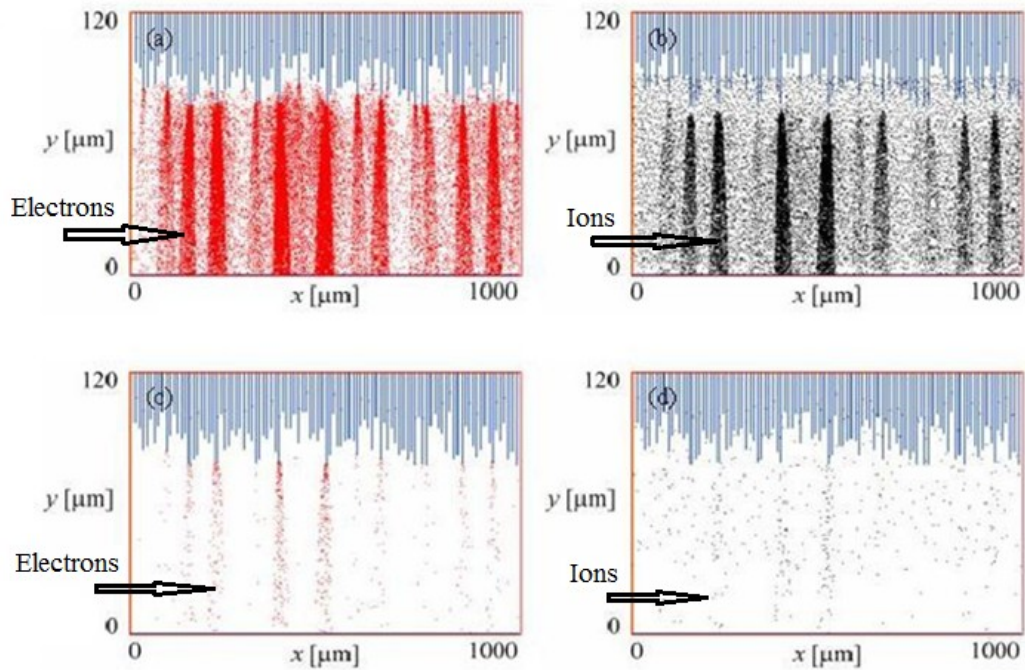


Figure 6.4. The plot of electrons and argon ions avalanches when the charge concentration at the first avalanche become maximum a) electrons and b) ions at  $P = 1$  Torr,  $V = -155$  V, c) electrons and d) ions at  $P = 0.05$  Torr,  $V = -180$  V

Figure 6.5 shows the evolution of total number of carriers with time for Ar gas at  $P = 1$  Torr. The higher total number of electrons compared to ions shows that field due to generated electrons contribute to the formation of an avalanche.

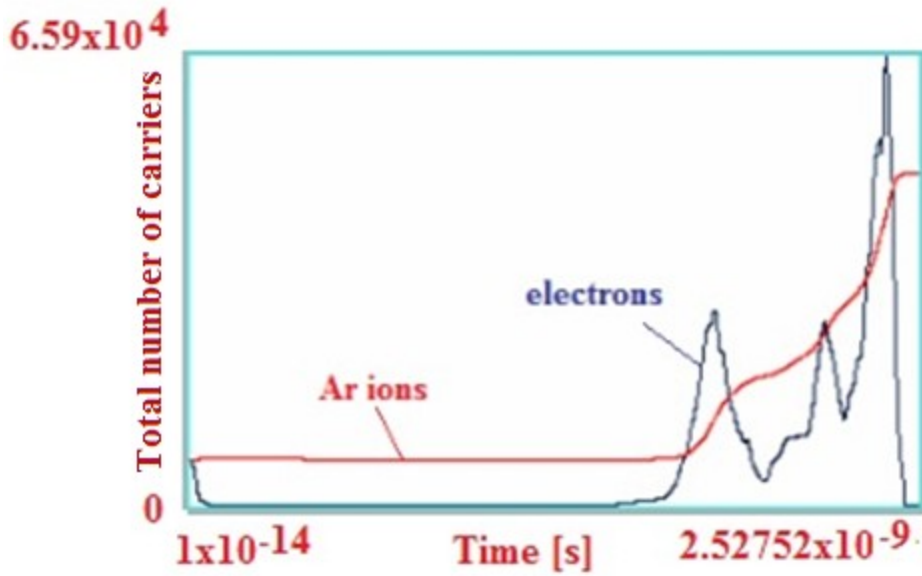


Figure 6.5 The evolution of the total number of carriers in argon for  $P=1$  Torr. (both axes are logarithmic scaled)

Once the total number of carriers builds up inside the device with respect to time an avalanche of electrons will happen. As a result, the constant current suddenly falls to zero and goes substantially negative, indicating the breakdown of the gas. Figure 6.6 shows the  $I-t$  characteristic of the device. It shows the breakdown of Ar gas. The breakdown voltage in this case was,  $V_B = -158$  V.

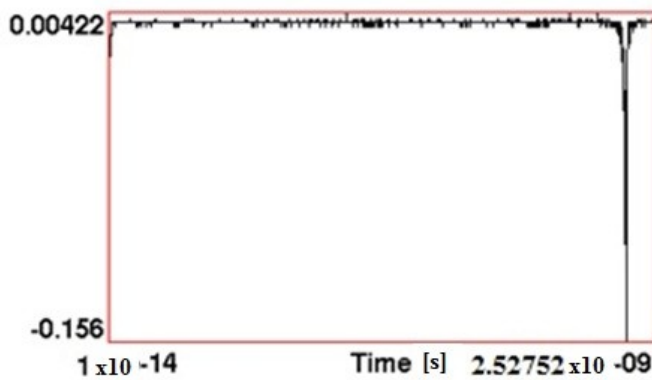


Figure 6.6 The  $I-t$  characteristics showing the breakdown of Argon Gas at pressure  $P = 1$  Torr.

## 6.2 Verification of the Simulation Results

In order to verify the accuracy of our model and the simulation tool, we first designed in the input file of the developed XOOPIE-GIS tool and simulated a device similar to one which was fabricated in our laboratories. In this design, we have considered grown gold nanowires on one of the electrodes. The nanowires thickness was considered around 300nm, with lengths varying between 15 $\mu$ m to 35 $\mu$ m, and separated by 300nm in the direction of x. The y direction is represented by 100  $\mu$ m gap distance between the two parallel plate's electrodes.

The circuit elements as a series resistance,  $R$ , is incorporated with our device, dc voltages and the contribution of field emission from AuNW tips are also considered in this process. The breakdown voltages obtained from our simulation results were in very good agreement with the experimental results [24].

Figure 6.7 shows the simulated  $V_b$ - $P$  curves obtained for Ar gas in the pressure range of  $0.02 \leq P \leq 1$  Torr, at room temperature, with AuNWs as cathode [25]. The minimum breakdown voltage,  $V_b$  was recorded for several gas pressures.

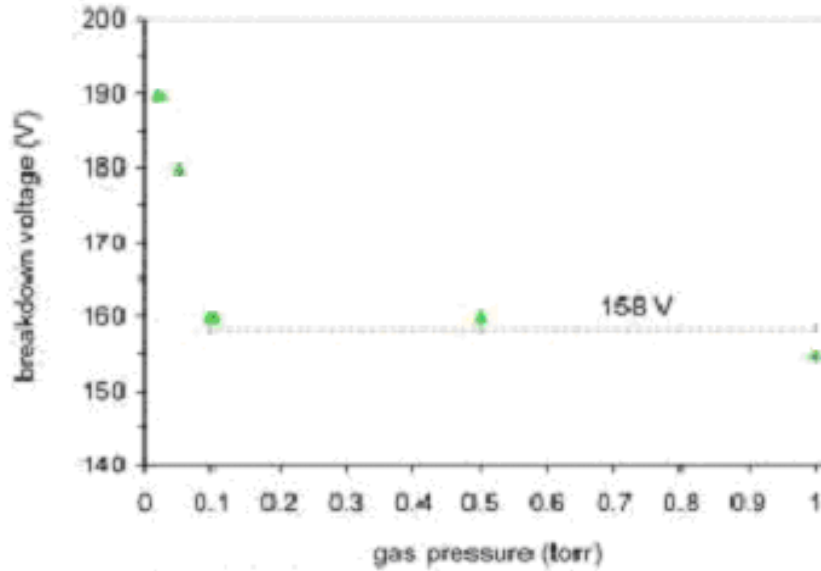


Figure 6.7 Simulated V-P curves for AuNWs grown at cathode side [25].

As the figure shows the  $V_B$  remains constant for gas pressure above 0.1 Torr. However, as the pressure goes down the gas molecule concentration decreases causing the breakdown happens at much higher voltages.

Figure 6.8 shows the  $V_B$  for Ar gas obtained experimentally for the same range of pressures [25]. Comparing figures 6.7 and 6.8 shows that the simulated and the experimental results are in good agreement.

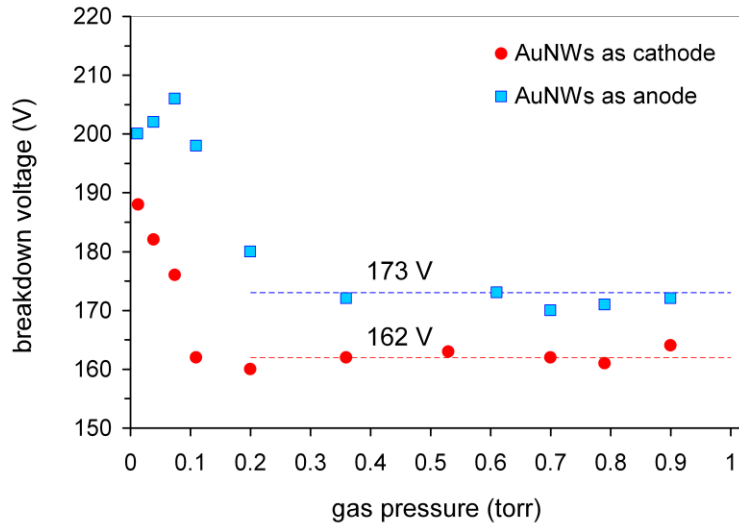


Figure 6.8 Experimental  $V$ - $P$  curves for AuNWs grown at cathode and at anode [25].

We have further verified our results for a device fabricated with silver nanowires. A device was modeled with the same description reported by [26]; the  $V_B$  obtained by our simulation technique was in good agreement with theirs under the same conditions. Figures 6.9 and 6.10 show the  $V_B$  - $P$  characteristics of Ar gas obtained experimentally [26], and by our works respectively.

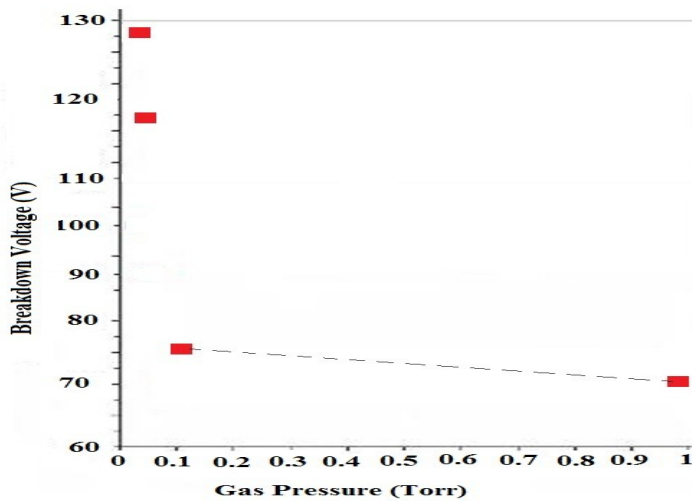


Figure 6.9 Experimental  $V$ - $P$  curve for Ar NWs grown at cathode [26].

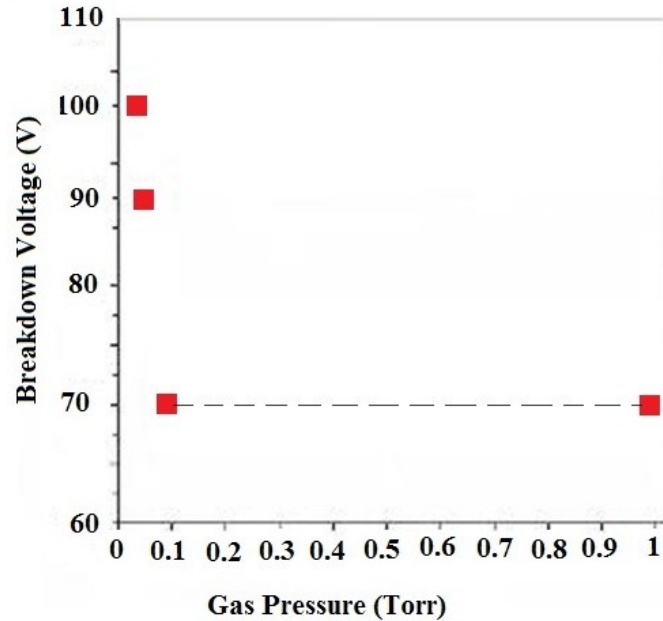


Figure 6.10 Simulated V-P curve for Ar NWs grown at cathode [26].

## 6.3 Effects of Various Parameters on $V_B$

Based on the field ionization, physics, and mathematical model described in Chapters 1 and 2 the following parameters will influence the device structure and functionality:

- type of gases like Ar, He, N<sub>2</sub>, Ne, greenhouse gases, mixture of gases;
- different type of nanowires like Gold, Silver, Zinc Oxide;
- the aspect ratio  $\beta$  ( the radius to length ratio of the NW);
- the shape of nanowires tips;
- distance between the nanowires;
- the gap between the electrodes;
- the resistance R;

- the distance between nanowires and the top electrode;
- Non linearity of the electric field around the nanowires.

In the following sections we report our studies on the effect of above parameters on the breakdown voltages of gases. In these investigations to be comparable we have considered a device with gold nanowires, and Ar at  $P = 1\text{Torr}$  as the background gas in all cases.

### 6.3.1 Effect of Series Resistance on $V_B$

Table 6.1 The effect of series resistance on  $V_B$

Parameter	Breakdown Voltage $V_B$ [V]	Time $t$ [s]
R = 4 Ohm (Beta = 500, X = 1000 $\mu\text{m}$ , Y = 100 $\mu\text{m}$ )	-210	$1.02 \times 10^{-09}$
R = 6 Ohm (Beta = 500, X = 1000 $\mu\text{m}$ , Y = 100 $\mu\text{m}$ )	-190	$1 \times 10^{-09}$
R = 8 Ohm (Beta = 500, X = 1000 $\mu\text{m}$ , Y = 100 $\mu\text{m}$ )	-170	$1.1 \times 10^{-09}$
R = 10 Ohm (Beta = 500, X = 1000 $\mu\text{m}$ , Y = 100 $\mu\text{m}$ )	-155	$1 \times 10^{-09}$
R = 100 Ohm (Beta = 500, X = 1000 $\mu\text{m}$ , Y = 100 $\mu\text{m}$ )	-155	$5.1 \times 10^{-10}$

Keeping the same values for the parameters like field enhancement factor,  $\beta$ , the gap distance, Y, and the chamber width, X, simulations were done for different values of the series resistance, R. From the simulation results tabulated in Table 6.1 it can be seen that the optimum value of the series resistance R is 10 Ohm for which the breakdown voltage has the lowest value of -155V.

In order to study further the behavior of  $V_B$  versus resistance R, simulations were done for a high value of R (100 Ohm) and the results have been confirmed our conclusion: as

high is the R as lower  $V_B$  will be. But in reality there are circuit limitations, so we can consider that 10 Ohm is a reasonable value as the series resistance to represent the associated microelectronic circuits.

Figure 6.11 shows a typical simulation result of generated current versus time between the two parallel plate for Ar at P= 1Torr, Beta = 500, Y = 100 $\mu\text{m}$ , X = 1000 $\mu\text{m}$  and a) R = 4 Ohm, b) R = 6 Ohm, c) R = 8 Ohm, d) R = 10 Ohm.

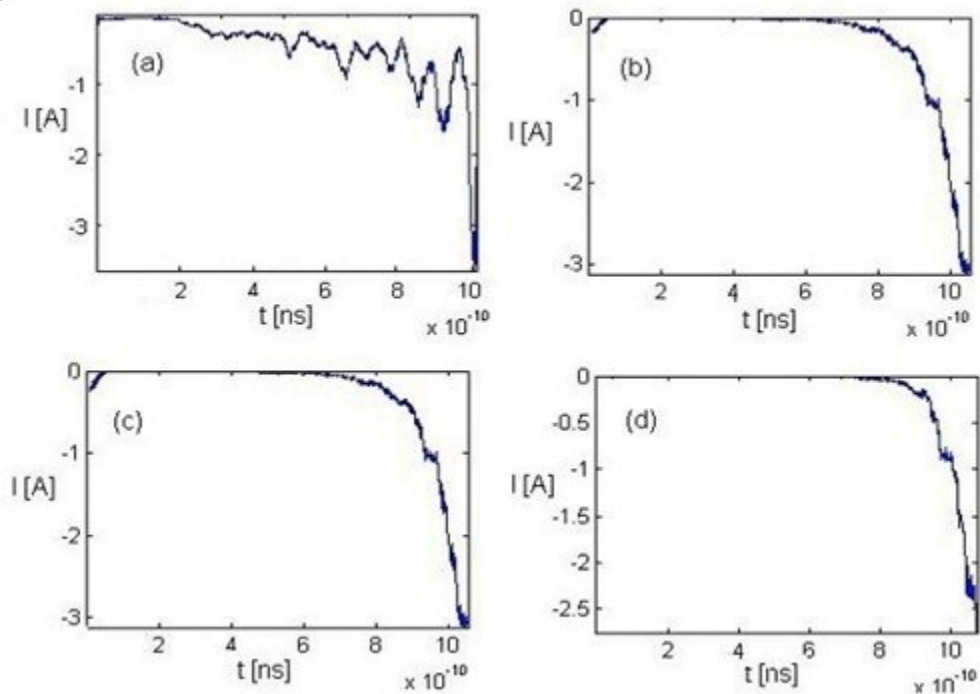


Figure 6.11 Generated current versus time for Ar at P= 1 Torr, Beta = 500, Y = 100 $\mu\text{m}$ , X = 1000  $\mu\text{m}$  and a) R = 4 Ohm, b) R = 6 Ohm, c) R = 8 Ohm, d) R = 10 Ohm

## 6.3.2 Effect of Aspect Ratio on $V_B$

As previously presented in Section 3.1, the field enhancement factor,  $\beta$ , can be approximated by the aspect ratio  $l/r$ . In this step, we kept the values of the series resistance  $R$ , gap distance,  $Y$ , and the chamber width  $X$  constant as in previous step. The aspect ratio represented by the field enhancement factor,  $\beta$ , is varied from 200 to 500. Several simulations were done until the breakdown happened at the same time,  $t \sim 1 \times 10^{-9}$  s, for each set of parameters the result were recorded in Table 6.2. The minimum value of the breakdown voltage is reached for a field enhancement factor  $\beta$  of 500, which in practice is equivalent to a high aspect ratio of the nanowires.

Table 6.2 The effect of the enhancement factor on  $V_B$

Parameter	Breakdown Voltage $V_B$ [V]	Time $t$ [s]
Beta = 200 (R=10 Ohm, X = 1cm, Y = 100 $\mu$ m)	-380	$1.2 \times 10^{-9}$
Beta = 300(R=10 Ohm, X = 1cm, Y = 100 $\mu$ m)	-260	$1.2 \times 10^{-9}$
Beta = 500(R=10 Ohm, X = 1cm, Y = 100 $\mu$ m)	-155	$1 \times 10^{-9}$

The simulations show that as  $\beta$  increases the breakdown voltage will decrease. However, the larger the  $\beta$  means larger aspect ratio. There are always limitations in practice to develop nanowires with a very high aspect ratio. We recommend that  $\beta = 500$  is a very reasonable to be considered in practice.

### 6.3.3 Effect of the Chamber Width on $V_B$

We are defining the “X” parameter as the width of the parallel plate electrodes, or chamber width. Keeping the same number of the nanowires ( $n = 100$ ) at the cathode side as in the previous simulations, and keeping other parameters the same as the last step simulations were done for different values of  $X$  and the breakdown voltage recorded. The optimum device configuration which leads to the minimum  $V_B$  has the width of the parallel plates,  $X$ , of  $1000 \mu\text{m}$ .

Table 6.3 The effect of the chamber widths on  $V_B$

Parameter	Breakdown Voltage $V_B$ [V]	Time $t$ [s]
$X = 600 \mu\text{m}$ (R=10 Ohm, Beta = 500, Y = $100 \mu\text{m}$ )	-210	$1.2 \times 10^{-09}$
$X = 900 \mu\text{m}$ (R=10 Ohm, Beta = 500, Y = $100 \mu\text{m}$ )	-170	$1.1 \times 10^{-09}$
$X = 1000 \mu\text{m}$ (R=10 Ohm, Beta = 500, Y = $100 \mu\text{m}$ )	-155	$1 \times 10^{-09}$

We should emphasize that we are designing a miniaturized gas sensor however, as mentioned before there are limitations in practice. Although, the narrower electrodes are more desirable in our design but the our simulations show that for the devices with very narrow width (smaller volume) the breakdown voltages is higher compare to the wider devices. This could be due to the low amount of gas available in the sensor. Consequently, we recommend a minimum of 1 mm width in the design of the GIS.

### 6.3.4 Effect of the Gap Distance on $V_B$

The gap distance between the two electrodes is defined by “Y” parameter. Simulations were done keeping all parameters with the same values as in previous step, except the gap distance. From the simulations results presented in Table 6.4 the conclusion is that the value of breakdown voltage increases as the gap reduces.

Again for the practical purposes, we recommend a gap with around 100 micron for the designed device. The proposed gap will be enough to facilitate the flow of the gases through the sensors, particularly when the device is tuned to detect gases with larger molecules.

Table 6.4 The effect of the gap distance on  $V_B$

Parameter	Breakdown Voltage $V_B$ [V]	Time t [s]
Y= 80 $\mu\text{m}$ (R=10 Ohm, Beta = 500, X = 1000 $\mu\text{m}$ )	-130	$1.1 \times 10^{-09}$
Y = 100 $\mu\text{m}$ (R=10 Ohm, Beta = 500, X = 1000 $\mu\text{m}$ )	-155	$1 \times 10^{-09}$
Y=120 $\mu\text{m}$ (R=10 Ohm, Beta = 500, X = 1000 $\mu\text{m}$ )	-200	$1.1 \times 10^{-09}$

### 6.3.5 Effect of Work Function differences on $V_B$

In this step the effect of different nanowire materials was studied. The simulations were done for argon gas at pressure  $P = 1$  Torr with the following parameters, R=10 Ohm, Beta = 500, X = 1000 $\mu\text{m}$  and Y = 100  $\mu\text{m}$ . The device was tested for Au, Ag, and

ZnO nanowires. The simulation results shown in Table 6.5 illustrates that the minimum breakdown voltage is reached for the sensor with ZnO nanowires. This could explained by the fact that the ZnO has a smaller work function,  $\phi$  compare to other nanowires ( $\phi_{\text{ZnO}} = 4.35$ ,  $\phi_{\text{Ag}} = 4.8$ ,  $\phi_{\text{Au}} = 5.1$ ). We should add that ZnO is semiconductor material and in this work we have considered highly doped material (high conductive nanowires).

Table 6.5 The effect of different nanowires on  $V_B$

Parameter ( $Y = 100 \mu\text{m}$ , $R=10 \text{ Ohm}$ , $\text{Beta} = 500$ , $X = 1000 \mu\text{m}$ )	Breakdown Voltage $V_B$ [V]	NWs Work Function	Time t [s]
Au NWs	-135	5.1	$2.1 \times 10^{-09}$
Ag NWs	-120	4.8	$2.1 \times 10^{-09}$
ZnO NWs	-93	4.35	$2.1 \times 10^{-09}$

Figure 6.12 shows the  $I-t$  curves for the simulated device having different nanowires material.

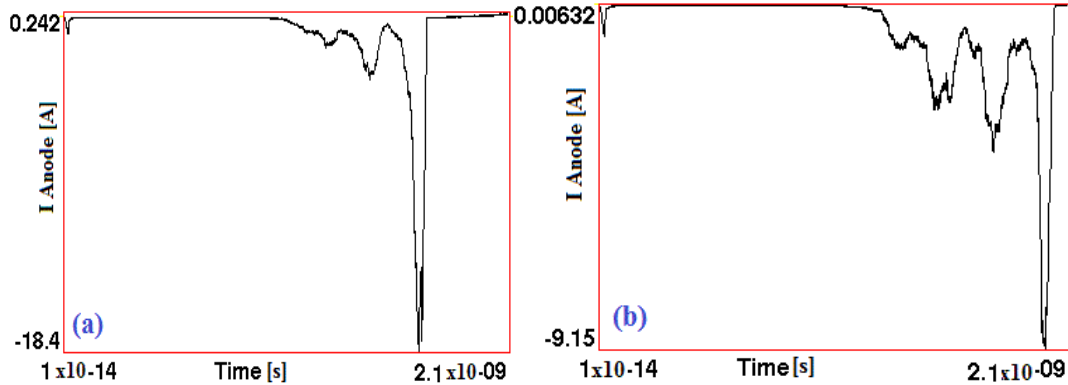


Figure 6.12 shows a typical simulation result of generated current versus time between the two parallel plates for the device having a) Ar NWs; b) ZnO NWs.

## 6.4 Detection of Breakdown Voltages for Simple Gases

In this step simulations are done in order to detect single element gases. The device parameters are kept the same values as in previous simulations. The gap distance between the two electrodes is 100 $\mu$ m, the length of the nanowires grown at the cathode considered between 15 $\mu$ m and 35 $\mu$ m, and the applied pressure was taken as P=1 Torr. With this configuration the simulations were done Ar, He, and Ne gases. Table 6.6 illustrates the fact that each gas has a unique breakdown voltage.

Table 6.6 Simulation results of breakdown voltages for several gases in the modeled GIS device.

Gas	NWs material	Vapp [V]	Time [s]
Ar	Au	-150	1.88 x10 <sup>-9</sup>
Ar	Au	-165	1.42 x10 <sup>-9</sup>
Ar	Au	-170	1.04 x10 <sup>-9</sup>
Ar	Au	-160	1.63 x10 <sup>-9</sup>
He	Au	-120	7.2 x10 <sup>-10</sup>
He	Au	-200	5.9 x10 <sup>-10</sup>
Ne	Au	-270	6.53 x10 <sup>-10</sup>
Ne	Au	-200	8.04 x10 <sup>-10</sup>
Ne	Au	-190	1.6x10 <sup>-09</sup>
Ne	Au	-185	1.27 x10 <sup>-9</sup>
Ne	Au	-182	1.28 x10 <sup>-9</sup>
O <sub>2</sub>	Au	-200	2.38 x10 <sup>-9</sup>
N <sub>2</sub>	Au	-100	1.95x10 <sup>-9</sup>
N <sub>2</sub>	Au	-200	8.8x10 <sup>-10</sup>
N <sub>2</sub>	Au	-175	1.32x10 <sup>-9</sup>

Figure 6.13 shows the simulation results of current evolution with respect to time. The breakdowns are clearly seen for He and Ne gases. One can note that for the same value of applied voltage of  $-200\text{V}$ , the breakdown of He is achieved much faster than the one for Ne indicating that the  $V_B$  for He is smaller than that for Ne. The same trend should be considered in all cases as it is very difficult to adjust the applied voltages to achieve  $V_B$  at the same time for all gases.

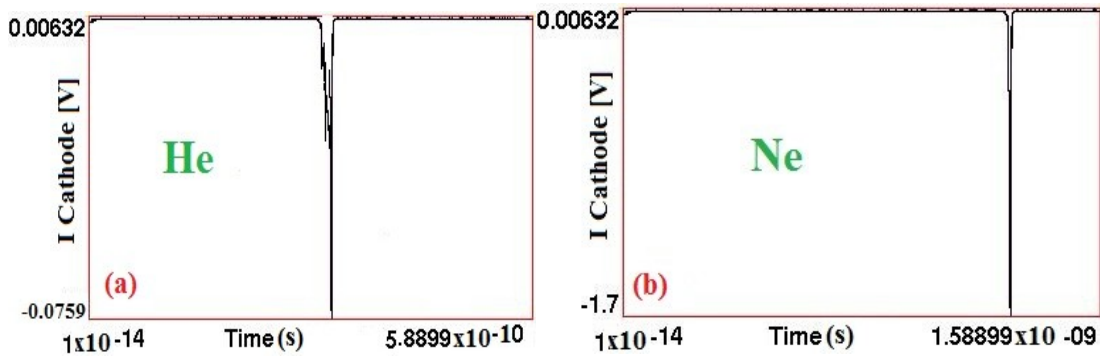


Figure 6.13 Simulation result of generated cathode current versus time for the device having as background gas a) He,  $V_B = -200\text{V}$  ; b) Ne,  $V_B = -190\text{ V}$ .

## 6.5 Detection of Breakdown Voltages for Greenhouse Gases

Using our XOOPIC-GIS simulation tool, we simulated the breakdowns of  $\text{CF}_4$ ,  $\text{SF}_6$ ,  $\text{CO}$  and  $\text{CO}_2$  gases. Quantitative knowledge of electron-neutrals interactions is essential to model the electrical gas discharge. In these studies again based on the electron collision data available in the literature, we have integrated elastic, excitation,

ionization, vibrational and electron attachments cross sections into our simulation package. We have also considered the device made of gold, silver, and ZnO. With these structures, simulations were done in order to detect the breakdown voltage for several greenhouse gases. The gas pressure was considered as 1 Torr, series resistance R of 10 Ohm and gap between the electrodes 100 $\mu$ m, and  $\beta = 500$ . Figure 6.13 shows the time evolution of the CF<sub>4</sub> charged particle inside the GIS. Although the numbers of ions are increasing as well, the gas breakdown is due to the electrons, as the breakdown occurs when the electron concentration falls down suddenly.

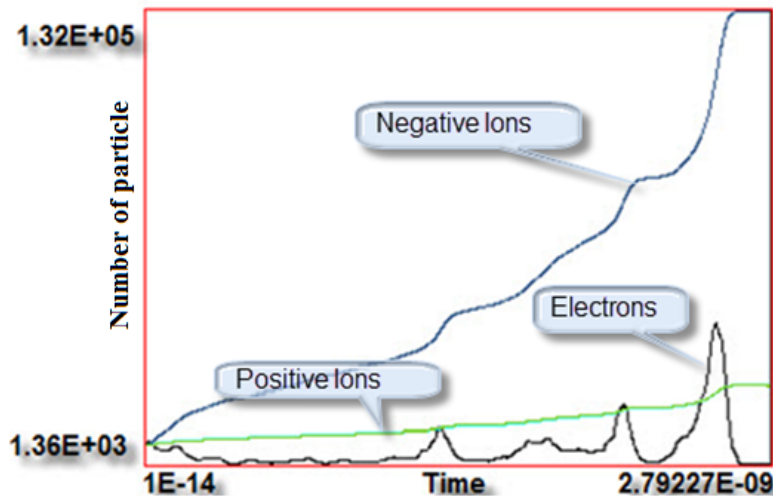


Figure 6.14 CF<sub>4</sub> Particle charge number evolution versus time reported by N. Chivu, and M. Kahrizi [42].

The complete results of simulations of breakdown voltages for several gases in the modeled GIS devices are tabulated in Table 6.7.

It is a difficult and time consuming task to adjust the applied voltage such a way that the breakdown of different gases happens at the same time, in order to compare them

properly. For this reason, based on the simulated results shown in Table 6.4 we have plotted the  $V_B$ - $t$  characteristics, as presented in Figure 6.15. Using the extrapolation of these curves, we obtain the comparable breakdown voltages happen at the same time for all gases.

Table 6.7 Simulation results of breakdown voltages for greenhouse gases in the modeled GIS device.

Gas	NWs material	$V_{app}$ [V]	Time [s]
CO	Au	-175	$1.365 \times 10^{-9}$
CO <sub>2</sub>	Au	-200	$1.287 \times 10^{-9}$
CO <sub>2</sub>	Au	-250	$1.04 \times 10^{-9}$
CO <sub>2</sub>	Au	-150	$1.53 \times 10^{-9}$
CF <sub>4</sub>	Au	-275	$3.8e^{-10}$
CF <sub>4</sub>	Au	-175	$2.495 \times 10^{-9}$
CF <sub>4</sub>	Au	-215	$2.96 \times 10^{-9}$
CF <sub>4</sub>	ZnO	-120	$2.92 \times 10^{-9}$
CF <sub>4</sub>	ZnO	-150	$2.63 \times 10^{-9}$
CF <sub>4</sub>	Ag	-200	$1.425 \times 10^{-9}$
CF <sub>4</sub>	ZnO	-250	$3.57 \times 10^{-10}$
SF <sub>6</sub>	Au	-200	$4.6 \times 10^{-9}$
SF <sub>6</sub>	Au	-300	$4.7 \times 10^{-10}$
SF <sub>6</sub>	Au	-280	$1.07 \times 10^{-9}$
SF <sub>6</sub>	Au	-265	$1.3 \times 10^{-9}$
SF <sub>6</sub>	Au	-245	$1.7 \times 10^{-9}$
SF <sub>6</sub>	Au	-230	$4.25 \times 10^{-9}$
SF <sub>6</sub>	Ag	-300	$2.82 \times 10^{-10}$
SF <sub>6</sub>	Ag	-350	$2.37 \times 10^{-10}$
SF <sub>6</sub>	Ag	-150	$4.39 \times 10^{-9}$
SF <sub>6</sub>	ZnO	-250	$2.67 \times 10^{-10}$
SF <sub>6</sub>	ZnO	-150	$3.32 \times 10^{-9}$
SF <sub>6</sub>	ZnO	-300	$2.54 \times 10^{-10}$
NH <sub>3</sub>	Au	-150	$1.18 \times 10^{-9}$

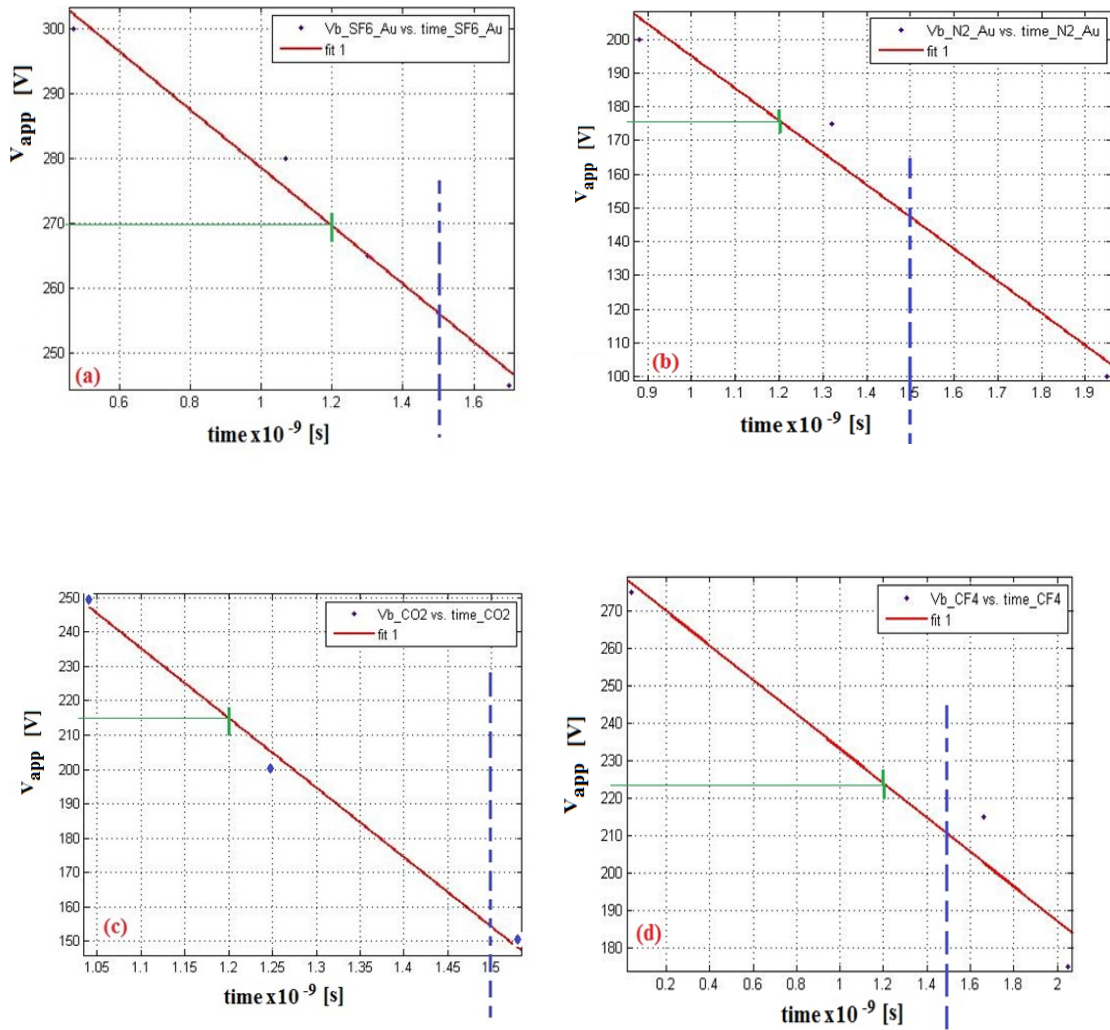


Figure 6.15  $V_{app} - t$  curves for a)  $SF_6$  – Gold; b)  $N_2$  – Gold; c)  $CO_2$  – Gold; d)  $CF_4$  – Gold.

The  $V_{app}-t$  characteristics presented in Figure 6.15 show that each gas has a unique relative breakdown voltage  $V_B$ , happens within the same time interval of [ $1 \times 10^{-9}$ ,  $1.51 \times 10^{-9}$ ] seconds. As an example, at time  $t = 1.2 \times 10^{-9}$  s, the extrapolated relative  $V_B$  values from the above graphs are listed in Table 6.8.

Table 6.8 Extrapolated  $V_B$  values at the sample time  $t = 1.2 \times 10^{-9}$  s, based on simulation results of breakdown voltages for several greenhouse gases in the modeled GIS device.

Gas	NWs material	$V_{app}$ [V]
SF <sub>6</sub>	Au	-270
N <sub>2</sub>	Au	-175
CO <sub>2</sub>	Au	-215
CF <sub>4</sub>	Au	-222

## 6.6 Detection of Breakdown Voltages for Mixed Gases

Using the GIS device with gold nanowires of length between 15 $\mu\text{m}$  and 35 $\mu\text{m}$ , a gap distance of 100 $\mu\text{m}$  and a width of 1000 $\mu\text{m}$ , simulations were done for Argon background gas with different impurity concentration of Ne. The results show clearly that the breakdown voltage is affected by adding an impurity. Figure 6.16 shows the phase space plot of ArNe mixed gases.

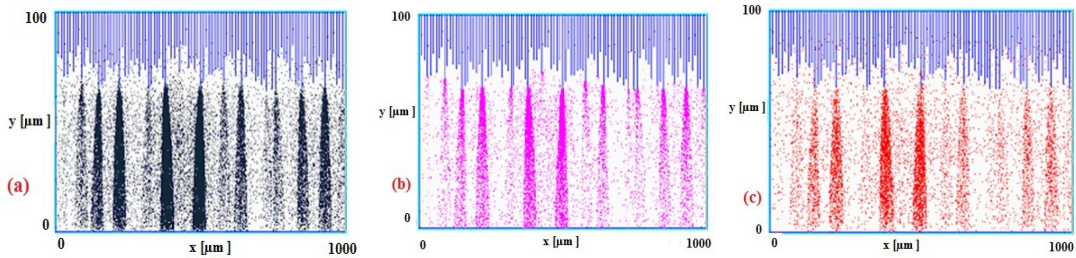


Figure 6.16 Phase space plot of Ar (50%)Ne(50%) for a) Argon ions; b) electrons; c) Neon ions.

Figure 6.17 a. shows electric field intensity inside the cell along the y-axis for pure Argon and electric field intensity inside the cell along the y-axis for Ar (10%) Ne (90%) is presented in Figure 6.16 b.

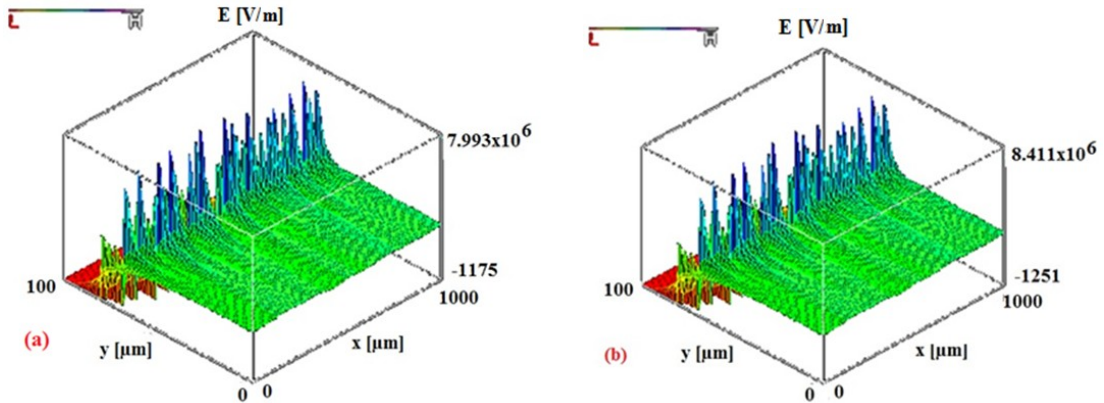


Figure 6.17 The electric field intensity along y axis ( $E_y$ ) of the cell for a) Ar (80%) Ne(20%); b) Ar(50%)Ne(50%).

Figure 6.18 shows a typical simulation result of generated current versus time between the two parallel plates for different concentrations of ArNe mixture.

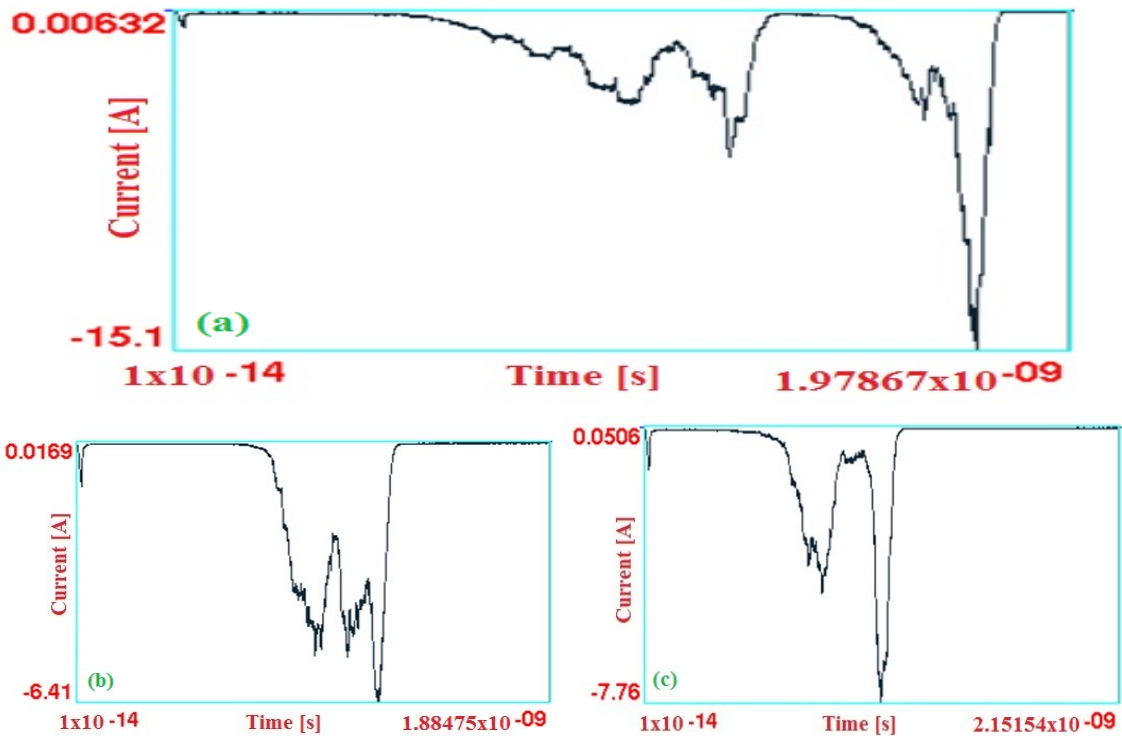


Figure 6.18 The generated current versus time for (a) Ar (10%) Ne (90%) (b) Ar (20%) Ne (80%) (c) Ar (50%) Ne(50%)

Table 6.9 represents the parameters used in the simulations for AuNWs, for two different gas mixture, at  $R = 10$  Ohm, (Beta = 500, X = 1000  $\mu\text{m}$ , Y = 100  $\mu\text{m}$ ).

ArNe			
Argon concentration	Neon concentration	Breakdown Voltage $V_{app}$ [V]	time [s]
100%	-	-145	1.6e-09
90%	10%	-165	1.6e-09
<b>80%</b>	<b>20%</b>	<b>-170</b>	<b>1.6e-09</b>
50%	50%	-175	1.6e-09
20%	80%	-180	1,59e-09
10%	90%	-178	1.6e-09
-	100%	-190	1.6e-09
ArHe			
Argon concentration	Helium concentration		
<b>80%</b>	<b>20%</b>	<b>-145</b>	<b>1.6e-09</b>

Our atmosphere is made of a mixture of gases in different concentrations, including oxygen (~21%), nitrogen (~78%) and carbon dioxide (~0.038%). For this reason we have performed simulation to detect the breakdown voltage of N<sub>2</sub>&O<sub>2</sub> and N<sub>2</sub>&O<sub>2</sub>&CO<sub>2</sub> mixtures. Although the mixture of N<sub>2</sub>(10%)O<sub>2</sub>(10%)CO<sub>2</sub>(80%), is not realistic but simulations were done for the testing purposes. The simulations results are recorded in Table 6.10.

Table 6.10 Simulation results of breakdown voltages for several gas mixtures in the modeled GIS device.

Gas	NWs material	V <sub>app</sub> [V]	Time [s]
He20%Ar80%	Au	-145	1.6 x10 <sup>-9</sup>
Ne10%Ar90%	Au	-210	8.85 x10 <sup>-10</sup>
Ne10%Ar90%	Au	-185	1.13 x10 <sup>-9</sup>
Ne10%Ar <sub>2</sub> 90%	Au	-175	1.16 x10 <sup>-9</sup>
Ne50%Ar50%	Au	-175	9.43 x10 <sup>-9</sup>
N <sub>2</sub> (10%)O <sub>2</sub> (10%)CO <sub>2</sub> (80%)	Au	-175	1.55x10 <sup>-9</sup>
N <sub>2</sub> (10%)O <sub>2</sub> (10%)CO <sub>2</sub> (80%)	Au	-200	1.13x10 <sup>-9</sup>
N <sub>2</sub> (10%)O <sub>2</sub> (10%)CO <sub>2</sub> (80%)	Au	-220	1.498x10 <sup>-9</sup>
N <sub>2</sub> (10%)O <sub>2</sub> (10%)CO <sub>2</sub> (80%)	Au	-250	9.25x10 <sup>-10</sup>
N <sub>2</sub> (10%)O <sub>2</sub> (10%)CO <sub>2</sub> (80%)	Au	-150	1.63x10 <sup>-9</sup>
N <sub>2</sub> (10%)O <sub>2</sub> (80%)CO <sub>2</sub> (10%)	Au	-150	2.301x10 <sup>-9</sup>
N <sub>2</sub> (10%)O <sub>2</sub> (80%)CO <sub>2</sub> (10%)	Au	-200	2.115x10 <sup>-9</sup>
N <sub>2</sub> (10%)O <sub>2</sub> (80%)CO <sub>2</sub> (10%)	Au	-250	1.02x10 <sup>-9</sup>
N <sub>2</sub> (79%)O <sub>2</sub> (21%)	Au	-100	1.38x10 <sup>-9</sup>
N <sub>2</sub> (79%)O <sub>2</sub> (21%)	Au	-140	1.29x10 <sup>-9</sup>
N <sub>2</sub> (79%)O <sub>2</sub> (21%)	Au	-175	9.38x10 <sup>-10</sup>
N <sub>2</sub> (78%)O <sub>2</sub> (20%)CO <sub>2</sub> (2%)	Au	-150	1.6x10 <sup>-9</sup>
N <sub>2</sub> (78%)O <sub>2</sub> (20%)CO <sub>2</sub> (2%)	Au	-200	1.47x10 <sup>-9</sup>

## 6.7 Conclusions

The breakdown characteristic of the device for AuNWs, AgNWs and ZnONWs was modeled using the XOOPIE-GIS software.

As it is seen from Table 6.2, as the aspect ratio of the nanowires increases the breakdown voltage decreases, this is due to the fact that the higher the aspect ratio the higher enhanced local field which in turn increases the total effective electric field between the two plates. The higher the electric field the faster the breakdown happens.

The interaction of electric field between the nanowires apparently affects the enhancement factor as a result the closer the nanowires are (smaller  $s$ ) the higher breakdown voltage will be. On the other hand, the distance between nanowires and the upper electrode ( $Y$ ) will change the breakdown inversely. The closer the nanowires get to the upper electrode the lower the breakdown voltage will be. This is not surprising however; in practice one must be careful because if  $Y$  gets too small there is possibility of sparks between the nanowires and the electrode, which may damage the device.

We found the optimal external resistance to be around 10 Ohms. Larger values of  $R$  causes that the breakdown happens at lower voltage but at longer time (the sensitivity of the device is an important factor).

The simulation of the ZnONWs gas sensor shows an improvement compared to its AuNWs and AgNWs counterparts, as the breakdown voltages were further reduced. The reduction of  $V_B$  was attributed to the lower work function of zinc oxide compared to that of gold and silver.

When an impurity is added to the Ar gas, the breakdown voltage is affected. The

changes in breakdown voltage are visible dependent on the impurity concentration and on the atomic mass of the impurity.

When 10%Ne, 20%Ne and so on, are added to the pure argon, the Ar breakdown voltage changes from -145V to -180V.

For the same concentration of Ar (80%) adding 20% of another gas, we found out that for different gases used as impurity, the Ar breakdown voltage is different, which means that  $V_B$  is also affected by atomic mass of the impurity.

For example for a mixture of 80% Ar and 20% Ne, we found  $V_B$  to be -170V but for 80% Ar and 20% He,  $V_B$  was found as -145V.

The breakdowns of the greenhouse gases are studied. From the simulation results tabulated in Table 6.7 the  $V_B$  was plotted with respect to time (Figure 6.13). Using the produced graphs we determined the actual breakdown of gases under the same conditions. The results show distinct breakdown voltages for each gas.

# Chapter 7

## Summary, Contributions and Future Work

### 7.1 Summary of the Project

In this research work, we have designed and modeled and simulated a miniaturized gas sensor based on what was fabricated in our laboratories prior to this work.

The device is made of two parallel plates with nanowires grown on one of the plates, sandwiched between them. The goal of the project was to optimize the structure and functionality of the sensor to detect various gases including greenhouse gases and odors. There is an ongoing research in the Micro/Nano Device laboratories in ECE department at Concordia to develop a GIS for various applications. The aim of this research was to help to save time and cost for future fabrication of the sensors in that labs and other researchers working in this area. All the parameters responsible for the function of the device in terms of sensitivity, selectivity, and fast response were considered in our model. The field emission inside the device and its enhancement due to the sharp nanowires were studied, the electrostatic interaction between arrays of nanowires was investigated and considered in the model. The simulation tools of COMSOL and XOOPIC are introduced, their structure and how to implement them were discussed. Using these simulation tools we have studied the effect of structural elements on the function of the device and based

on our finding we recommended the most relevant parameters to achieve an optimized design for future works. Finally we have estimated the breakdown voltages for several gases as a reference for future researchers in this field.

## 7.2 Contributions

The following is the list of major contributions of this work to the design and modeling of the GIS device.

- The electric field inside the GIS and its enhancement due to the presence of nanowires were studied thoroughly. The nonlinear electric field at the tip of the nanowires was studied. The enhancement factor of an array of nanowires was presented analytically. The screening of the electric field and reduction of enhancement factor due to the interactions of electric fields of an array of nanowires were investigated. Our results have shown that the screening effect is weaker as the nanowires are grown far apart from each other.
- Using the finite element method analyzer COMSOL, we have simulated the static electric field (responsible for the ionization of gases inside the GIS) around the individual and arrays of nanowires. The effects of the shapes of nanowires tips, their separations, their materials, dielectric gases between the electrodes, and the gap between the nanowires and the opposite electrode on the local electric field were studied.

- Based on an open source tool, the XOOPIE-GIS software program was developed to simulate the GIS model. We modified and developed the tool to accommodate our modeled device and simulate its structure and function. The series resistance “R” is integrated into new XOOPIE-GIS codes. The gas discharge inside of the GIS is modeled by MCC and various collisions between the electrons and neutral molecules are implemented in our developed software tool. The complete device structure and corresponding parameters are modeled into the input file of the XOOPIE-GIS.
- The breakdown voltage  $V_b$  and the relationship between  $V_b$  and the parameters which affect the functionality of the device are studied through XOOPIE-GIS software simulations. For the modeled GIS device structure, we have analyzed the simulations results in order to optimize parameters such a way that the breakdown of gases happens at a lowest applied voltage. Based on these studies our recommendations are:
  - ✓ A reasonable value of the series resistance “R” is to be around 10 Ohms. Due to the circuit limitations, “R” cannot be considered greater than this value.
  - ✓ The optimized gap distance between the two parallel plates is about 100 $\mu$ m and the chamber width 1 mm. Although we have found that the breakdown voltage decreases as the gap decreases, in practice the gas chamber cannot be too narrow, to allow a proper gas flow inside the device.
  - ✓ The semispherical nanowires tip shape shown the best electric field distribution along the tip surface.
  - ✓ To avoid the screening effect, the NWs should be grown far apart from each other. In the present work it is shown that an interwire spaces about four times the nanowire length will not affect the overall electric field intensity, in other

words under this condition the screening effect is minimized.

- ✓ A good value of the nanowires aspect ratio,  $l/r$ , will be 500 if the technology allows to fabricate such nanowires.
  - ✓ Nanowires material with a lower work function causes a lower breakdown voltage in the device.
- 
- The simulated device model is extended to detect and measure the breakdown voltages of greenhouse gases like SF<sub>6</sub>, CF<sub>4</sub>, CO, CO<sub>2</sub>, O<sub>2</sub>, NH<sub>3</sub> as well as mixture of gases like Ar&Ne, Ar&He, N<sub>2</sub>&O<sub>2</sub>, N<sub>2</sub>&O<sub>2</sub>&CO<sub>2</sub>.

## 7.3 Future Work

While we accomplished much in our work in modeling and optimizing of the design and structure of the GIS device, still more investigations can be made in the following areas:

- **3D simulation** – Much of the physics requires a three dimensional simulations for a more accurate result. The code presented in our work can be further developed to accommodate the 3D future, but beside the complexity of the physics in the new codes, still remains the question of the computational speed and power.
  
- **Meshing on the grid** – While the mesh grid makes the physics computations to be fast and easy however, this type of mesh couldn't solve our need of various device

design. The segments in graphics can be done only in a step function, and the fine tips for some nanowires cannot be achieved. Future development can be done into the grid generating functions to implement a simulation capable to increase the control over mesh spacing and boundaries of nanowires tip shape.

- **Modeling of the ion-neutral Monte Carlo Collision** – due to the lack of available cross sections data in the literature, in present work we did not take the ion-molecule interactions into account. The new MCC package to accommodate the greenhouse gases employed in the present study should be further assessed with analytical computational work to develop the corresponding cross sections.
- **To identify one or few gases in a soup** – In present work studies were done to analyze the effect of impurities and the breakdown of the mixture of gases. An area of interest for further research is the gas detection from a soup of gases, for example to detect the toxic gases in the air. For this probably a grid of the designed sensors needed to detect various gases simultaneously. Another suggestion is to design the GIS as a two non-parallel plates device as presented in section 4.1.6.
- **Apply the results of the work in practice** – Another area for future work is to apply the results of the modeled GIS in practice in particular for monitoring the greenhouse gases.

## Bibliography

- [1] Y. Sakurai, H. Jung, T. Shimanouchi, T. Inoguchi, S. Morita, R. Kuboi, K. Natsukawa, “Novel array-type gas sensor using conducting polymers, and their performance for gas identification”, *Sensors and Actuators B* 83, 270-275, 2002.
  
- [2] Y. T. Jang, S. Moona, J. H. Ahn, Y. H. Lee, B. K. Ju, “A simple approach in fabricating chemical sensor using laterally grown multi-walled carbon nanotubes”, *Sensors and Actuators B* 99 118–122, 2004.
  
- [3] A. I. Zad, F. Rahimi, M. Chavoshi, M. M. Ahadian, “Characterization of porous poly-silicon as a gas sensor”, *Sensors and Actuators B* 100 341–346, 2004.
  
- [4] O. K. Varghese, P. D. Kihambre, D. Gong, K. G. Ong, E. C. Dickey, C. A. Grimes, “Gas sensing characteristics of multi-wall carbon nanotubes”, *Sensors and Actuators B* 81 32-41, 2001.
  
- [5] W. Wongwiriyan, S. Honda, H. Konishi, T. Mizuta, T. Ikuno, T. Ito, T. Maekawa, K. Suzuki, H. Ishikawa, K. Oura and M. Katayama, “Single-Walled Carbon Nanotubes Thin-Film Sensor for Ultrasensitive Gas Detection”, *Japanese Journal of Applied Physics*, Vol. 44, No. 16, pp. L 482–L 484, 2005.

- [6] M.Y. Faizah, A. Fakhru'l-Razi, R.M. Sidek and A. G. Liew Abdullah, "Gas Sensor Application of Carbon Nanotubes", *International Journal of Engineering and Technology*, Vol. 4, No. 1, pp. 106-113, 2007.
- [7] M. Y. Faizah, "Room Temperature Multi Gas Detection Using Carbon Nanotubes", *European Journal of Scientific Research* ISSN 1450-216X Vol.35 No.1, pp 142-149, 2009.
- [8] J. K. Abraham, B. Philip, A. Witchurch, V. K. Varadan and C. C. Reddy, "A compact wireless gas sensor using a carbon nanotube/PMMA thin film chemiresistor", *Smart Mater. Struct.* 13 1045–1049, 2004.
- [9] J. Li, Y. Lu, Q. Ye, L. Delzeit, and M. Meyyappan, "A Gas Sensor Array Using Carbon Nanotubes and Microfabrication Technology", *Electrochemical and Solid-State Letters*, 8 11 H100-H102, 2005.
- [10] S. Kim, "CNT Sensors for Detecting Gases with Low Adsorption Energy by Ionization," *Sensors*, vol. 6, pp. 503-513, 2006.
- [11] A. Modi, N. Koratkar, E. Lass, B. Wei, and P. M. Ajayan, "Miniaturized gas ionization sensors using carbon nanotubes," *Nature*, vol. 424, pp. 171-174, 2003.

- [12] Y. Zhang, J. Liu, X. Li, and C. Zhu, "The structure optimization of the carbon nanotube film cathode in the application of gas sensor," *Sensors and Actuators A: Physical*, vol. 128, pp. 278-289, 2006.
- [13] Z. Yong, L. Junhua, L. Xin, T. Xiaojun, and Z. Changchun, "Study of improving identification accuracy of carbon nanotube film cathode gas sensor," *Sensors and Actuators A: Physical*, vol. 125, pp. 15-24, 2005.
- [14] Z. Yong, L. Junhua, L. Xin, D. Juying, L. Weihua, H. Yongning, and Z. Changchun, "Study of gas sensor with carbon nanotube film on the substrate of porous silicon," *Proc. IEEE IVMC*, pp. 13-14, 2001.
- [15] C. Xing, H. Zhongying, H. Jiarui, L. Jinhuai, and K. Mingguang, "Gas ionization sensors using well-aligned MWCNT arrays grown in porous AAO template," *Proc. IEEE ICIA*, Hong Kong and Macau, China, pp. 290-293, 2005.
- [16] Z. Hou, D. Xu, and B. Cai, "Ionization gas sensing in a microelectrode system with carbon nanotubes," *Appl. Phys. Lett.*, vol. 89, pp. 213502-1 - 213502-3, 2006.
- [17] G. Hui, L. Wu, M. Pan, Y. Chen, T. Li, and X. Zhang, "A novel gas-ionization sensor based on aligned multi-walled carbon nanotubes," *Meas. Sci. Technol.*, vol. 17, pp. 2799-2805, 2006.

- [18] A. M. Howatson, *An introduction to gas discharges*, 2<sup>nd</sup> ed. Oxford: Pergamon Press, 1976.
- [19] J. M. Meek and J. D. Craggs, *Electrical Breakdown of Gases*. New York: John Wiley & Sons, 1978.
- [20] M. Abdel-Salam, H. Anis, A. El-Morshedy, and R. Radwan, *High Voltage Engineering—Theory and Practice*, 2<sup>nd</sup> ed. New York: Dekker, 2000.
- [21] A. Modi, N. Koratkar, E. Lass, B. Wei & P.I M. Ajayan, “Miniaturized gas ionization sensors using carbon nanotubes”, *Nature* V0p 424, 10 July 2003
- [22] J. Huang, J. Wang, C. Gu, K. Yu, F. Meng, J. Liu, “A novel highly sensitive gas ionization sensor for ammonia detection”, *Sensors and Actuators A* 150 , 218–223, 2009.
- [23] L. Liao, H. B. Lu<sup>1</sup>, M. Shuai, J. C. Li, Y. L. Liu, C. Liu, Z. X, Shen and T. Yu, “A novel gas sensor based on field ionization from ZnO nanowires: moderate working voltage and high stability”, *Nanotechnology* 19, 175501 (5pp), 2008.

- [24] R. B. Sadeghain, N. Chivu and M. Kahrizi “Sub-torr Operation of a Miniature Gas Ionization Sensor Based on Gold Nanowires”, *Sensors and Materials*, Vol. 21, No. 1 53-64, 2009.
- [25] R. B. Sadeghian and M. Kahrizi, “A novel miniature gas ionization sensor based on freestanding gold nanowires,” *Sensors and Actuators: A Physical*, vol. 137, no. 2, pp. 248–255, 2007.
- [26] N. Azmoodeh, N. Chivu, R.B. Sadeghian, and M. Kahrizi “A Silver Nanowire based Gas Ionization Sensor”, EUROCON 2009, 18-23 May 2009.; *IEEE XPlore*, 2009.
- [27] N. Chivu, R.B. Sadeghian, and M. Kahrizi, “Modeling and Simulation of a Miniaturized Gas Sensor”, EUROCON 2009, May 18-23, At. Petersburg, Russia, 2009.
- [28] R. B. Sadeghian, S. Badilescu, Y. Djaoued, S. Balaji, V-V. Truong and M. Kahrizi, “Ultra-low voltage Schottky barrier field enhanced electron emission from gold nanowires electrochemically grown in modified porous alumina templates,” *IEEE Electron. Dev. Lett.*, vol. 29, no. 4, pp. 312–314, 2008.

- [29] R. B. Sadeghian and M. Kahrizi, "A Low Voltage Gas Ionization Sensor based on Sparse Gold Nanorods," *The 6th IEEE Sensors Conf., Atlanta, GA*, Oct., pp. 648–651, 2007.
- [30] R. B. Sadeghian and M. Kahrizi, "Enhanced field-emission properties of electrochemically grown Au nanorods in porous AAO templates," *13th CSTC, Montréal*, pp. 31–32, 2007.
- [31] R. B. Sadeghian and M. Kahrizi, "Low voltage field-ionization using sparse gold nanorods," *13th CSTC, Montréal, Aug.*, pp. 193–194, 2007.
- [32] R. B. Sadeghian and M. Kahrizi, "A Low Pressure Gas Ionization Sensor Using Freestanding Gold Nanowires," *IEEE ISIE, Vigo, Spain*, pp. 1387–1390, 2007.
- [33] R. B. Sadeghian and M. Kahrizi, "Finite-element Modeling of the Field-enhancement Phenomenon in Nanoscale Field emitters and Field-ionizers," in *Proc. COMSOL Multiphysics Conf., Boston, MA*, pp. 251–254, 2007.
- [34] R. B. Sadeghian and M. Kahrizi, "Miniaturized Gas Ionization Sensor," presented in the 5th CWMEMS Contest, Montréal, Aug. 2007.
- [35] A. M. Howatson, *An introduction to gas discharges*, 2nd ed. Oxford: Pergamon Press, 1976.

- [36] J. M. Meek and J. D. Craggs, *Electrical Breakdown of Gases*. New York:: John Wiley & Sons, 1978.
- [37] M. Abdel-Salam, H. Anis, A. El-Morshedy, and R. Radwan, *High Voltage Engineering–Theory and Practice*, 2nd ed. New York: Dekker, 2000.
- [38] M. K. Miller, A. Cerezo, M. G. Hetherington, and G. D. W. Smith, *Atom Probe Field Ion Microscopy*. New York: Oxford, 1996.
- [39] R. Gomer, *Field emission and Field ionization*. Cambridge: Harvard Univ. Press, 1961.
- [40] T. T. Tsong, *Atom-Probe Field Ion Microscopy*. Cambridge: Harvard Univ. Press, 1990.
- [41] T. Sakurai, A. Sakai, and H. W. Pickering, *Atom-Probe Field Ion Microscopy and its Applications*. San Diego: Academic Press Inc., 1989.
- [42] N. Chivu, and M. Kahrizi, “Design, modeling and simulation of a miniaturized gas ionization sensor: Optimization of the structure and operation”, *ICIT2012*, *Athen*,

Greece, <http://ieeexplore.ieee.org/xpl/mostRecentIssue.jsp?punumber=6198915>

March 2012.

- [43] D. G. Brandon, "The resolution of atomic structure: recent advances in the theory and development of the field ion microscope," *British Journal of Applied Physics*, vol. 14, pp. 474-484, 1963.
  
- [44] X. Liu and J. Orloff, "Analytical model of a gas phase field ionization source," *J. Vac. Sci. Technol.*, pp. 2816-2820, 2005.
  
- [45] T. Sakurai and E. W. Muller, "Field calibration using the energy distribution of a free-space field ionization," *Journal of Applied Physics*, vol. 48, pp. 2618-2625, 1977.
  
- [46] R. Gomer, "*Field emission and Field ionization*". Cambridge: Harvard Univ. Press, 1961.
  
- [47] R. G. Forbes, C. J. Edgcombe, and U. Valdre, "Some comments on models for field enhancement," *Ultramicroscopy*, vol. 95, pp. 57-65, 2003.
  
- [48] F. H. Read and N. J. Bowring, "Field enhancement factors of random arrays of carbon nanotubes," *Nucl. Instrum. Methods Phys. Res. Sect. A*, vol. 519, pp. 305-314, 2004.

- [49] H. C. Miller, “Change in Field Intensification Factor beta of an Electrode Projection (Whisker) at Short Gap Lengths,” *J. Appl. Phys.*, vol. 38, pp. 4501-4504, 1967.
- [50] F.H. Read, N.J. Bowring, “Field enhancement factors of one-dimensional and two-dimensional arrays of nanotubes” *Microelectronic Engineering* 73–74, pp 679–685, 2004.
- [51] X.Q. Wanga, M. Wangc, H.L. Gea, Q. Chena, Y.B. Xu, “Modeling and simulation for the field emission of carbon nanotubes array”, *Physica E* 30, pp 101–106, 2005.
- [52] M. Lim, D. Kim, S. Y. Kim and J.E. Bourée, “Calculation of the local electric field for an infinite array of conducting nanosized objects”, *J. Phys. A: Math. Theor.* 40, pp 853–862, 2007.
- [53] X.Q. Wanga, M. Wanga, Z.H. Lib, Y.B. Xua, P.M. Hea, “Modeling and calculation of field emission enhancement factor for carbon nanotubes array”, *Ultramicroscopy* 102 , pp 181–187, 2005.
- [54] D.Kkim, J.E. Bouree, S.Y. Kim, “Numerical study on the field emission properties of aligned carbon nanotubes using the hybrid field enhancement scheme”, *Appl. Phys. A* 83, pp 111–114, 2006.

- [55] N.V. Egorov, A.A. Almazov, "Optimization of multi-tip field emission electron source", *Vacuum* 52 pp 295-300, 1999.
- [56] B. Florkowska and R. Wlodek, "Pulse Height Analysis of Partial Discharges in Air", *Transactions on Electrical Insulation*, Vol. 28 No. 6, December 1993.
- [57] M. R. Spiegel, "*Theory and Problems of Vector Analysis*", Schaum Publishing Co., New York
- [58] P. Moon, D. E. Spencer, "Field Theory for Engineers", D. van Nostrand CO, Inc, 1961.
- [59] S. Hamada and T. Takuma, "*Electric Field Calculation in Composite Dielectrics by Curved Surface Charge Method Based on Electric Flux Continuity Condition*", *Electrical Engineering in Japan*, Vol. 141, No. 3, 2002.
- [60] V. M. Zhukov, "Multi-tip field emission-based electron sources", *Nuclear Instruments and Methods in Physics Research A* 558 , pp 271–273, 2006.
- [61] M. R. Radjenovic and B. Radjenovic, "A Particle-in-Cell Simulation of the High-Field Effect in Devices with Micrometer Gaps", *IEEE Transactions on Plasma Science*, Vol. 35, No. 5, October 2007.

- [62] C. K. Birdsall, "Particle-in-Cell Charged-Particle Simulations, Plus Monte Carlo Collisions With Neutral Atoms, PIC-MCC", *IEEE Transactions on Plasma Science*, Vol. 19, No. 2, April 1991.
- [63] V. V. Serikov and K. Nanbu, "Spatio-Temporal Variations in a Three-Dimensional DC Glow Discharge via Particle-in-Cell Simulation", *IEEE Transactions on Plasma Science*, Vol. 27, No. 1, February 1999.
- [64] V. Vahedi, M. Surendra, "A Monte Carlo collision model for the particle-in-cell method: applications to argon and oxygen discharges", *Computer Physics Communications* 87 179-198, 1995.
- [65] M. Roberto, H. B. Smith, and J. P. Verboncoeur, "Influence of Metastable Atoms in Radio-Frequency Argon Discharges", *IEEE Transactions on Plasma Science*, Vol. 31, No. 6, December 2003.
- [66] C. Thoma, T. P. Hughes, N. L. Bruner, T. C. Genoni, D. R. Welch, and R. E. Clark, "Monte Carlo Versus Bulk Conductivity Modeling of RF Breakdown of Helium", *IEEE Transactions on Plasma Science*, Vol. 34, No. 3, June 2006.

- [67] V. Vahedi and M. Surendra , “A Monte Carlo collision model for the particle-in-cell method: applications to argon and oxygen discharges” , *Computer Physics Communications* 87 , 179-198, 1995.
- [68] S. Mahalingam and J. A. Menart , “Computational Model Tracking Primary Electrons, Secondary Electrons, and Ions in the Discharge Chamber of an Ion Engine” , *NASA/CR—2005-213833, AIAA—2005—4253*.
- [69] C. K. Birdsall, “Plasma Physics via Computer Simulation”, *McGraw-Hill*, New York.
- [70] L. G. Christophorou and J. K. Olthoff, “Electron Interactions With Plasma Processing Gases: An Update for CF<sub>4</sub>, CHF<sub>3</sub>, C<sub>2</sub>F<sub>6</sub>, and C<sub>3</sub>F<sub>8</sub>, ”, *J. Phys. Chem. Ref. Data*, Vol. 28, No. 4, 1999.
- [71] L. G. Christophorou, J. K. Olthoff and M. V. V. S. Rao, “Electron Interactions with CF<sub>4</sub>”, *J. Phys. Chem. Ref. Data*, Vol. 25, No. 5, 1996.
- [72] Y. Itikawa, “Cross Sections for Electron Collisions With Carbon Dioxide”, *J. Phys. Chem. Ref. Data*, Vol. 31, No. 3, 2002.

- [73] Y. Itikawa, M. Hayashi, A. Ichimura, K. Onda, K. Sakimoto, K. Takayanagi, “Cross Sections for Collisions of Electrons and Photons with Nitrogen Molecules”, *J. Phys. Chem. Ref. Data*, Vol. 15, No. 3, 1986
- [74] Y. Itikawa, M. Hayashi, A. Ichimura, K. Onda, K. Sakimoto, K. Takayanagi, “Cross Sections for Collisions of Electrons and Photons with Oxygen Molecules”, *J. Phys. Chem. Ref. Data*, Vol. 18, No. 1, 1989
- [75] L. G. Christophorou and J. K. Olthoffand, “Electron Interactions with SF<sub>6</sub>”, *J. Phys. Chem. Ref. Data*, Vol. 29, No. 3, 2000.
- [76] O. J. Orient and S. K. Srivastava, “Electron impact ionisation of H<sub>2</sub>O, CO, CO<sub>2</sub> and CH<sub>4</sub>”, *J. Phys. B: At. Mol. Phys.* 20, 3923-3936, 1987.
- [77] I. Kanik and S. Trajmar, J. C. Nickel, “Total Electron Scattering and Electronic State Excitations Cross Sections for O<sub>2</sub>, CO, and CH<sub>4</sub>.”